

# **Impact of Climate Change on the Frequency and Intensity of Low-Level Temperature Inversions in California**

**Sam Iacobellis, Dan Cayan, Joel Norris and Masao Kanamitsu  
Scripps Institution of Oceanography, University of California San Diego**

**Final Report to the California Air Resources Board  
Project 06-319**

**July, 2010**

## **DISCLAIMER**

**The statements and conclusions in this report are those of the contractor and not necessarily those of the California Air Resources Board. The mention of commercial products, their source, or their use in connection with material reported herein is not to be construed as actual or implied endorsement of such products.**

## **ACKNOWLEDGEMENTS**

**This project was funded by the California Air Resources Board (Project No. 06-319). We would like to thank Nehzat Motallebi for project management and guidance. We would like to thank those who helped review this report and particularly Leon Dolislager for his thorough and insightful comments. We would also like to thank Mary Tyree and Emelia Bainto for data processing.**

## GLOSSARY of SYMBOLS and ACRONYMS

—	Overbar denotes spatial mean
$\sigma_{H500'}$	Standard deviation of geopotential height anomalies at 500 hPa
$\theta$	potential temperature
$\theta_{2M}$	potential temperature at 2 meters above surface
$\theta_{850}$	potential temperature at 850 hPa
$\theta_{BASE}$	potential temperature at inversion base
$\theta_{TOP}$	potential temperature at inversion top
00Z	0000 Hours (midnight) Greenwich mean time
12Z	1200 Hours (noon) Greenwich mean time
AR4	Fourth Assessment Report
°C	Degrees Centigrade
CaRD10	California Reanalysis Downscaling at 10km
CNRM	Centre National de Recherches Meteorologiques climate model
DJF	December-January-February
$D\theta_{850}$	Potential temperature difference between 850 hPa and 2 meters above surface
$D\theta_{850,SJV}$	Potential temperature difference between 850 hPa and 2 meters above surface in the San Joaquin Valley Air Basin
$D\theta_{850,SC}$	Potential temperature difference between 850 hPa and 2 meters above surface in the South Coast Air Basin
$DT_{INV}$	Temperature difference between inversion top and inversion base
$DZ_{INV}$	Height difference between inversion top and inversion base
ENSO	El Nino Southern Oscillation
ERSL	Earth System Research Laboratory
°F	Degrees Fahrenheit
$F_i$	Fractional occurrence of cluster i
GCM	Global Climate Model
GDL	Greatest difference from linearity
GFDL	Geophysical Fluid Dynamics Laboratory climate model
GHCN2	Global Historical Climatology Network Version 2
GTS	Global Telecommunications System
hPa	Hectopascals
H500	Geopotential height at 500 hPa
H500'	Geopotential height anomaly at 500 hPa
$H500'_N$	Normalized geopotential height anomaly at 500 hPa
H700	Geopotential height at 700 hPa
H700'	Geopotential height anomaly at 700 hPa
HadAT2	Hadley Centre Radiosonde Temperature product version 2
IPCC	Intergovernmental Panel on Climate Change
JJA	June-July-August
°K	Degrees Kelvin
km	Kilometer
KOAK	Oakland Radiosonde site

KSAN	San Diego Radiosonde site
LT	Local Time
m	meter
MAM	March-April-May
MIROC	National Institute for Environment Studies Model for Interdisciplinary Research on Climate
MPI	Max Planck Institute climate model
$N_C$	Number of clusters used in the cluster analysis
NCARc	National Center for Atmospheric Research community climate system model
NCARp	National Center for Atmospheric Research parallel climate model
NCDC	National Climatic Data Center
NCEP	National Centers for Environmental Prediction
NNDC	NOAA National Data Centers
NOAA	National Oceanic and Atmospheric Administration
$N_{RUN}$	Number of runs made with the cluster analysis model
O700	Vertical velocity at 700 hPa
O700'	Vertical velocity anomaly at 700 hPa
O700 <sub>N</sub> '	Normalized vertical velocity at 700 hPa
OBS	Observations
p	Probability of correlation being coincidental
PDO	Pacific Decadal Oscillation
PM10	Particulate Matter smaller than 10 microns
PST	Pacific Standard Time
PV	Persistence Value
Q <sub>1</sub>	First quartile level
Q <sub>3</sub>	Third quartile level
R	Correlation statistic
R1	National Centers for Environmental Prediction Reanalysis I
$R_{CEN}$	Correlation value using centered correlation statistic
RAOBCORE	Radiosonde Observation Correction using Reanalyses
RATPAC	Radiosonde Atmospheric Temperature Products for Assessing Climate
RH	Relative humidity
RMS	Root Mean Square
RSM	Regional Spectral Model
$R_{UNC}$	Correlation value using uncentered correlation statistic
SJVAB	San Joaquin Valley Air Basin
SOCAB	South Coast Air Basin
SOI	Southern Oscillation Index
SON	September-October-November
SRES	Special Report on Emissions Scenarios
SRES A2	Special Report on Emissions Scenarios A2 scenario (less optimistic emission scenario)
SRES B1	Special Report on Emissions Scenarios B1 scenario (more optimistic emission scenario)
SST	Sea Surface Temperature
T <sub>2M</sub>	Temperature at 2 meters above surface

T <sub>500</sub>	Temperature at 500 hPa
T <sub>850</sub>	Temperature at 850 hPa
T <sub>995</sub>	Temperature at the 0.995 sigma level, where 0.995 refers to the ratio between the level pressure and the surface pressure.
T <sub>BASE</sub>	Inversion base temperature
T <sub>MAX</sub>	Maximum Daily Temperature
T <sub>MIN</sub>	Minimum Daily Temperature
T <sub>TOP</sub>	Inversion top temperature
UTC	Universal Coordinated Time
V <sub>H500'</sub>	Variance of geopotential height anomalies at 500 hPa
V <sub>O700'</sub>	Variance of vertical velocity anomalies at 700 hPa
V <sub>i</sub>	Variance within cluster i
V <sub>RUN</sub>	Variance computed for each run of the cluster analysis model
WMO	World Meteorological Organization
Z <sub>BASE</sub>	Inversion base height
Z <sub>TOP</sub>	Inversion top height

## **PROPOSED TASKS AND WORK DESCRIBED IN THIS REPORT**

The tasks identified in the original proposal are outlined below. Sections within this report containing results from each task are also identified.

### **Task 1. Identify and acquire historical climate records.**

These historical climate records are introduced in Section 2 and are used throughout the report.

### **Task 2. Obtain downscaled regional model data products based on reanalysis.**

This data is described in Section 2.4 and is used primarily in Section 5.

### **Task 3. Produce SCM data products in regions of high inversion frequency**

Results from the SCM poorly reproduced observed variability of inversion characteristics in the air basins examined in this study. We believe this is due in part to deficiencies in the forcing data needed to run the SCM. The SCM was forced with data supplied by NCEP Reanalysis that we feel in hindsight was too coarse (2.5 x 2.5 horizontal resolution) to be able to distinguish between SCM during different inversion conditions.

### **Task 4. Catalog occurrence of low-level inversions and other pertinent atmospheric variables in various regions of California.**

These results are described in Section 4 and Section 6.

### **Task 5. Diagnose circulation patterns and meteorological variables associated with low-level inversions.**

These results are shown in Sections 5, 6, and 8.

### **Task 6. Examine how inversion frequency/magnitude related to warm/cold periods in historical record**

These results are shown primarily in Section 7.

### **Task 7. Examine role of decadal climate modes and ENSO on circulation patterns, meteorological variables and inversion characteristics.**

These results are described in Section 7.

### **Task 8. Identify and acquire GCM climate simulations**

The models used for the GCM climate simulations are shown in Table 8-1. The results from these model simulations are used in Section 8.

**Task 9. Obtain downscaled regional model products based on GCM climate simulations**

Statistical regression models applicable to the individual air basins are developed and described in Section 8.

**Task 10. Diagnose future inversion frequency/magnitude from GCM simulations**

**Task 11. Examine seasonal and regional patterns**

**Task 12. Examine range of results for different greenhouse gas scenarios**

Results from Tasks 10-12 are presented in Section 8.

**Task 13. Preparation of articles and reports.**

This task was performed during the course of the project in the preparation of quarterly progress reports, a report to the California Climate Change Center (Iacobellis et al, 2009), this report, and the preliminary drafts of two journal articles.

## TABLE OF CONTENTS

DISCLAIMER.....	2
ACKNOWLEDGEMENTS .....	3
GLOSSARY OF SYMBOLS AND ACRONYMS .....	4
PROPOSED TASKS AND WORK DESCRIBED IN THIS REPORT .....	7
LIST OF FIGURES .....	11
LIST OF TABLES.....	16
EXECUTIVE SUMMARY .....	18
1.0 INTRODUCTION .....	25
2.0 DATA.....	28
2.1 Radiosonde Measurements .....	28
2.2 Surface Temperature Measurements .....	31
2.3 Reanalysis Data .....	34
2.4 Regional Atmospheric Model Data .....	34
2.5 How Representative are Oakland and San Diego Radiosonde Measurements of Conditions in Other Air Basins?.....	35
2.6 Climate Model Projections .....	38
3.0 INVERSION CHARACTERISTICS AND MEASURES .....	39
3.1 General Inversion Measures .....	39
3.2 Measures of Strong and Weak Inversions .....	41
3.3 Measures of the Persistence of Strong and Weak Inversions .....	42
4.0 INVERSION CLIMATOLOGY AND CHARACTERISTICS .....	42
4.1 Seasonal Cycle of Inversion Frequency .....	42
4.2 Comparison of Radiation and Subsidence Inversions .....	44
4.3 Seasonal Cycle and Variability of Subsidence Inversion Measures .....	48
4.4 Relationship Between Subsidence Inversion Measures .....	50
4.5 Relationship Between Inversion Strength and Pollutant Concentrations.....	54
5.0 INFLUENCE OF LARGE-SCALE CIRCULATION AND SEA SURFACE TEMPERATURE ON INVERSIONS .....	56
5.1 Large-Scale Circulation Patterns Associated with Inversion Strength.....	56
5.1.1 Physical Mechanisms and Inversion Characteristics .....	62
5.2 Impact of Local Sea Surface Temperature on Inversion Measures .....	66
6.0 INVERSION PERSISTENCE.....	68
6.1 Persistence of Strong and Weak Inversions.....	68
6.2 Analysis of Persistent Inversion Episodes.....	70

7.0 TEMPORAL VARIABILITY OF INVERSION MEASURES DURING HISTORICAL PERIOD .....	84
7.1 Time Series of Inversion Strength and Inversion Depth .....	84
7.2 Time Series of Strong and Weak Inversion Frequency .....	95
8.0 PROJECTED VARIABILITY OF INVERSION MEASURES FOR 2010-2099 PERIOD	99
8.1 Cluster Analysis .....	99
8.1.1 Method .....	100
8.1.2 Cluster Pattern for H500 and O700 Monthly Mean Anomalies .....	102
8.2 Regression Models .....	106
8.2.1 Method .....	107
8.2.2 Uncentered Correlations vs Centered Correlations .....	109
8.3 Regressed Inversion Magnitudes for Historical Period 1960-1999 .....	111
8.4 Regressed Inversion Magnitudes for Future Period 2010-2099 .....	112
8.5 Inversion Magnitude Projections Directly from Climate Models .....	120
9.0 CONCLUSIONS .....	123
9.1 Inversion Climatology and Characteristics .....	123
9.2 Influence of Large-Scale Circulation and SST .....	124
9.3 Inversion Persistence .....	126
9.4 Temporal Variability of Inversion Measures during Historical Period .....	127
9.5 Projected Changes in Inversion Strength during 2010-2099 Period .....	129
9.6 Recommendations for Future Work .....	131
REFERENCES .....	133

## LIST OF FIGURES

- Figure 2-1.** Map of California denoting the radiosonde locations at Oakland, Vandenberg, and San Diego. Also shown on the map are the approximate boundaries of the San Joaquin Valley and South Coast Air Basins. The color contours indicate height above sea level (meters)..... 29
- Figure 2-2.** Plots showing cross-correlation (spatial coherence) of daily mean values of  $D\theta_{850}$  from the CaRD10 product relative to locations at (a) Oakland, (b) San Diego, and (c) Vandenberg..... 37
- Figure 3-1.** Schematic diagram showing some of the measures used to characterize low-level temperature inversions. .... 39
- Figure 4-1.** Monthly mean inversion frequency at Oakland (a, b), Vandenberg (c, d), and San Diego (e, f), determined from twice-daily radiosonde measurements. Subsidence inversion frequency (red curves), radiation inversion frequency (blue curves), and total (subsidence + radiation) inversion frequency (black curves) are shown separately. The data cover the period from 1960–2007. .... 43
- Figure 4-2.** Composite profiles of temperature, specific humidity, relative humidity, and clear-sky longwave heat rates. The composites were formed using radiosonde data from the 30 days with the strongest radiation (blue lines) and subsidence (red lines) inversions at the Oakland radiosonde location over the 1960-2007 period. Composites are shown for the JJA (top row) and DJF (bottom row). The clear-sky longwave heating rates were calculated with the parameterization of Morcrette (1988) based on composite temperature and humidity profiles..... 44
- Figure 4-3.** Composited cloud cover observations based on the 30 days with the strongest radiation (blue) and subsidence (red) inversions at the Oakland for DJF (top) and JJA (bottom). The composited cloud cover spans a 144 hour period centered at the 12Z radiosonde launch time. Cloud cover observations are from the NNDC hourly surface data set..... 45
- Figure 4-4.** Composited surface wind speed observations based on the 30 days with the strongest radiation (blue) and subsidence (red) inversions at Oakland for DJF (top) and JJA (bottom). The difference between the subsidence and radiation composites is shown by the green curve. The composited wind speeds spans a 144 hour period centered at the 12Z radiosonde launch time. Wind speed observations are from the NNDC hourly surface data set..... 47
- Figure 4-5.** Box plot diagrams showing the distribution of daily values at 00Z (red) and 12Z (blue) of  $DT_{INV}$ ,  $Z_{BASE}$ , and  $DZ_{INV}$  at (a) Oakland, (b) San Diego, and (c) Vandenberg radiosonde locations. Additionally, plots of  $D\theta_{850,SJV}$  and  $D\theta_{850,SC}$  are included in the Oakland and San Diego columns, respectively. The data cover the period from 1960–2007..... 49
- Figure 4-6.** Scatter plots of daily  $D\theta_{850}$  vs  $DT_{INV}$  anomalies at Oakland at 00Z (left column) and 12Z (right column). For this comparison,  $D\theta_{850}$  was calculated using only radiosonde data. Data was only included for those days when a subsidence inversion was measured.

- Plots only including days where  $Z_{\text{BASE}} < 1000$  meters are shown in (c) and (d). The time period is from 1960–2007. The straight lines represent best linear fits, and the correlation coefficients are shown within each plot. .... 53
- Figure 4-7.** Correlation of daily values of  $D\theta_{850}$  and pollutant concentration in the San Joaquin (top) and South Coast (bottom) Air Basins as a function of month. Correlations are shown for ozone (blue line) and particulate matter (PM10) (red line). Solid lines are correlations found using all available days while dashed lines only used days with daily  $T_{2M}$  within  $\pm 1.0$  °C of the monthly mean value. Monthly correlations are based on detrended daily values of 12Z  $D\theta_{850}$  and average pollutant concentration within the air basin. Open circles denote correlations not significant at the 95% confidence level... 55
- Figure 5-1.** Mean geopotential height and vertical velocity at 700 hPa from NCEP Reanalysis product during the 30 days with the largest (a, b) and smallest (c, d) inversion magnitudes ( $D\theta_{850,SJV}$  at 12Z) at the San Joaquin Valley Air Basin during the period 1979–2005. The geopotential heights are shown by the color contours and the vertical velocities are denoted by the black contour lines. Contour intervals are 2 pascals per second ( $\text{Pa sec}^{-1}$ ) (JJA [June, July, August]) and 3  $\text{Pa sec}^{-1}$  (DJF [December, January, February]) and dashed contours indicate negative (upward) vertical velocity..... 57
- Figure 5-2.** Mean geopotential height and vertical velocity at 700 hPa from NCEP reanalysis during the 30 days with the largest (a, b) and smallest (c, d) inversion magnitudes ( $D\theta_{850,SC}$  at 12Z) at the South Coast Air Basin during the period 1979–2005. The geopotential heights are shown by the color contours, and the vertical velocities are denoted by the black contour lines. Contour intervals are 2  $\text{Pa sec}^{-1}$  (JJA) and 3  $\text{Pa sec}^{-1}$  (DJF) and dashed contours indicate negative (upward) vertical velocity. .... 58
- Figure 5-3.** Average values of CaRD10  $D\theta_{850}$  and 10-meter wind during the 30 days with the largest (a, b) and smallest (c, d) observed  $D\theta_{850,SJV}$  during time period 1979–2005 for DJF (left column) and JJA (right column). The white line denotes the approximate boundary of the San Joaquin Valley Air Basin. The color filled contours indicate the CaRD10  $D\theta_{850}$  values; the vector arrows represent the 10-meter winds. Grey areas indicate where surface is above the 850 hPa level and  $D\theta_{850}$  is not defined..... 59
- Figure 5-4.** Average values of CaRD10  $D\theta_{850}$  and 10-meter wind during the 30 days with the largest (a, b) and smallest (c, d) observed  $D\theta_{850,SC}$  during time period 1979–2005 for DJF (left column) and JJA (right column). The white line denotes the approximate boundary of the South Coast Air Basin. The color filled contours indicate the CaRD10  $D\theta_{850}$  values while the vector arrows represent the 10-meter winds. Grey areas indicate where surface is above the 850 hPa level and  $D\theta_{850}$  is not defined..... 61
- Figure 6-1.** Distribution of persistent strong inversion episodes by season at Oakland (left) and San Diego (right) based on the episode length. .... 70
- Figure 6-2a.** Composite H700 anomaly plots for JJA based on the starting day (left column) and ending day (right column) of persistent strong inversion episodes lasting 5 days or longer at Oakland. Plots are shown for 3 days prior and 2 days after the start day and 2 days prior and 3 days after the ending day. .... 72
- Figure 6-2b.** Same as Figure 6-2a, except for San Diego. .... 73

- Figure 6-3a.** Composite H700 anomaly plots for DJF based on the starting day (left column) and ending day (right column) of persistent strong inversion episodes lasting 5 days or longer at Oakland. Plots are shown for 3 days prior and 2 days after the start day and 2 days prior and 3 days after the ending day..... 75
- Figure 6-3b.** Same as Figure 6-3a, except at San Diego..... 76
- Figure 6-4.** Composite vertical temperature profiles for 3 days before and after the starting day (left column) and ending day (right column) of persistent strong inversion episodes lasting 5 days or longer at Oakland during JJA (top row) and DJF (bottom row)..... 78
- Figure 6-5.** Composite vertical temperature profiles for 3 days before and after the starting day (left column) and ending day (right column) of persistent strong inversion episodes lasting 5 days or longer at San Diego during JJA (top row) and DJF (bottom row).... 79
- Figure 6-6.** Composite time series of surface and near-surface variables on the starting day of persistent strong inversion episodes in JJA lasting 5 days or longer. The composite time series covers an 11-day period centered on the starting day of the persistent strong inversions. Time series are shown for Oakland (top) and San Diego (bottom). ..... 81
- Figure 6-7.** Composite time series of surface and near-surface variables on the starting day of persistent strong inversion episodes in DJF lasting 5 days or longer. The composite time series covers an 11-day period centered on the starting day of the persistent strong inversions. Time series are shown for Oakland (top) and San Diego (bottom). ..... 83
- Figure 7-1.** Time series of filtered monthly mean values of (a) 12Z  $DT_{INV}$ , (b) 00Z  $DT_{INV}$ , (c) 12Z  $D\theta_{850,SJV}$ , (d) 00Z  $D\theta_{850,SJV}$ , (e) 12Z  $DZ_{INV}$ , (f) 00Z  $DZ_{INV}$ , (g) 12Z  $Z_{TOP}$  and  $Z_{BASE}$ , and (h) 00Z  $Z_{TOP}$  and  $Z_{BASE}$  based on the Oakland radiosonde data and surface temperature measurements in the San Joaquin Valley Air Basin. For each variable a six-month running mean (green line) and a five-year running mean filter (red line) are shown except for the bottom row of plots showing  $Z_{TOP}$  and  $Z_{BASE}$ , where only the five-year running mean filtered data are shown for clarity. The straight blue lines represent a linear best fit to the data for the entire 1960-2007 period. The straight black lines represent linear fits for the periods 1960-1975 and 1976-2007. The monthly means were calculated using only days when subsidence inversions were observed. Note: Data gaps in some of the filtered data curves are due to some months with no subsidence inversions..... 85
- Figure 7-2.** Time series of filtered monthly mean values of (a) 12Z  $DT_{INV}$ , (b) 00Z  $DT_{INV}$ , (c) 12Z  $D\theta_{850,SC}$ , (d) 00Z  $D\theta_{850,SC}$ , (e) 12Z  $DZ_{INV}$ , (f) 00Z  $DZ_{INV}$ , (g) 12Z  $Z_{TOP}$  and  $Z_{BASE}$ , and (h) 00Z  $Z_{TOP}$  and  $Z_{BASE}$  based on the San Diego radiosonde data and surface temperature measurements in the South Coast Air Basin. For each variable a six-month running mean (green line) and a five-year running mean filter (red line) are shown, except for the bottom row of plots showing  $Z_{TOP}$  and  $Z_{BASE}$  where only the five-year running mean filtered data are shown for clarity. The straight blue lines represent a linear best fit to the data for the entire 1960-2007 period. The straight black lines represent linear fits for the periods 1960-1975 and 1976-2007. The monthly means were calculated using only days when subsidence inversions were observed. .... 86
- Figure 7-3.** Time series of annual mean values of  $DT_{INV}$  (a, b),  $D\theta_{850}$  (c, d),  $DZ_{INV}$  (e, f), based on radiosonde data and surface temperature measurements in the San Joaquin Valley ( $D\theta_{850,SJV}$ ) and South Coast ( $D\theta_{850,SC}$ ) Air Basins. The green line shows the annual mean

data, while the red line show a five-year running mean. The straight blue lines represent a linear best fit to the data for the entire 1960-2007 period. The straight black lines represent linear fits for the periods 1960-1975 and 1976-2007. The annual means were calculated using only days when radiation inversions were observed at 12Z..... 96

**Figure 7-4.** Time series of monthly frequency of strong and weak inversions at Oakland (a, c) and San Diego (b, d). Red curves show the frequency of strong inversions while the blue curve shows the frequency of weak inversions. The data was smoothed using a six-month running mean (thin lines) and five-year running mean (thick curves) filters. The straight lines represent a linear best fit. Strong inversions are defined when  $DT_{INV}$  exceeds the third quartile and weak inversions are defined when  $DT_{INV}$  is less than the first quartile value. Quartiles were calculated for each calendar month using detrended daily values of  $DT_{INV}$  derived from radiosonde measurements over the 1960–2007 period at each site. .... 97

**Figure 8-1.** The four leading cluster patterns of monthly mean 500 hPa geopotential height anomalies for the 1960-2007 period. Also shown for each pattern are the mean annual cycle (red curves) and annual mean time series (solid blue curves) of the frequency of occurrence. The long-term trends are illustrated by the dashed blue lines. .... 103

**Figure 8-2.** The six leading cluster patterns of monthly mean 700 hPa vertical velocity anomalies for the 1960-2007 period. Also shown for each pattern are the mean annual cycle (red curves) and annual mean time series (solid blue curves) of the frequency of occurrence. The long-term trends are illustrated by the dashed blue lines. .... 105

**Figure 8-3.** Comparison of inversion magnitude anomalies from observations (black), regressions using uncentered pattern correlations (red), and regressions using centered pattern correlations (blue) within bins of the normalized mean 500 hPa anomaly. The number of months within each bin is shown by the dashed grey line and the crosses denote the midpoints of each bin. .... 110

**Figure 8-4.** Future changes in inversion strength based on regression estimates for the San Joaquin Valley (left column) and South Coast (right column) Air Basins for each 3-month season as well as an annual mean. Results shown have been averaged over the six climate models and over a 40-year historical period (1960-1999) and three 30-year future periods. Results are based on the two emission scenarios B1 (blue curves) and A2 (red curves). The error bars on each curve denote the standard deviation between 30-year means from the six climate models within each time period..... 114

**Figure 8-5.** Evolution of the average pattern correlation between climate model fields and the H500' (top) and O700' (bottom) cluster patterns. The pattern correlations were averaged over the six climate models and three 30-year periods spanning 2010-2099 as well as the 40-year 1960-1999 historical period. Note: the scale of the y-axis variable differs between the two plots..... 116

**Figure 8-6.** The average standard deviation within model fields associated with each H500' (top) and O700' (bottom) cluster pattern. The standard deviations were averaged over the six climate models and three 30-year periods spanning 2010-2099 as well as the 40-year 1960-1999 historical period..... 117

**Figure 8-7.** Frequency of monthly mean inversion magnitude anomalies from observations (grey), and regressed estimates during historical period (blue) and future period (red).  
..... 120

**Figure 8-8.** Future changes in inversion strength based on direct model estimates for the San Joaquin Valley (left column) and South Coast (right column) Air Basins for each 3-month season as well as an annual mean. Results shown have been averaged over the six climate models and over a 40-year historical period (1960-1999) and three 30-year future periods. The error bars on each curve denote the standard deviation between 30-year means from the six climate models within each time period..... 122

**LIST OF TABLES**

**Table 2-1.** Maximum/Minimum inter-station  $\theta_{2M}$  correlations for both daily values and monthly means. Surface temperatures are from available cooperative observer stations within the South Coast and San Joaquin Valley Air Basins. .... 36

**Table 2-2.** Correlations of  $T_{850}$  between radiosonde locations for both daily values and monthly means. No overlap (NO) indicates there were less than 30 days in common between a particular station pair. .... 36

**Table 4-1.** Correlation of daily values from 1960–2007 Oakland 00Z radiosonde measurements. The correlations were calculated using only days when a subsidence inversion was observed in the radiosonde data. The various time series were detrended prior to calculation. .... 51

**Table 4-2.** Correlation of monthly means from 1960–2007 Oakland 00Z radiosonde measurements. The monthly means were calculated using only those days when a subsidence inversion was observed in the radiosonde data. The various time series were detrended prior to calculation. .... 51

**Table 4-3.** Correlation of daily values from 1960–2007 San Diego 00Z radiosonde measurements. The correlations were calculated using only days when a subsidence inversion was observed in the radiosonde data. The various time series were detrended prior to calculation. .... 52

**Table 4-4.** Correlation of monthly means from 1960–2007 San Diego 00Z radiosonde measurements. The monthly means were calculated using only those days when a subsidence inversion was observed in the radiosonde data. The various time series were detrended prior to calculation. .... 52

**Table 5-1.** Correlations between monthly mean values of local SST and various inversion measures at Oakland and San Diego. Correlations greater than 0.19 at San Diego and 0.22 at Oakland are significant at the 95% confidence level. .... 67

**Table 6-1.** Average value of persistence parameter PV. .... 69

**Table 7-1.** Correlation between 1960–2007 filtered monthly means: Inversion measures vs. SST indices. Monthly means of the inversion measures are for subsidence inversions only. The time series were detrended and then filtered using a 12-month running mean. Correlations greater than 0.28 are significant at the 95% confidence level. .... 87

**Table 7-2.** Correlation of daily values from 1960–2007 Oakland 00Z radiosonde measurements. The correlations were calculated using only days when a subsidence inversion was observed in the radiosonde data. The various time series were detrended prior to calculation. .... 92

**Table 7-3.** Correlation of monthly means from 1960–2007 Oakland 00Z radiosonde measurements. The monthly means were calculated using only those days when a subsidence inversion was observed in the radiosonde data. The various time series were detrended prior to calculation. .... 92

**Table 7-4.** Correlation of daily values from 1960–2007 San Diego 00Z radiosonde measurements. The correlations were calculated using only days when a subsidence

inversion was observed in the radiosonde data. The various time series were detrended prior to calculation. .... 93

**Table 7-5.** Correlation of monthly means from 1960–2007 San Diego 00Z radiosonde measurements. The monthly means were calculated using only those days when a subsidence inversion was observed in the radiosonde data. The various time series were detrended prior to calculation. .... 93

**Table 7-6.** Correlation of low-frequency subsidence inversion variability (five-year running mean filter) from 1960–2007 Oakland 00Z radiosonde measurements. The various time series were detrended prior to calculation. .... 94

**Table 7-7.** Correlation of low-frequency subsidence inversion variability (five-year running mean filter) from 1960–2007 San Diego 00Z radiosonde measurements. The various time series were detrended prior to calculation. .... 94

**Table 7-8.** Average number of strong inversion days per year based on time series of  $DT_{INV}$  that was not detrended. Values are given for the first and second half of the period. .... 98

**Table 8-1.** Climate models from the IPCC AR4 used in the present study. .... 99

**Table 8-2.** Mean  $D\theta_{850}$  anomaly values over those months assigned to each  $H500'$  and  $O700'$  cluster pattern. Months assigned to cluster patterns based on NCEP Reanalysis monthly mean fields over the 1960-2007 period. (Units = °C). .... 106

**Table 8-3.** Correlations and explained variance from regressions estimating monthly mean inversion magnitude anomaly. .... 109

**Table 8-4.** 12Z Inversion magnitude ( $D\theta_{850}$ ) anomaly monthly means and standard deviation of monthly means at SJVAB (top) and SOCAB (bottom) predicted from regressions using monthly mean  $H500$  and  $O700$  anomaly fields from 6 climate models and NCEP Reanalysis1. Also shown are values from observations. Values calculated over the 1960-1999 period. Separate regressions were used for the each season and the annual results are an average over all months. .... 112

## **EXECUTIVE SUMMARY**

### **Background**

Concentration of several key air pollutants (ozone, secondary particulate matter) depend strongly upon the vertical gradient of temperature (e.g. inversion strength) in the lower atmosphere. Variations in inversion strength and other inversion characteristics in California are driven by natural processes over time scales from synoptic to decadal periods, and can be investigated using observational records over the past several decades. Additionally, virtually all climate model projections indicate that California's climate will warm as greenhouse gases continue to accumulate in the atmosphere. Based upon recent runs over a variety of models and greenhouse gas emissions scenarios, potential warming over California during the 21<sup>st</sup> Century would range from about 2°C to 5°C (change of temperatures in 2100 relative to recent 1961-1990 historical climatology). Because the magnitude of these changes may rival or exceed the magnitude of natural year-to-year climate variability in California, these changes could have significant consequences on the production and buildup of air pollutants in California's air basins. Thus, a better understanding of future changes in the temperature structure, including low level inversions and the associated atmospheric structure is crucial to preparing for regional air quality problems in California over the next several decades.

### **Methods**

Historical observations from 1960-2007 are used to examine inversion characteristics on diurnal, synoptic, seasonal, and interannual time scales. Using a combination of radiosonde and surface-based observations, inversions measures are derived for the San Joaquin and South Coast Air Basins. For this work, inversions are classified into two categories: i) surface based inversions that are made up primarily of radiation inversions; and ii) "elevated" inversions consisting of both subsidence and marine air inversions or a combination of the two (the term elevated is used as the region where temperature increases with height is not in contact with the surface). Subsidence and marine air inversions are grouped together because a) these two types of inversions are difficult to distinguish using radiosonde measurements, the primary means of inversion identification, and b) climate model simulations lack the resolution to distinguish between subsidence and marine air inversions and this necessitates the examination of them as one category.

Inversions are characterized from radiosonde vertical temperature observations by the height of the inversion top and base, and also by the thickness and temperature difference between the inversion top and base.

Analysis techniques included correlations, cluster analysis, and compositing based upon strong and weak inversions. Diagnostics included linkage between fluctuations in inversion characteristics and local and large-scale measures from the Reanalysis data set.

Results from reanalysis models are used to determine relationships between large-scale atmospheric circulation features and inversion strength and persistence. These relationships are then used to develop regression models that use atmospheric circulation patterns to predict the monthly mean inversion strength at both the San Joaquin and South Coast Air Basins. Cluster pattern analysis is used to characterize the atmospheric circulation patterns and as a means of relating historical patterns to patterns projected by the climate models. Estimates of future inversion strength at each air basin are produced using the regression models and future climate projections from six global climate models using the A2 (less optimistic) and B1 (more optimistic) emission scenarios.

### **Limitations**

1. There is only a sparse set of historical vertical air profiles on long-term time scales. Radiosonde measurements with consistent multi-year records are only available at coastal locations in California. To help to offset this limitation, upper-air temperature measurements from the coastal radiosondes are combined with surface measurements within the air basins to derive long-term historical estimates of inversion characteristics within these air basins. Additionally, the lack of high-quality long-term surface temperature measurements within individual air basins limits the characterization of inversions to estimates of a basin wide average.
2. All types of elevated near-surface inversions (mainly subsidence and marine air inversions) are combined into a single category, which for brevity are called "subsidence inversions"

throughout this report. Subsidence inversions are relatively large-scale while marine air inversions are limited primarily to coastal areas and some inland valley sites. The varying influence of marine air inversions can create large differences in inversion structure within an individual air basin.

3. Global climate models (GCM's) have coarse horizontal and vertical resolution and relatively crude representations of some of the important physical processes that affect the temperature structure near the surface. Thus, the large-scale information from these GCMs must be downscaled using dynamical or statistical methods to evaluate possible changes in low level inversion characteristics in California air basins. These downscaling techniques provide useful estimates, but are only approximations of the potential changes that may occur in these regional and local air basins.

## **Results**

Radiosonde records demonstrate that inversions are a common feature throughout California. Long-term records at Oakland and San Diego show inversions were present during more than 65 percent of winter days and nearly 100 percent of summer days. In this report, inversion strength is generally measured as the temperature difference between the top and base of the inversion. Strong inversions tend to be thicker, and weak inversions tend to be thinner in their vertical extent. Variations in the frequency of inversion strength are quite strong - a high inversion month may have up to 24 days with strong inversions, while a low inversion month might not have any strong inversion days.

There is a clear-cut connection between large-scale circulation features and inversion events, with strong inversions associated with high pressure systems over California and weak inversions associated with low pressure systems. A combination of physical processes associated with these circulation features, including horizontal and vertical temperature advection, is shown to affect inversion structure and variability.

Strong and weak inversions tend to cluster into multi-day episodes, as driven by synoptic-scale weather and other lower-frequency climate patterns. The frequency of occurrence of strong

inversions varies on interannual to decadal time scales. For instance at San Diego, the 1973-1977 was a period of high activity with 110 strong inversions per year, while there were only 71 strong inversions per year during 1983-1987. This variability is linked to some extent with local sea surface temperature (SST) with warmer than normal SST associated with weaker and thinner inversions. Accordingly, weaker and thinner inversion layers tend to occur in California during El Niño events and during the anomalously warm North Pacific Ocean phase of the Pacific Decadal Oscillation (PDO) and vice versa during La Niña events and during the cool PDO phase.

Strong or weak inversions tend to occur in spells as 73% of the strong inversions at the San Diego and Oakland sites occurred during episodes of two days or longer. Episodes of persistently strong inversions occur in all seasons. These episodes are often associated with a large-scale pressure wave, with teleconnections up- and downstream from an anomalous high pressure center stationed over the West Coast. Strong episodes are preceded by increasing positive geopotential height anomalies over the region and often initiated with a significant increase in the local sea-breeze circulation. Blocking mechanisms often in the form of a high amplitude wave train, are responsible for maintaining these positive height anomaly patterns and allowing persistent strong inversion episodes, sometimes lasting 5 days or longer. Most climate model projections suggest that as global temperatures rise, the inland-coastal temperature contrast will increase thereby increasing the sea-breeze circulation. Historical patterns suggest that an increased sea-breeze circulation could result in an increase in the magnitude and frequency of persistent inversion episodes.

The historical radiosonde record indicates that inversion frequency and strength undergoes variability on multi-year time scales, partly in association with large-scale climate modes such as the Pacific Decadal Oscillation. Over the entire 1960-2007 historical period, the magnitude of subsidence inversions decreased moderately, on the order of 0.5°C at both the San Diego and Oakland radiosonde locations as well as in measures designed to estimate inversion strength in the San Joaquin and South Coast Air basins. However, this decrease has not been monotonic, as from the mid-1970s, inversion strength has increased at the San Diego and Oakland coastal radiosonde sites. During this more recent period since the 1970's the inversion strength for the San Joaquin Air Basin shows a slight decrease and the South Coast Air Basin shows a slight

increasing trend. This change in trends during the mid-1970s may be due to the PDO-related climate shift that occurred at approximately the same. Although this study took care to homogenize the observed sampling rates, changes in radiosonde instrumentation and/or sampling procedures cannot be ruled out as affecting these trends, so they must be regarded with caution.

Evidence from climate model projections, including direct estimates of the vertical profiles from the simulations and linear regressions using key large-scale variables identified from historical analyses yields a tendency for inversions to strengthen throughout the next several decades.

The inversion strength is projected to grow over the course of the 21<sup>st</sup> Century. From direct estimates using the GCM temperature simulation, these increases range from 0.1°C to 0.4°C in the SJVAB and 0.2°C to 0.8°C in the SOCAB. From the large-scale patterns in the model projections, via the regression technique, these increases range from 0.2°C to 1.6°C for the SJVAB and 0.5°C to 1.3°C for the SOCAB with an uncertainty conservatively estimated at about +/- 0.6°C. The projected changes in inversion strength become substantial, relative to historical levels and variability, by 2060.

## **Conclusions**

- Low-level inversions are a ubiquitous feature in California, but vary in frequency, magnitude and structure over a range of time scales from synoptic periods to decades. Strong inversions tend to be thicker in their vertical extent, and strong inversions often persist for two or more days.
- The strength and variability of elevated inversions (includes combined effect of subsidence and marine-air inversions) at both coastal radiosonde locations and in the San Joaquin and South Coast Air Basins are strongly related to characteristic large-scale atmospheric circulation patterns and are also associated with other climate elements including anomalous Pacific sea surface temperature patterns. Very generally, stronger inversions tend to occur under patterns having anomalously high mid- and lower tropospheric geopotential height and when the eastern North Pacific Ocean surface temperatures are anomalously cool.

- Models used in this study estimate increasing trends in elevated inversion strength into the next century at both the San Joaquin and South Coast Air Basins. These estimates are basin-wide averages and do not provide any information on intra-basin variability.
- The estimated increases of inversion strength would tend to decrease air quality within both the San Joaquin and South Coast Air Basins.

### **Recommendations for Future Work**

- Continued use of regional models, with 10km or less horizontal resolution and vertical resolution sufficient to resolve boundary layer features is needed to improve the performance of simulating low level inversions and to understand processes involved in their variability. Future work using Single-Column Models (SCMs) to estimate inversions within California's air basins should use forcing derived from data able to resolve the individual air basins.
- Future work should aim to distinguish between subsidence inversions and marine-air inversions as it is likely that future trends in these individual inversion types may vary for a given air basin. Since marine-air inversions exhibit strong variability across individual air-basins, changes in this type of inversion could lead to strong changes in the variability of inversions across an air basin. The use of relatively new RWP/RASS sites within the air basins could help with this effort.
- Examining coastal-inland temperature gradients on historical time scales could be used together with large-scale circulation features to better understand inversion behavior due both marine-air advection and subsidence processes.
- The climate model projections used in this report were only available as monthly mean fields. It would be advantageous to use projected daily mean fields in order to derive estimates on variability and persistence of strong inversion events.
- Continued, perpetual monitoring of low level inversions is needed to track their frequency, strength and structural characteristics, which are seen to vary over decadal periods and may change as global climate changes develop. These observations should be made consistently

with care to minimize spurious changes from instrumental and sampling artifacts. Presently, there are no readily available decades-long observational datasets to track inversions directly within California's two problematic air basins -- the San Joaquin Valley and the South Coast (Los Angeles) Air Basins. Aircraft temperature observations could be explored to investigate whether they are suitable for monitoring inversions in these air basins.

## 1.0 INTRODUCTION

Concentrations of key air pollutants (e.g., ozone and secondary particulate matter) depends strongly upon the vertical gradient of temperature (e.g., inversion strength) in the lower atmosphere. California's setting, featuring strong subsidence along the flank of the North Pacific High and the containment within coastal and interior valleys, produces regularly occurring low-level inversions and thus chronic air quality problems. Low-level atmospheric temperature inversions (where temperature increases with height) inhibit vertical movement of air and can thereby increase the concentrations of pollutants emitted near the ground. As the climate and regional circulation patterns change, the frequency and intensity of low-level temperature inversions will likely be affected. A variation in the frequency or intensity of these low-level inversions would likely have a significant impact on air quality in California. Thus, this investigation of the historical occurrence of inversions, including their seasonal cycle and anomalous variability, will provide an important background for the assessment of how climate change might impact ambient air quality.

For this study low-level inversions are defined as occurring in the lower troposphere (usually within 3 km of the surface) and are classified into two broad categories. The first is denoted as surface-based *radiation* inversions where temperature immediately increases as one moves up from the surface. *Radiation inversions* typically occur at night when there is no incoming solar radiation to balance the surface cooling due to outgoing longwave radiation. These inversions are usually at their maximum strength around sunrise, but often survive well into the daylight hours. Large valley regions are especially prone to radiation inversions due to enhancement by cold air drainage along the slopes of the valley margins. In the San Joaquin Valley, concentrations of particulate matter, which are generally at a maximum during the winter season, are affected by the interaction of a relatively shallow radiation inversion layer and a higher valley wide inversion layer (Watson and Chow 2002).

The second category is designated as non-surface based or *elevated* inversions where the inversion layer (the region with increasing temperature with height) occurs at some distance above the surface. Types of inversions belonging to this category are *subsidence inversions* and *marine air inversions*. A *subsidence inversion* is associated with higher level, broad scale sinking

motions associated with high pressure systems along with a diminished level of turbulence within the surface mixed layer (Tennekes 1973). The combination of these processes produces an inversion layer that is elevated above the surface even during the early morning hours, whereas the base of a radiation inversion is at the surface. A marine air inversion occurs when relatively cool marine air moves inland displacing warmer upwards with an inversion layer resulting near the interface between the two air masses. The advection of marine air over land is often due to a sea-breeze circulation which can occur at all times of the year, but is most prevalent during the warm months. The advection of cool marine air inland can locally intensify and prolong existing large-scale subsidence inversions, while at other times two separate inversion layers may form. Besides coastal areas, some inland locations such as the northern San Joaquin Valley are also affected by this process due to mountain-valley topography and can be important factors in the evolution of the inversion layer and associated pollution events (Lu and Turco 1994; Wakimoto 1987). The San Joaquin Valley is subject to subsidence inversions during summer, with ozone pollution concentrations approaching that of the Los Angeles region. In the San Joaquin Valley, local wind patterns play a key role in the horizontal variability of pollution, as some of the pollutants may be transported from other regions (Dabdub et al. 1999).

In this report we do not attempt to distinguish between elevated inversions formed due to subsidence and those due to marine air advection (or a combination of the two processes). A major goal of this study was to examine inversion variability in a context that would be applicable with respect to results from large-scale global climate model projections of future climate. The spatial (vertical and horizontal) resolution of these models is too coarse to differentiate between these two types of inversions and as a result any observed or modeled occurrence of either of these inversion types is simply labeled as a subsidence inversion. Although it is beyond the scope of this study, in the future it would be useful to attempt to separate these two inversion types, since changes to either (or both) of these processes could have important implications for the air quality in particular regions.

Previous studies have examined the effect of climate on regional air quality in the central and eastern portions of the United States (Hogrefe et al. 2004; Mickley et al. 2004; Aw and Kleeman 2003). These studies used output from Global Climate Models (GCMs) to study the frequency of

large-scale weather patterns that promote the formation of air pollution events. The results of these previous studies predict that the frequency of summer ozone air pollution events in the central and eastern United States will increase in the future due to altered climate and increased background concentrations of ozone. The GCM output can also be dynamically downscaled using regional meteorological models to simulate air pollution formation with regional air quality models. Steiner et al (2006) used this approach to examine the effects of regional climate change and future emission scenarios on ozone formation in central California. Their results indicate that changes in meteorological variables associated with future climate changes would increase daily peak ozone concentrations in central California. Along similar lines, a recent study assessing effects of temperature on ozone concentrations in California's South Coast and San Joaquin air basins by Mahmud et al. 2008 indicates that projected future climate warming would increase the occurrence of days with hazardous ozone concentrations.

Although coastal daytime temperatures have remained steady or in some cases cooled (Lebassi et al 2009), as a whole, California has warmed over the last few decades, with temperature increases exceeding levels that would likely be expected solely from natural climate variability (Bonfils et al. 2008). Virtually all climate model projections indicate that California's climate will warm as greenhouse gases continue to accumulate in the atmosphere (IPCC 2007). Based upon recent runs over a variety of models and greenhouse gas emissions scenarios, potential warming over California during the twenty-first century would range from about 2°C to 5°C, or 3.6°F to 9°F (change of temperatures in 2100 relative to recent 1961–1990 historical climatology) (Cayan et al. 2008). In a recent report, Kleeman et al (2010) estimated projected temperature increases during the 21<sup>st</sup> century would likely have a detrimental impact on air quality in many regions of California. This degree of warming over California would be associated with significant changes in circulation and other facets of the climate over the region, as indicated by results from regional modeling studies (e.g., Snyder et al 2002; Duffy et al 2006). Because the magnitude of these changes may rival or exceed the magnitude of natural year-to-year climate variability in California, these changes could have significant consequences on the production and buildup of air pollutants in California's air basins. To build an understanding of how these factors may change, it is important to examine the available record of historical variability of low-level inversions.

The emphasis is on the two air basins of primary concern in California: the South Coast Air Basin (SOCAB) and the San Joaquin Air Basin (SJVAB) that are generally subjected to the highest air pollution levels in the state. Historical data is used to determine the climatological strength and frequency of inversions, the persistence of strong and weak inversions, as well as the relationship between different measures of inversion strength at different sites in California. The influence of interannual to decadal climate modes on the frequency and persistence of strong inversions and temporal trends in various inversion measures over the historical period are also analyzed. Finally, using relationships between large-scale circulation and inversion characteristics developed with historical data, projections of inversion strength in the San Joaquin Valley and South Coast Air Basins are produced for the time period 2010-2099.

## **2.0 DATA**

### ***2.1 Radiosonde Measurements***

Radiosonde measurements provide a detailed vertical profile of temperature, pressure, dew point, and horizontal winds, and are well suited to study low-level temperature inversions.

Radiosondes are routinely launched twice daily at stations around the world since the mid-20<sup>th</sup> century. Measurements from each radiosonde launch are collected and sorted using standards determined by the World Meteorological Organization (WMO) then translated over the Global Telecommunications System (GTS) allowing access to meteorological centers around the world (Durre et al 2006).

Radiosonde data over the United States is collected and archived by Earth System Research Laboratory (ESRL) of the National Oceanic and Atmospheric Administration (NOAA) (Schwartz and Govett. 1992). All data are subjected to a hydrostatic check procedure to detect gross inconsistencies between observed temperatures and reported heights. Routine radiosonde profiles are made twice daily at 0Z and 12Z at locations within the United States, including three sites in California: at San Diego, Vandenberg, and Oakland. These observations date from 1960 to present (some data exists prior to 1960 but are not used in this study due to uncertainties and irregular launch times). In addition to the three primary sites, parts of this study also included some less-continuously sampled radiosonde observations from Long Beach, Santa Monica, and

Merced. Figure 2-1 shows the location of the California radiosonde sites and the proximity to the main air basins of interest in this study.

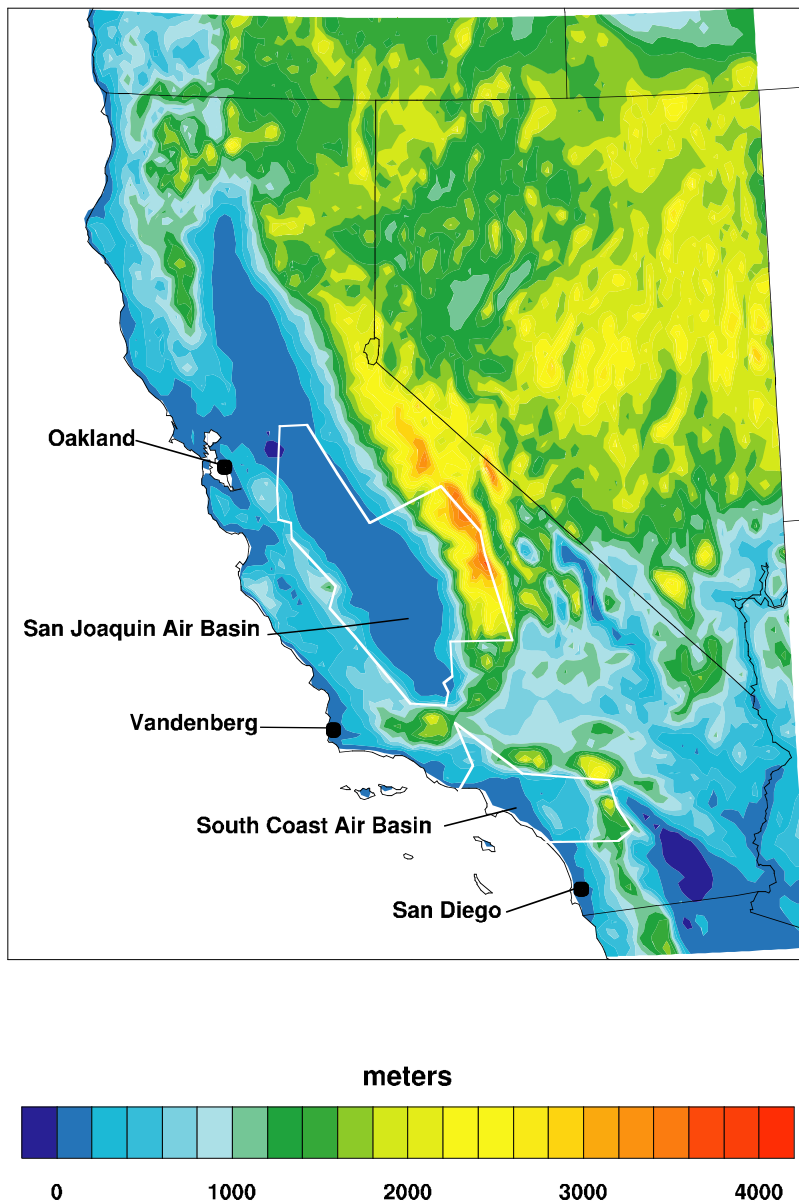


**Figure 2-1.** Map of California denoting the radiosonde locations at Oakland, Vandenberg, and San Diego. Also shown on the map are the approximate boundaries of the San Joaquin Valley and South Coast Air Basins. The color contours indicate height above sea level (meters).

The site of the San Diego radiosonde observation moved in 1989 from Montgomery Field to Miramar Naval Air Station. The distance between the old and new sites is about 6 kilometers (km), and the difference in elevation is 23 meters (m). Both Montgomery Field and Miramar

Naval Air Station are approximately the same distance (12 km) from the Pacific Ocean. It is expected that the impact of the site move would be minimal on measured upper air temperatures due to the similar geography and proximity to the Pacific Ocean. However, the impact on the surface temperature may be more significant, as even slight changes in the local conditions at and near the surface could have an appreciable effect.

Radiosonde instrumentation and processing algorithms have undergone changes over the historical time period examined in this report. Additionally, the ESRL product is a combination of radiosonde data from two sources - the first from the GTS and the second from the National Climatic Data Center (NCDC) also known as the TD6201 series data (Schwartz and Govett, 1992). The instrumental and processing changes appear to have led to differences in the vertical resolution of temperature readings between the surface and the 700 hPa level at the Oakland, Vandenberg, and San Diego sites. At all three sites there was a gradual increase in the average number of temperature readings (surface to 700 hPa) from about 10 in 1960 to about 14 in the late 1980s. The number of reporting levels increased to about 20 in 1990 and then dropped dramatically to about 10 in 1998. Some of these changes in vertical resolution can be traced to the addition or removal of standard reporting levels. Other factors affecting the vertical resolution are not so easily identified and are likely due to the criteria (e.g., difference from linearity) used to determine additional significant reporting levels.

An examination of the historical radiosonde data indicates that the changes in radiosonde reporting criteria may induce a small uncertainty in the measurement of inversion characteristics (e.g. 0.2-0.5°C for  $DT_{INV}$ , see section 3 for definition of  $DT_{INV}$ ). These changes noted above are not expected to have a significant impact on the identification of individual strong or weak inversions. However they could influence the interpretation of long-term trends in inversion characteristics that is addressed in section 7.

To address this variability in vertical resolution, the radiosonde records were re-constructed using a consistent set of standard reporting levels and consistent criteria used to include additional levels for the entire time period from 1960-2007. This re-constructed radiosonde data set was used in the derivation of the long-term trends discussed in section 7. The reconstructed

data set examined all the levels reported in the original radiosonde report and was produced using the following steps:

1. Include the standard levels at 1000, 950, 900, 850, 800, 750 and 700 hPa and at the surface.
2. Include levels that denote an inversion where  $\Delta P > 20 \text{ hPa}$  or  $\Delta T > 2.5^\circ\text{C}$  or  $|\Delta \text{RH}| > 10\%$ . These values were determined by examining all radiosonde records within the 1960-2007 period on a year-by-year basis and noting the minimum  $\Delta P$ ,  $\Delta T$ , and  $\Delta \text{RH}$  demarking an inversion was for each year. The yearly values varied as reporting criteria changed during the 1960-2007 period. These values above were found to be the largest used within the 1960-2007 data set. By using the maximum values, inversions from all radiosonde records during the 1960-2007 period can be identified using a consistent set of criteria.
3. The levels denoted in (1) and (2) are termed "significant levels". The remaining levels in the original radiosonde report that were between the significant levels were then examined. For each of these levels, a difference from linearity relative to the significant levels was calculated. The level with the greatest difference from linearity (GDL) was included as a new significant level if  $\text{GDL} > 1.0^\circ\text{C}$ . This was repeated until there were no additional new levels with  $\text{GDL} > 1.0^\circ\text{C}$ .

The levels described above were selected on the basis of being the least restrictive levels employed throughout the 1960-2007 period. As a result, some levels in the original radiosonde report were not included in the reconstructed data set. Removing these levels makes the reconstructed data set more consistent and thus more suitable for capturing natural variability, including long-term trends, across the entire 1960-2007 historical period.

## ***2.2 Surface Temperature Measurements***

Surface temperature measurements from the soundings in San Diego and Oakland were not used in the analysis of long-term variability because they are generally not representative of surface temperature conditions in the South Coast Basin and San Joaquin Valley. Additionally, the sounding record in San Diego suffers from inhomogeneities due to several site changes. Unfortunately, there are no single-site records of hourly temperature observations that extend over the entire time period. The only homogeneous long-term daily surface temperature

measurements available are maximum ( $T_{MAX}$ ), minimum ( $T_{MIN}$ ), and mean temperature from the Global Historical Climatology Network (Version 2) (GHCN2) (Peterson and Vose 1997). The GHCN2 data in California come from NOAA's Cooperative Observing stations that experienced very few and very small changes in location over time. Peterson and Vose (1997) describe statistical methods that were used to detect and correct inhomogeneities in the monthly mean GHCN2 station time series. They adjusted the station time series by adding or subtracting a correction factor for each month. Unlike the case for monthly mean values, daily values of  $T_{MAX}$  and  $T_{MIN}$  in the GHCN2 did not include any adjustments for inhomogeneities. We therefore added or subtracted the GHCN2 monthly correction factor for all days in the respective month. After doing so, the daily GHCN2  $T_{MAX}$  and  $T_{MIN}$  station time series no longer had inhomogeneities (to the extent that the monthly correction factors were reliable). A few stations that experienced large or highly variable adjustments were discarded. Long-term trends for adjusted and non-adjusted time series exhibited little difference.

Since the daily maximum temperature typically occurs in the afternoon and the daily minimum temperature typically occurs shortly before sunrise,  $T_{MAX}$  in Pacific Time generally occurs close in time to 00Z and  $T_{MIN}$  in Pacific Time generally occurs close in time to 12Z. A difference between surface observing time for  $T_{MAX}$  and  $T_{MIN}$  and sounding observing on the order of a couple hours should not matter much, because the diurnal cycle in temperature above the boundary layer is small. For the purposes of our study, it is beneficial that the time of surface maximum temperature generally corresponds to the time of day when the boundary layer is least stable and the time of surface minimum temperature generally corresponds to the time of day when the boundary layer is most stable.

The nominal observing procedure is that the maximum and minimum temperatures occurring in the 24-hour period prior to the time of observation are reported as  $T_{MAX}$  and  $T_{MIN}$ . Observing times range from 6 local time (LT) to 18 LT. Irrespective of observing time,  $T_{MIN}$  will almost always correspond to the minimum during the previous night. That is not the case for  $T_{MAX}$ , which could correspond to the maximum temperature during the previous local day for a morning observing time or the maximum temperature during the same local day for a late afternoon observing time. Unfortunately, information on observing time is uncertain, and it

moreover appears that some stations reported  $T_{MAX}$  as maximum temperature that occurred several hours after a nominal morning observing time. The appropriate coordinated universal time (UTC) day on which to assign a  $T_{MAX}$  measurement varied across the record, and was assigned on a monthly basis. This was determined from correlations at various lead/lags were calculated between  $T_{MAX}$  and 00Z 995 sigma level temperature ( $T_{995}$ ) interpolated to the station location from the National Centers for Environmental Prediction (NCEP) Reanalysis. These correlations were calculated for each month of the year, and the results indicated that there were multi-year blocks of time where  $T_{MAX}$  had best correspondence with 00Z  $T_{995}$  from the same UTC day (previous local day) and other blocks of time where  $T_{MAX}$  had best correspondence with 00Z  $T_{995}$  from the following UTC day (same local day). Errors in the assignment of  $T_{MAX}$  day should have minimal impact on the results since the decorrelation time for  $T_{MAX}$  is on the order of 7–13 days.

For purposes of better comparability, temperatures from the soundings were converted to potential temperature using values of 00Z and 12Z NCEP Reanalysis sea level pressure interpolated to the station location. Station temperature was converted to potential temperature to avoid biases due to stations being located at different altitudes (e.g., stations at higher elevations would have systematically colder temperature than stations at lower altitude). Values of 00Z and 12Z NCEP Reanalysis sea level pressure values were interpolated to the station location and converted to pressure at the elevation of the station using the assumption of a  $6.5^{\circ}\text{C km}^{-1}$  lapse rate and a mean layer temperature equal to the average near-surface temperature over the previous twelve hours. This method is commonly used in the weather community and introduces little uncertainty relative to errors in the measurements of maximum and minimum temperature.

Regional average maximum and minimum potential temperature time series were created by separately averaging station climatologies and station anomalies. This minimized geographical biases that would have occurred when one station had missing data because spatial gradients in temperature anomalies are smaller than gradients in climatological temperature (the number of missing values was less than 4%). Daily station anomalies were calculated from a climatology made from the first five harmonics fit to the annual cycle. A regional time series was created for

the South Coast Air Basin using stations at Chula Vista, Irvine Ranch, Pasadena, and Redlands, while a time series representative of the San Joaquin Valley was constructed with station data from Wasco, Lemon Cove, Hanford, Fresno, Merced, and Lodi. These stations were selected based primarily on availability of locations with consistent, long-term temperature records. Many stations were eliminated from consideration due to gaps of missing data and/or discontinuities in the data. The final set of stations was selected based on geographical considerations that attempted to provide uniform coverage throughout each air basin. Although the Chula Vista site is not within the boundaries of the South Coast Air Basin, it is included because it lies nearby, and there is a lack of stations with long-term records.

### ***2.3 Reanalysis Data***

Data from the NCEP Reanalysis 1 product (Kalnay et al. 1996) are used in this study to describe the large-scale circulation patterns which we associated with the strength and frequency of inversions in California. The NCEP Reanalysis project assimilates available past observational data into a state-of-the-art atmospheric model to produce dynamically consistent data on a global grid with a horizontal resolution of 2.5 degrees and 17 vertical pressure levels. The data has a temporal coverage of 1948 to present at a six-hour resolution.

### ***2.4 Regional Atmospheric Model Data***

In the present study, data from the California Reanalysis Downscaling at 10 km (CaRD10) are also used to provide domain-wide estimates of inversion strength. Data from NCEP Reanalysis 1 for the period 1948–2005 were dynamically downscaled to 10-km resolution using the Regional Spectral Model (RSM), called the CaRD10 dataset (Kanamitsu and Kanamaru 2007; Kanamaru and Kanamitsu 2007). The downscaled near-surface wind and temperature data were found to be a better fit to station observations within this region than to the large-scale reanalysis winds and temperatures used to force the regional model. The CaRD10 data also fit observations better than those from the regional data assimilation North American Regional Reanalysis (Mesinger et al. 2006; Kanamaru and Kanamitsu 2007). The CaRD10 near-surface data and free atmospheric data on 17 vertical pressure levels are available. The data have a temporal coverage of 1948 to 2005 at hourly resolution.

## ***2.5 How Representative are Oakland and San Diego Radiosonde Measurements of Conditions in Other Air Basins?***

Historical sounding records in California are restricted mostly to coastal or near-coastal sites in Oakland, San Diego, and to lesser extent, at Vandenberg Air Force Base. Are the thermal structure and inversion characteristics at these few long-term locations a reasonable representation of the meteorological conditions in other key air basins in the state, in particular where the air quality is poorest (i.e., San Joaquin and South Coast Air Basins)? To this end, it will be seen below that the diurnal and seasonal nature of the frequency and strength of subsidence inversions and of radiation inversions is quite similar across the three sounding locations. The anomalous variability, on daily and monthly time scales, is well correlated across several locations (see Tables 2-1 and 2-2). Surface temperatures, taken from available cooperative observer stations in Southern California and from the San Joaquin Valley, are well correlated, as will be demonstrated in Table 2-1. For Southern California, the weakest inter-station daily anomaly correlation ( $r$ ) is 0.54 (summer  $T_{MAX}$  for Chula Vista-Redlands) and the strongest correlation is 0.89 (winter  $T_{MAX}$  for Pasadena-Redlands). For the San Joaquin Valley, the weakest daily correlation is 0.64 (summer  $T_{MIN}$  for Hanford-Lodi) and the strongest is 0.94 (summer  $T_{MAX}$  for Fresno-Lemon Cove). Longer time scale surface temperature variations, formed from monthly and annual mean anomalies, are also generally well-correlated, with correlations ranging from 0.49–0.91 (monthly) and 0.34–0.89 (annual) for Southern California and 0.36–0.94 (monthly) and 0.56–0.86 (annual) for the San Joaquin Valley. The 850 hPa temperatures from the extensive records from San Diego, Oakland, and Vandenberg, along with more limited records from Long Beach (1949–1956), Santa Monica (1956–1965), and Merced (1952–1963, with many gaps), are even more highly correlated, as demonstrated in Table 2-2. Daily 850 hPa temperature anomalies at San Diego and the Los Angeles stations have a 0.94 (winter) and 0.92 (summer) correlation, and daily anomalies at Oakland and Merced have a 0.94 (winter) and 0.88 (summer) correlation. This clearly supports the applicability of San Diego 850 hPa temperature to the South Coast Basin and the Oakland 850 hPa temperature to the San Joaquin Valley. The daily correlation between San Diego and Oakland is 0.75 (winter) and 0.65 (summer), indicating that 850 hPa temperature patterns are spatially coherent over California. Monthly and annual 850 hPa temperatures produce about the same level of correlation.

**Table 2-1.** Maximum/Minimum inter-station  $\theta_{2M}$  correlations for both daily values and monthly means. Surface temperatures are from available cooperative observer stations within the South Coast and San Joaquin Valley Air Basins.

	Daily		Monthly	
	NDJF	JJAS	NDJF	JJAS
SOCAB $\theta_{2M}$ 00Z	0.89/0.68	0.88/0.54	0.91/0.77	0.84/0.56
SOCAB $\theta_{2M}$ 12Z	0.82/0.69	0.79/0.58	0.83/0.76	0.80/0.64
SJVAB $\theta_{2M}$ 00Z	0.90/0.73	0.94/0.83	0.93/0.85	0.90/0.80
SJVAB $\theta_{2M}$ 12Z	0.87/0.72	0.83/0.64	0.92/0.83	0.83/0.50

Note:  $\theta_{2M}$  is potential temperature at two meters above the surface—a proxy for surface air temperature.

**Table 2-2.** Correlations of  $T_{850}$  between radiosonde locations for both daily values and monthly means. No overlap (NO) indicates there were less than 30 days in common between a particular station pair.

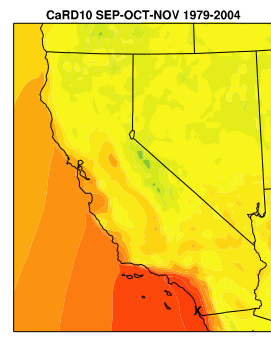
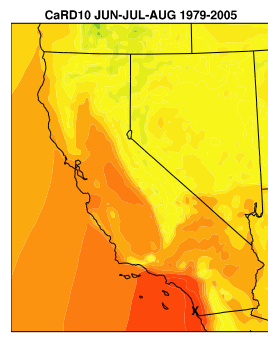
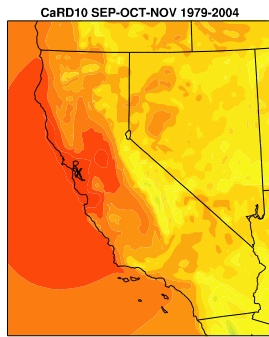
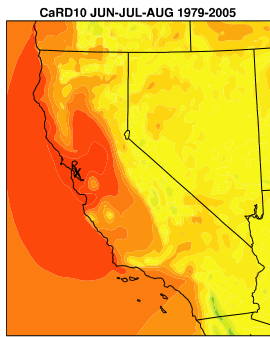
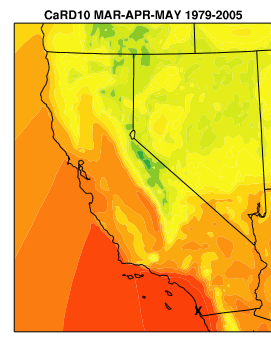
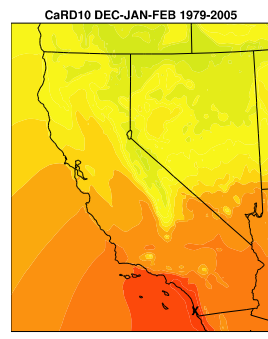
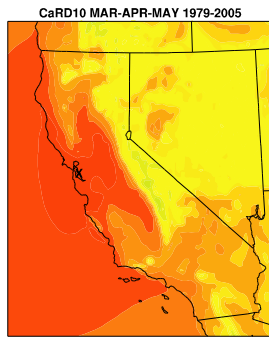
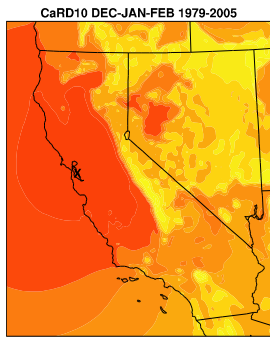
Daily Values								
	Los Angeles		Vandenberg		Oakland		Merced	
	NDJF	JJAS	NDJF	JJAS	NDJF	JJAS	NDJF	JJAS
San Diego	0.94	0.92	0.88	0.84	0.75	0.65	0.83	NO
Los Angeles			NO	NO	0.82	0.73	0.87	NO
Vandenberg					0.87	0.85	NO	NO
Oakland							0.94	NO

Monthly Means								
	Los Angeles		Vandenberg		Oakland		Merced	
	NDJF	JJAS	NDJF	JJAS	NDJF	JJAS	NDJF	JJAS
San Diego	0.93	0.88	0.92	0.88	0.83	0.73	0.77	NO
Los Angeles			NO	NO	0.85	0.72	0.81	NO
Vandenberg					0.90	0.88	NO	NO
Oakland							0.97	NO

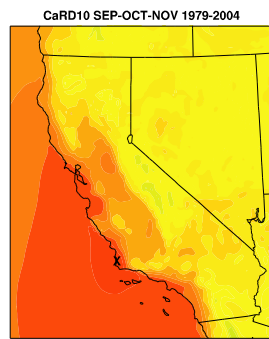
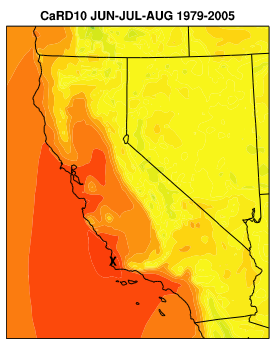
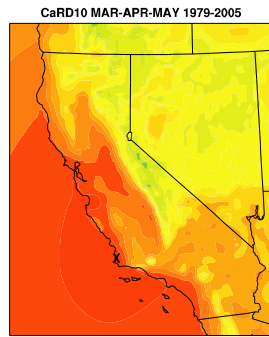
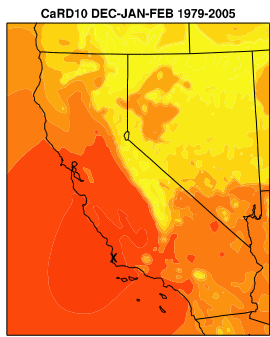
NDJF = November, December, January, February; JJAS = June, July, August, September

The high-resolution CaRD10 product also provides insight into this question of the spatial representativeness of the atmospheric soundings. While a model product, CaRD10 does successfully simulate regional-scale weather patterns such as Santa Ana wind events and Catalina Eddy circulation, thus providing some confidence in the realism of the data. Figure 2-2 contains the spatial coherence of inversion strength as measured by daily  $D\theta_{850}$  values from the CaRD10 data set, where  $D\theta_{850}$  is the potential temperature difference between 850 hPa and the surface (2 meters). These maps were produced by cross-correlating daily  $D\theta_{850}$  values at Oakland, Vandenberg, or San Diego to all other grid points.



(A)  $D\theta_{850}$  Cross-correlation at Oakland

(B)  $D\theta_{850}$  Cross-correlation at San Diego



(C)  $D\theta_{850}$  Cross-correlation at Vandenberg

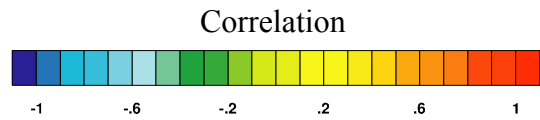


**Figure 2-2.** Plots showing cross-correlation (spatial coherence) of daily mean values of  $D\theta_{850}$  from the CaRD10 product relative to locations at (a) Oakland, (b) San Diego, and (c) Vandenberg.

Relatively strong correlations linking  $D\theta_{850}$  at Oakland with  $D\theta_{850}$  in neighboring areas are observed, to varying degrees, in all seasons. These strong correlations extend along the northern and central California coastal areas as well as into the Sacramento and San Joaquin Valleys. The extension into the interior valleys is strongest during winter and weakest in summer and fall. There is also strong spatial coherence of  $D\theta_{850}$  at Vandenberg into the San Joaquin Valley during winter, but it is significantly weaker during the other seasons, compared to  $D\theta_{850}$  at Oakland. While the spatial coherence of  $D\theta_{850}$  at San Diego is much more limited than at either Oakland or Vandenberg, it does maintain moderate-to-high values in the South Coast Air Basin during all seasons. Both Oakland and San Diego  $D\theta_{850}$  are well correlated with  $D\theta_{850}$  variations offshore from these locations. This analysis indicates that radiosonde measurements from Oakland and San Diego are appropriate to infer inversion measures within the San Joaquin Valley and South Coast Air Basins, respectively. Note that  $D\theta_{850}$  is not meaningful in mountainous regions because the surface is near or above the 850 hPa level.

## ***2.6 Climate Model Projections***

Climate model projections are obtained from several IPCC AR4 GCM simulations using a lower emissions (SRES B1) and a medium-high emissions (SRES A2) scenario. A total of six individual model simulations are used. These are the same emission scenarios and models that have been adopted by the State of California climate change scenarios assessment (Cayan et al 2009). There are other plausible model simulations that project lower and higher levels of future warming over California during the 21<sup>st</sup> Century. Criteria used in selecting these climate models included having, in their historical climate simulations, a reasonable similarity to regional climate over California, including their spatial structure, seasonality, and properties of their interannual climate variability, and also providing an archive of the model simulations at daily resolution as well as at the monthly level of sampling (see Cayan et al 2008; Cayan et al 2009). It should be noted that the results from these models are projections based on different greenhouse gas emission scenarios and should not be construed as predictions.

### 3.0 INVERSION CHARACTERISTICS AND MEASURES

#### 3.1 General Inversion Measures

A schematic illustration of a typical temperature inversion profile is shown in Figure 3-1. To quantify an inversion, several different measures are used, including the height of the base ( $Z_{BASE}$ ) of the inversion, the height of the top ( $Z_{TOP}$ ) of the inversion, the temperature at the base ( $T_{BASE}$ ) of the inversion, the temperature at the top ( $T_{TOP}$ ) of the inversion, the temperature difference across the inversion ( $DT_{INV}$ ), the depth of the inversion ( $DZ_{INV}$ ) and the temperature lapse rate within the inversion ( $DT_{INV}/DZ_{INV}$ ). Accurate computation of these quantities requires vertical profiles of temperature at a sufficiently high sampling interval to resolve these temperature differences. The potential temperature difference ( $D\theta_{850}$ ) between 850 hPa and the surface (2 meters) as well as  $\theta_{850}$  alone have also been used (Ferreria and Shipp 2005) as measures of inversion strength. This paper uses both  $DT_{INV}$  and  $D\theta_{850}$  to measure the strength of the inversion, where a larger positive value indicates a stronger inversion.

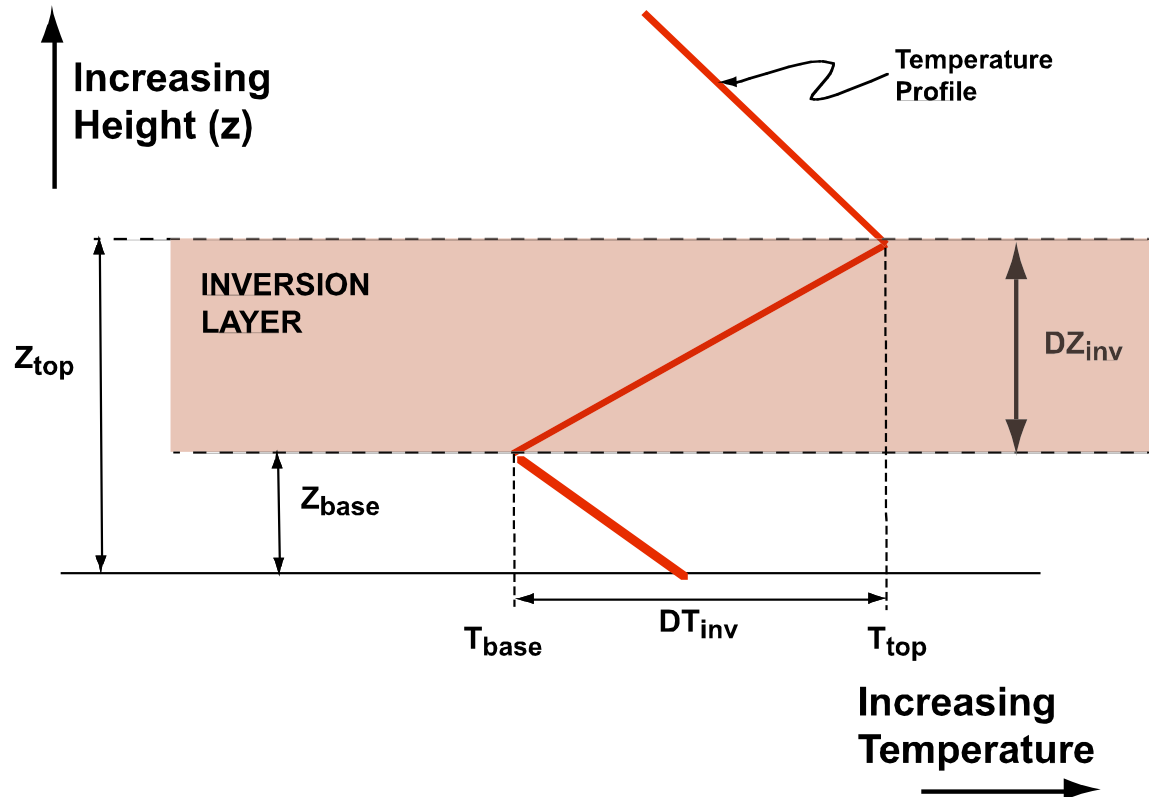


**Figure 3-1.** Schematic diagram showing some of the measures used to characterize low-level temperature inversions.

Although  $DT_{INV}$  has the advantage of being a direct measurement of inversion strength, it can only be obtained at the few sites where sounding observations are present. One would expect that temperatures within the boundary layer, in particular the inversion base temperature, to depend on surface characteristics that are highly variable throughout California. As a result,  $DT_{INV}$  may not be entirely representative of conditions away from the radiosonde sites.

While not a direct measure of a temperature inversion,  $D\theta_{850}$  can be estimated from reanalysis and surface temperature observations at a larger number of locations than  $DT_{INV}$ . The relatively large spatial coherence of temperatures above the boundary layer allows using radiosonde values of  $\theta_{850}$  along with abundant ground-based surface temperature observations to estimate  $D\theta_{850}$ . For example, this paper will often use  $\theta_{850}$  from San Diego radiosonde measurements together with surface temperature observations in the South Coast Air Basin to estimate a  $D\theta_{850}$  applicable to this air basin. These values will be denoted as  $D\theta_{850,SJV}$  and  $D\theta_{850,SC}$  depending on where the surface temperature observations were obtained, either the San Joaquin Valley Air Basin or South Coast Air Basin, respectively. Another advantage of using  $D\theta_{850}$  is that this quantity is easily obtained from the standard output of most climate models. In Section 4 we examine the spatial and temporal relationships between  $DT_{INV}$  and  $D\theta_{850}$ .

Additionally, the stability of the mid-to-lower atmosphere above the inversion layer, while not a direct measure of inversion strength, is used to help understand and interpret inversion characteristics and variability. Here the potential temperature lapse rate between 850 and 500 hPa ( $d\theta/dz_{850-500}$ ) is used to measure the mid-to-lower atmospheric stability.

Some important conventions were adopted in calculating  $DT_{INV}$ ,  $DZ_{INV}$ , and  $Z_{BASE}$ . First, the temperature profile, between the surface and 700 hPa level, is examined for temperature inversions, defined to be present when a temperature at a given altitude in the sounding was warmer than the temperature at an altitude below it. In the case when more than one inversion is observed, the inversion having the largest value of  $DT_{INV}$  is used. Subsidence inversions were defined as having a base level at least 50 meters above the surface. Radiation inversions are defined as cases when the base of the temperature inversion lies between the surface and 50

meters. The choice of 50 meters was based on the frequency distribution of inversion base height at the San Diego and Oakland sites that showed a relative minimum at this level suggesting a boundary between the two classes of inversions. As defined here, if a radiation inversion is present, it is not a subsidence inversion, although there may in fact be some cases when both classes of inversions could occur together. In most cases, subsidence inversions are examined separately from radiation inversions in this study.

### ***3.2 Measures of Strong and Weak Inversions***

Daily anomaly values of  $DT_{INV}$  from the set of all inversions (subsidence and radiation inversions together) were used to categorize the occurrence of strong and weak inversions. Anomalies were calculated by removing the climatological daily value. In computing the occurrence of strong and weak inversions, the 1960–2007 radiosonde  $DT_{INV}$  time series was detrended to remove any long-term trends that might bias the results. Long-term trends of inversion characteristics during the 1960-2007 period are discussed separately in Section 7. The detrending process simply removes any long-term linear trend that may interfere in the study of shorter term variations. Climatological monthly values of  $DT_{INV}$  were calculated from the 48 years of data. Climatological daily values were obtained by linearly interpolating between the climatological monthly values.

Quartiles were determined from the distribution of the daily anomaly values for each calendar month (approximately 48 years of data x 30 days per month = 1440 daily values per month over the 48 years of data). A day was considered to have a "strong inversion" if its daily  $DT_{INV}$  anomaly value exceeded the third quartile ( $Q_3$ ); similarly a day was identified as having a "weak inversion" if its daily  $DT_{INV}$  anomaly value was less than the first quartile ( $Q_1$ ). Thus, over the entire time series, 25% of the days were labeled as having a strong inversion and 25% of days were labeled as a weak inversion. Of course, individual months may have a strong or weak inversion frequency of more or less than 25%.

### ***3.3 Measures of the Persistence of Strong and Weak Inversions***

Persistence of different categories of strength of inversion was measured using the detrended  $DT_{INV}$  time series and quartile points described above. A persistence value (PV) was calculated for each day, where:

$$PV(i) = 0 \text{ if } DT_{INV} < Q_3 \text{ for day } i$$

$$PV(i) = N \text{ if } DT_{INV} > Q_3 \text{ for day } i, \text{ where } N \text{ is the number of contiguous previous days (including present day) where } DT_{INV} > Q_3.$$

For example, a value of  $PV(i)=3$  would indicate that  $DT_{INV} > Q_3$  for the present day  $i$  as well as the two previous days  $i-1$  and  $i-2$  and  $DT_{INV} < Q_3$  on day  $i-3$ . Larger values of PV indicate persistence (or episodes) of continuously strong inversion days. The example above defines the persistence of inversions in the fourth (highest strength) quartile, but will also be applied easily to the other three quartiles.

## **4.0 INVERSION CLIMATOLOGY AND CHARACTERISTICS**

### ***4.1 Seasonal Cycle of Inversion Frequency***

The seasonal cycles of monthly mean subsidence and radiation inversion frequency at Oakland, Vandenberg, and San Diego are shown in Figure 4-1 for both the 00Z (local 4 p.m. Pacific Standard Time, PST) and 12Z (local 4 a.m. PST) soundings. The data shown in the plots were derived from daily radiosonde measurements at these sites during the period 1960–2007. At all locations summer months are dominated by subsidence inversions. During winter, radiation inversions occur frequently (approximately 40-60% of the observations) in the early morning at 12Z, but are nearly absent in mid-afternoon at 00Z. At 12Z (4 a.m. local time) radiational cooling of the surface has just about reached a maximum, allowing radiation inversions to more easily form, while at 00Z (4 p.m. local time) solar heating has warmed the surface sufficiently to eliminate nearly all radiation inversions. For the early morning 12Z reading, the annual mean frequency of radiation inversions at Oakland, Vandenberg, and San Diego is about 32%, 43%, and 39%, respectively. This agrees reasonably well with Neiburger (1969) who estimates that radiation inversions are present in California about 40% of the time.

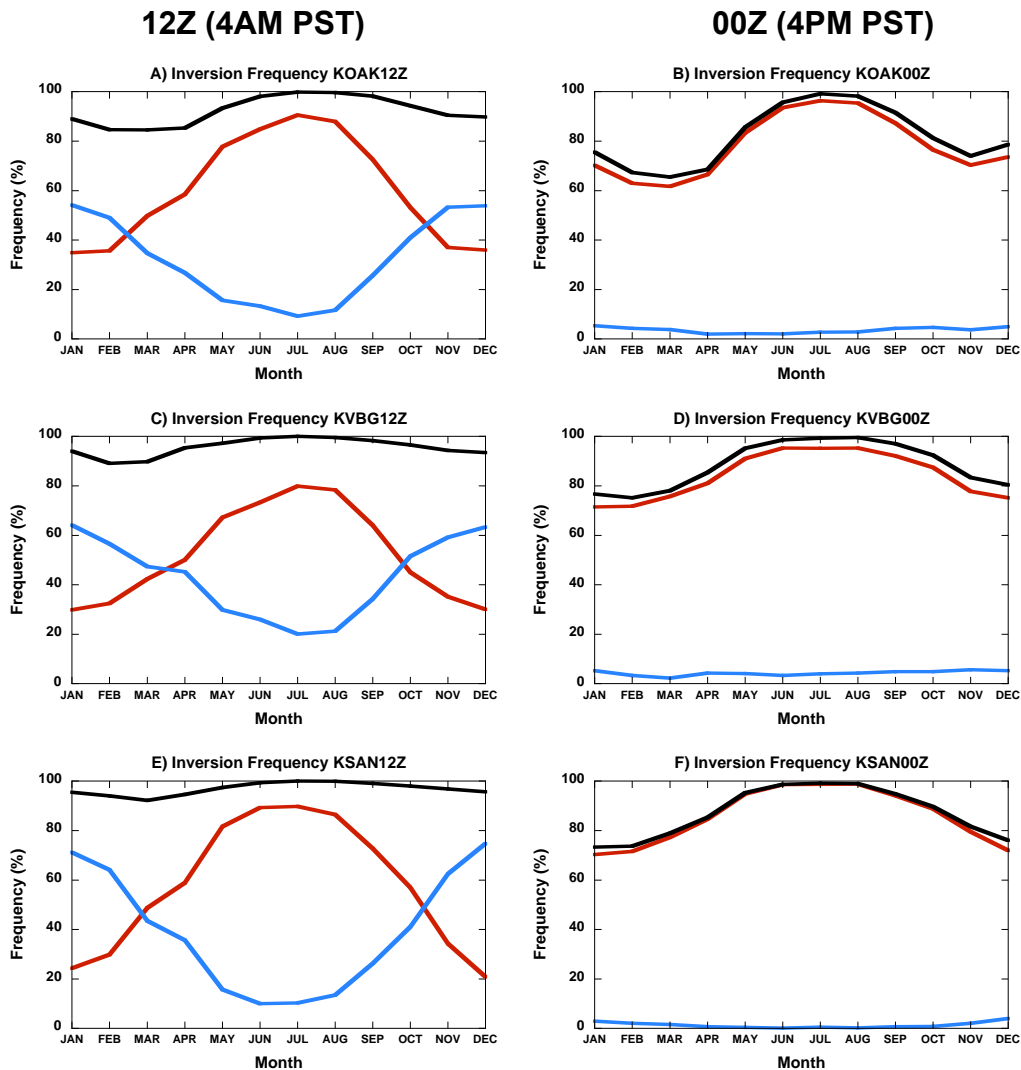


**Figure 4-1.** Monthly mean inversion frequency at Oakland (a, b), Vandenberg (c, d), and San Diego (e, f), determined from twice-daily radiosonde measurements. Subsidence inversion frequency (red curves), radiation inversion frequency (blue curves), and total (subsidence + radiation) inversion frequency (black curves) are shown separately. The data cover the period from 1960–2007.

Perhaps the most striking detail in Figure 4-1 is the high frequency of inversion occurrence (either subsidence or radiation) at all three locations throughout the year. During summer months, inversions of various magnitudes are almost always present at these sites, while during winter months low-level temperature inversions are present at least 65% of the time. Even when no inversion was present, the lower atmosphere was often quite stable. For example, 75% of the non-inversion days (00Z sounding) had regions below the 700 hPa level at least 50 hPa thick with values of  $d\theta/dz > 3.2$  degrees Kelvin per kilometer ( $^{\circ}\text{K km}^{-1}$ ) at San Diego and  $d\theta/dz > 3.4$   $^{\circ}\text{K km}^{-1}$  at Oakland.

## 4.2 Comparison of Radiation and Subsidence Inversions

At 12Z, both radiation and subsidence inversions are observed in all months at each of the coastal radiosonde sites. To illustrate the differences between the two inversion types, 30-day composite vertical profiles of temperature, specific humidity and relative humidity for both radiation and subsidence inversions at KOAK during JJA and DJF are shown in Figure 4-2. These composites were formed using the 30 days (12Z sounding) with the strongest radiation and subsidence inversions over the 1960-2008 time period during each 3-month season. Also shown in the figure are the clear-sky longwave heating rates for each set of temperature and humidity profiles using the longwave radiation parameterization of Morcrette (1988). Very similar profiles are obtained at the other two radiosonde locations and only the KOAK profiles are shown for brevity.

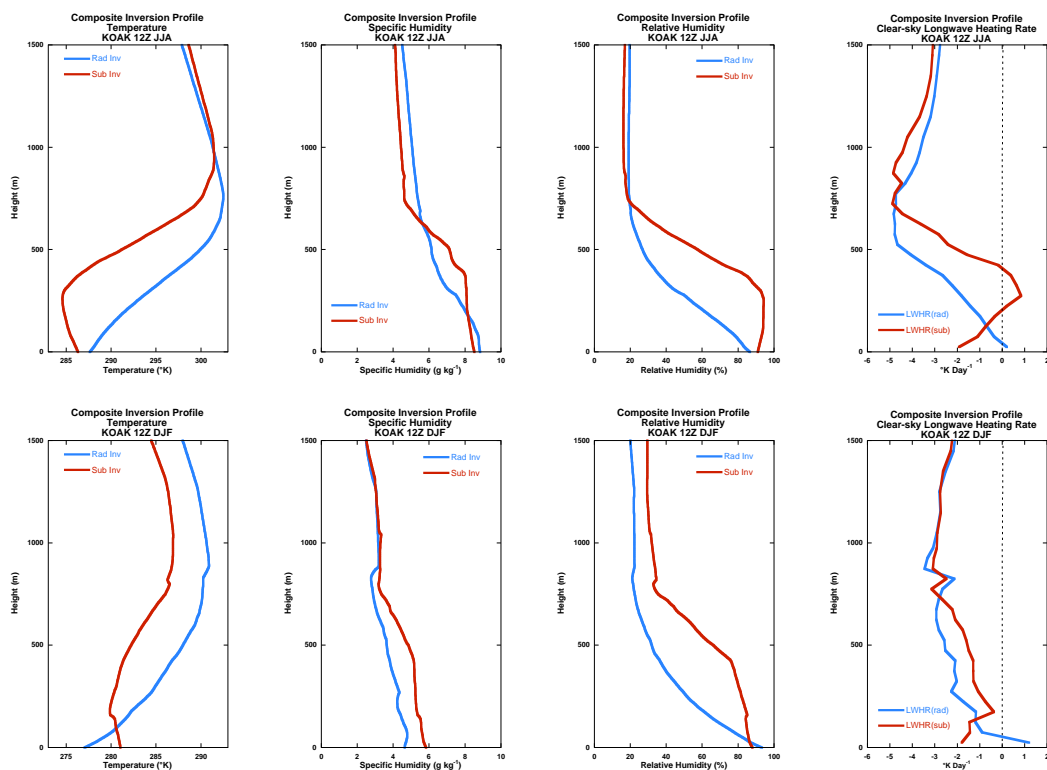


**Figure 4-2.** Composite profiles of temperature, specific humidity, relative humidity, and clear-sky longwave heat rates. The composites were formed using radiosonde data from the 30 days with the strongest radiation (blue lines) and subsidence (red lines) inversions at the Oakland radiosonde location over the 1960-2007 period. Composites are shown for the JJA (top row) and DJF (bottom row). The clear-sky longwave heating rates were calculated with the parameterization of Morcrette (1988) based on composite temperature and humidity profiles.

As expected, the 12Z composite temperature profiles for subsidence and radiation inversions are quite distinct in both seasons. The humidity profiles also show significant differences, particularly in the lowest 500 meters. It is worth noting that difference in the relative humidity profiles are due to differences in both temperature and specific humidity. In both seasons, the lower atmosphere is considerably closer to saturation during the subsidence inversion events which likely had a significant impact on cloud formation. The clear-sky longwave radiative heating rates also show significant differences in the lowest 500 meters, especially during JJA, and may also play a role in both the formation and lifetime of clouds.

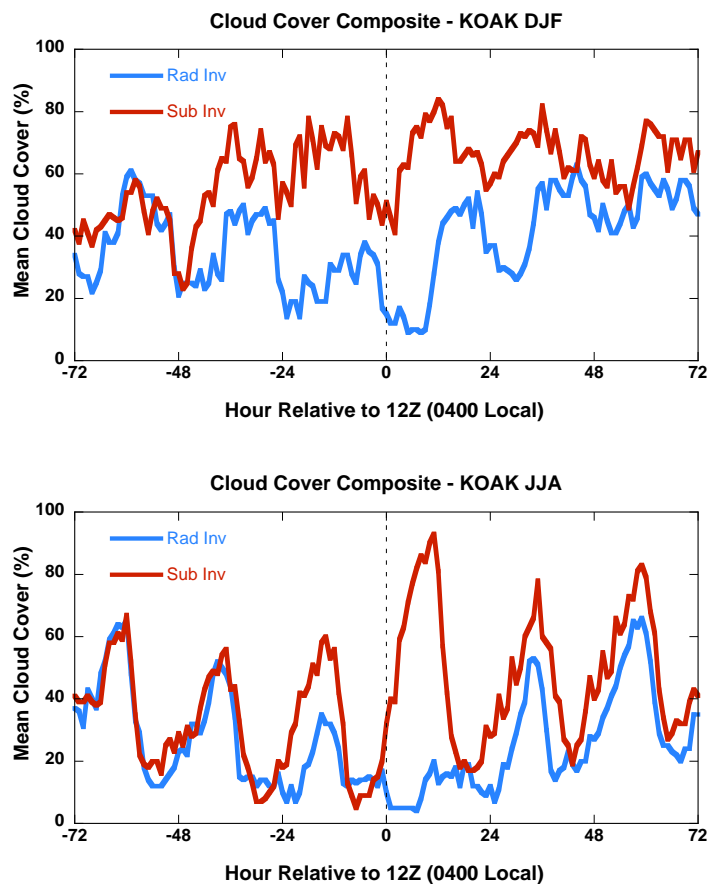


**Figure 4-3.** Composited cloud cover observations based on the 30 days with the strongest radiation (blue) and subsidence (red) inversions at the Oakland for DJF (top) and JJA (bottom). The composited cloud cover spans a 144 hour period centered at the 12Z radiosonde launch time. Cloud cover observations are from the NNDC hourly surface data set.

Each of the radiosonde sites are located at airports where hourly surface meteorological and cloud cover observations are also available (NNDC Hourly Surface Data). Figure 4-3 shows composited cloud cover observations (spanning +/- 72 hours relative to the 12Z radiosonde

launch time) based on the 30 days with the strongest subsidence and radiation inversions. During DJF, radiation inversions are associated with significantly less cloud cover compared to subsidence inversions. The reduced cloud cover during the radiation inversions is evident nearly 48 hours prior to the 12Z radiosonde launch time and extends at least 48 hours afterwards. This is consistent with less cloud cover leading to increased nighttime surface radiational cooling and the higher likelihood of radiation inversions being produced. During DJF synoptic systems advect clouds over the region which inhibits the formation of radiation inversions and making subsidence inversions more likely.

A very different pattern is observed for cloud cover during JJA where during most of the night there are relatively small values of cloud cover for both radiation and subsidence inversions. There is also a much stronger diurnal cycle in cloud cover compared to DJF. Just prior to the 12Z launch time, cloud cover increases for subsidence inversions relative to radiation inversions. In the next 12 hours after 12Z, cloud cover continues to increase for subsidence inversions but slightly decreases for radiation inversions. Of the clouds that form 12 hours after the 12Z radiosonde measurement time, more than 80% have a cloud base lower than the inversion base height. It is interesting to note that relative to the 3 days before and after the inversion measurement, cloud cover is at a maximum during the days with the strongest subsidence inversions and at a minimum during the days with the strongest radiation inversions. Since cloud cover does not significantly increase before the 12Z measurement time, it appears that cloud cover increases due to the subsidence inversion forming, unlike during DJF when the presence of clouds lead to the subsidence inversion. It also appears that there is more cloud cover associated with the strongest subsidence inversions. This suggests that stronger subsidence inversions are more efficient at capping marine air, increasing the relative humidity beneath the inversion base and thus making cloud formation more likely to occur.

The shorter time scales associated with changes in cloud cover during JJA indicate that clouds, and perhaps inversion characteristics, are determined by smaller regional processes, whereas during DJF clouds and inversion characteristics are products of larger scale synoptic processes. A possible explanation for determining whether a radiation or subsidence inversion forms in JJA may be the local wind speed, where lower wind speeds would lead to increased surface

radiational cooling and radiation inversions. Figure 4-4 shows the surface wind speeds at the KOAK site +/- 72 hours of the 12Z launch time of those days observed with the 30 largest subsidence and radiation inversions during DJF and JJA. During DJF, wind speed during subsidence inversions is greater than during radiation inversions just prior to the 12Z launch time and extending about 20 hours afterwards. However, during JJA the wind speed is larger during subsidence inversions relative to radiation inversions for at least 24 hours prior to the 12Z launch time. This would allow adequate time during the night for the wind to more thoroughly mix the lower atmosphere which reduces the surface radiational cooling and reduces (increases) the likelihood of a radiation (subsidence) inversion forming. These differences in wind speed during JJA do not appear to be caused by large-scale circulation patterns as composited geopotential heights patterns (not shown) are very similar for both radiation and subsidence inversion days. The differences in wind speeds may be due to local pressure gradients set up by contrasts in ocean and inland surface temperatures.

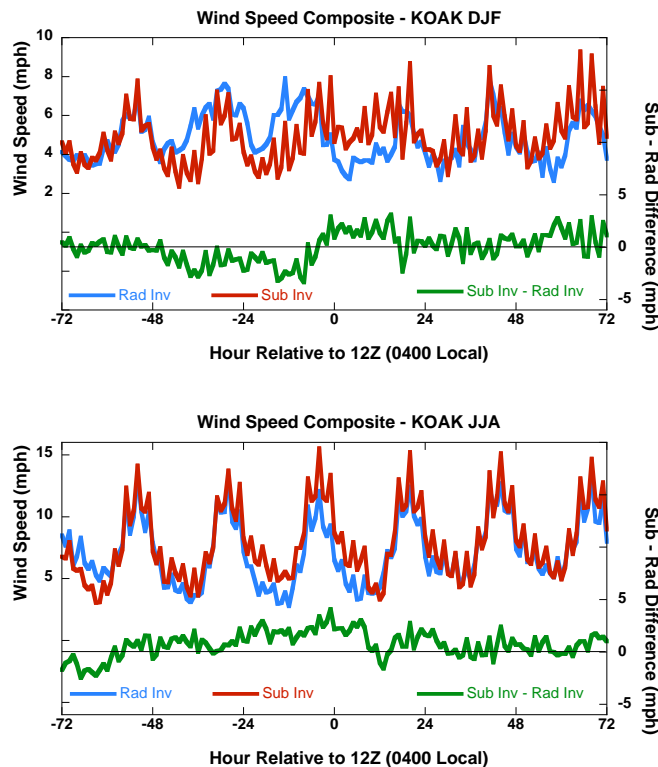


**Figure 4-4.** Composited surface wind speed observations based on the 30 days with the strongest radiation (blue) and subsidence (red) inversions at Oakland for DJF (top) and JJA (bottom). The difference between the subsidence and radiation composites is shown by the green curve. The composited wind speeds spans a 144 hour period centered at the 12Z radiosonde launch time. Wind speed observations are from the NNDC hourly surface data set.

### ***4.3 Seasonal Cycle and Variability of Subsidence Inversion Measures***

The magnitude and variability of daily values of four measures for subsidence inversions are shown in Figure 4-5 as a function of calendar month. Data are only included for those instances when a subsidence inversion was present. Data are shown for  $D\theta_{850,SJV}$  (or  $D\theta_{850,SC}$ ),  $DT_{INV}$ ,  $Z_{BASE}$ , and  $DZ_{INV}$  at both 00Z and 12Z radiosonde launch times. Recall, the  $D\theta_{850,SJV}$  and  $D\theta_{850,SC}$  measures use radiosonde 850 hPa temperature and mean surface temperature from the selected stations within the associated air basin, San Joaquin Valley or South Coast.

Throughout the year, the magnitude of both  $DT_{INV}$  and  $D\theta_{850}$  is larger at 12Z compared to 00Z. However, the seasonal variability, especially at 00Z and especially at Oakland/SJVAB is very different for  $D\theta_{850}$  as compared to  $DT_{INV}$ . The magnitude and variability of  $DT_{INV}$  at 00Z and 12Z increase during summer at all locations. In contrast,  $D\theta_{850}$  variability is at a minimum during summer, while the magnitude does not show much change over the course of the year except for the Oakland/SJVAB 00Z, when the  $D\theta_{850}$  magnitude decreases significantly. Daily values of inversion top temperature and  $\theta_{850}$  had correlations greater than 0.9 at both Oakland and San Diego, while correlations between the temperature at a height of two meters ( $T_{2m}$ ) and inversion base temperature were lower, at 0.6–0.8, although still highly significant. This indicates that the differences in seasonal and diurnal behavior between  $D\theta_{850}$  and  $DT_{INV}$  are most likely due to using regional mean surface temperatures to represent  $T_{2M}$  in the computation of  $D\theta_{850}$ .

The subsidence inversion base height ( $Z_{BASE}$ ) is lower during summer than winter and also has lower variability during the summer months than winter months—this is the case at all three locations and at both the 12Z and 00Z radiosonde launch times. Compared to  $Z_{BASE}$ , the seasonal differences in inversion depth ( $DZ_{INV}$ ) are significantly smaller, with only a slight increase in both magnitude and variability during summer.

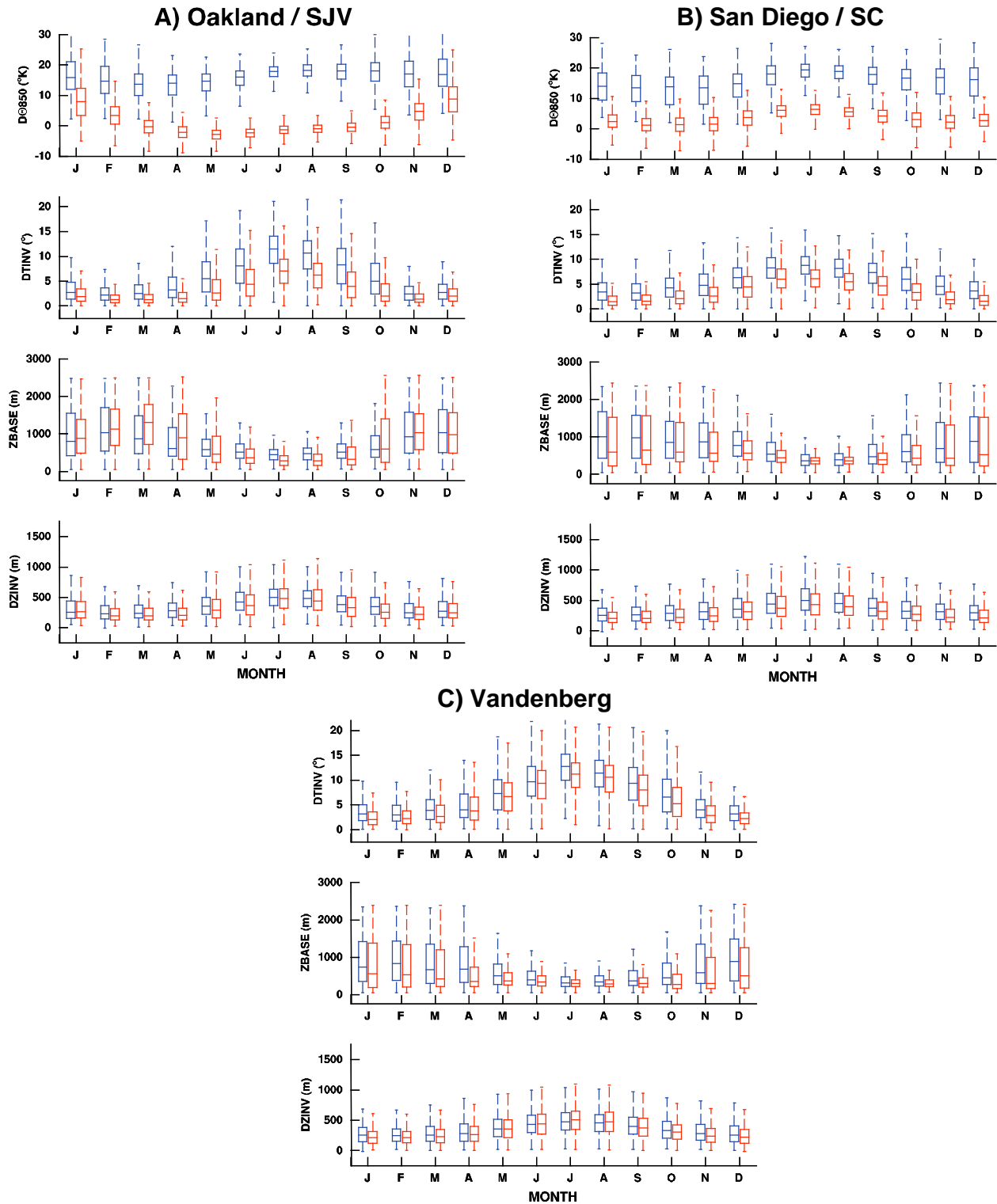


**Figure 4-5.** Box plot diagrams showing the distribution of daily values at 00Z (red) and 12Z (blue) of  $DT_{INV}$ ,  $Z_{BASE}$ , and  $DZ_{INV}$  at (a) Oakland, (b) San Diego, and (c) Vandenberg radiosonde locations. Additionally, plots of  $D\theta_{850,SJV}$  and  $D\theta_{850,SC}$  are included in the Oakland and San Diego columns, respectively. The data cover the period from 1960–2007.

#### ***4.4 Relationship Between Subsidence Inversion Measures***

Correlations between various inversion measures are displayed in Tables 4-1 to 4-4 for both daily values and monthly means. These correlations were calculated using only days when a subsidence inversion was measured, based upon the detrended time series. Results are presented at the 00Z launch time to better isolate the occurrence of subsidence-type inversions to prevent biases in monthly means from radiation inversions. Several of the measures show moderate to high correlation values ( $R > 0.5$ ,  $p < 0.01$ ). These include a moderate positive correlation between  $DT_{INV}$  and  $DZ_{INV}$  on monthly time scales, indicating that stronger/weaker inversions are also thicker/thinner in vertical extent. Additionally,  $T_{TOP}$  and  $T_{BASE}$  are highly correlated with  $T_{850}$  and to a lesser extent with  $T_{500}$ . In general, the correlations between the various temperatures decrease as the physical distance between the locations increase. The thickness of the inversion is not significantly correlated with either  $Z_{TOP}$  or  $Z_{BASE}$ , a reflection of the two height measures being so strongly correlated, and thus the difference was not too well correlated with either measure. The stability of the atmospheric layer between 850 hPa and 500 hPa is well correlated to  $T_{850}$ , but weakly correlated with  $T_{500}$ . This perhaps indicates that the dynamics driving the temperatures at the 850 hPa level are more relevant to low-level temperature inversions in California than the dynamics at 500 hPa.

To examine how well the  $D\theta_{850}$  measure represents  $DT_{INV}$ , daily anomaly values determined from radiosonde measurements at Oakland are compared in Figure 4-6 (data at San Diego is very similar). The data in this figure is only from days when a subsidence inversion was present. For these comparisons,  $D\theta_{850}$  values were computed using surface temperature from the radiosonde measurement, so that both  $DT_{INV}$  and  $D\theta_{850}$  are representative of the same location. There is a moderate-to-strong correspondence between  $DT_{INV}$  and  $D\theta_{850}$  anomalies at both Oakland and San Diego, with correlations greater than 0.7 (Figure 4-6a–b).

Higher correlations of about 0.8 are obtained if the comparison is limited to inversions with base heights less than 1000 meters as shown in Figure 4-6c,d (similar improvement is seen at San

Diego). Inversion layers above the 1000 meter level can impact the temperature at 850 hPa which acts to degrade the linear fit between these two variables.

**Table 4-1.** Correlation of daily values from 1960–2007 Oakland 00Z radiosonde measurements. The correlations were calculated using only days when a subsidence inversion was observed in the radiosonde data. The various time series were detrended prior to calculation.

	DT <sub>INV</sub>	DZ <sub>INV</sub>	Z <sub>TOP</sub>	Z <sub>BASE</sub>	Dθ <sub>850</sub>	T <sub>TOP</sub>	T <sub>BASE</sub>	T <sub>850</sub>	T <sub>500</sub>	DθDZ <sub>850-500</sub>	θ <sub>TOP</sub>	θ <sub>BASE</sub>	θ <sub>2M</sub>
DT <sub>INV</sub>	1.00												
DZ <sub>INV</sub>	0.46	1.00											
Z <sub>TOP</sub>	-0.08	0.16	1.00										
Z <sub>BASE</sub>	-0.25	-0.21	0.93	1.00									
Dθ <sub>850,SJV</sub>	0.34	0.27	-0.36	-0.45	1.00								
T <sub>TOP</sub>	0.38	0.19	-0.73	-0.79	0.58	1.00							
T <sub>BASE</sub>	-0.08	-0.02	-0.75	-0.73	0.46	0.89	1.00						
T <sub>850</sub>	0.45	0.29	-0.51	-0.61	0.68	0.91	0.76	1.00					
T <sub>500</sub>	0.18	0.16	-0.23	-0.29	0.38	0.55	0.50	0.60	1.00				
DθDZ <sub>850-500</sub>	-0.38	-0.20	0.41	0.48	-0.48	-0.60	-0.46	-0.66	0.21	1.00			
θ <sub>TOP</sub>	0.43	0.47	0.31	0.14	0.32	0.42	0.24	0.59	0.45	-0.30	1.00		
θ <sub>BASE</sub>	-0.44	-0.31	0.28	0.39	-0.01	0.11	0.34	0.19	0.28	0.03	0.53	1.00	
θ <sub>2M</sub>	0.28	0.12	-0.34	-0.38	-0.07	0.66	0.58	0.68	0.44	-0.42	0.48	0.27	1.00

**Table 4-2.** Correlation of monthly means from 1960–2007 Oakland 00Z radiosonde measurements. The monthly means were calculated using only those days when a subsidence inversion was observed in the radiosonde data. The various time series were detrended prior to calculation.

	DT <sub>INV</sub>	DZ <sub>INV</sub>	Z <sub>TOP</sub>	Z <sub>BASE</sub>	Dθ <sub>850</sub>	T <sub>TOP</sub>	T <sub>BASE</sub>	T <sub>850</sub>	T <sub>500</sub>	DθDZ <sub>850-500</sub>	θ <sub>TOP</sub>	θ <sub>BASE</sub>	θ <sub>2M</sub>
DT <sub>INV</sub>	1.00												
DZ <sub>INV</sub>	0.70	1.00											
Z <sub>TOP</sub>	-0.24	0.03	1.00										
Z <sub>BASE</sub>	-0.46	-0.36	0.94	1.00									
Dθ <sub>850,SJV</sub>	0.47	0.46	-0.35	-0.48	1.00								
T <sub>TOP</sub>	0.52	0.37	-0.75	-0.83	0.53	1.00							
T <sub>BASE</sub>	0.12	0.10	-0.76	-0.74	0.38	0.91	1.00						
T <sub>850</sub>	0.55	0.43	-0.61	-0.71	0.57	0.96	0.85	1.00					
T <sub>500</sub>	0.28	0.33	-0.29	-0.38	0.36	0.65	0.62	0.71	1.00				
DθDZ <sub>850-500</sub>	-0.48	-0.26	0.57	0.61	-0.44	-0.68	-0.56	-0.67	0.04	1.00			
θ <sub>TOP</sub>	0.52	0.53	-0.02	-0.19	0.40	0.67	0.52	0.77	0.66	-0.40	1.00		
θ <sub>BASE</sub>	-0.42	-0.33	0.14	0.25	-0.08	0.23	0.47	0.30	0.40	-0.01	0.51	1.00	
θ <sub>2M</sub>	0.23	0.10	-0.41	-0.42	-0.22	0.67	0.67	0.67	0.52	-0.41	0.56	0.43	1.00

**Table 4-3.** Correlation of daily values from 1960–2007 San Diego 00Z radiosonde measurements. The correlations were calculated using only days when a subsidence inversion was observed in the radiosonde data. The various time series were detrended prior to calculation.

	DT <sub>INV</sub>	DZ <sub>INV</sub>	Z <sub>TOP</sub>	Z <sub>BASE</sub>	Dθ <sub>850</sub>	T <sub>TOP</sub>	T <sub>BASE</sub>	T <sub>850</sub>	T <sub>500</sub>	DθDZ <sub>850-500</sub>	θ <sub>TOP</sub>	θ <sub>BASE</sub>	θ <sub>2M</sub>
DT <sub>INV</sub>	1.00												
DZ <sub>INV</sub>	0.34	1.00											
Z <sub>TOP</sub>	-0.02	0.30	1.00										
Z <sub>BASE</sub>	-0.14	-0.05	0.94	1.00									
Dθ <sub>850,SC</sub>	0.55	0.32	-0.29	-0.42	1.00								
T <sub>TOP</sub>	0.33	0.10	-0.75	-0.82	0.48	1.00							
T <sub>BASE</sub>	-0.06	-0.03	-0.79	-0.81	0.28	0.92	1.00						
T <sub>850</sub>	0.40	0.21	-0.56	-0.66	0.65	0.91	0.80	1.00					
T <sub>500</sub>	0.15	0.13	-0.22	-0.27	0.32	0.43	0.39	0.46	1.00				
DθDZ <sub>850-500</sub>	-0.32	-0.13	0.46	0.53	-0.48	-0.69	-0.60	-0.76	0.22	1.00			
θ <sub>TOP</sub>	0.46	0.57	0.29	0.09	0.31	0.42	0.25	0.55	0.32	-0.37	1.00		
θ <sub>BASE</sub>	-0.33	-0.12	0.16	0.21	-0.18	0.25	0.49	0.30	0.22	-0.17	0.57	1.00	
θ <sub>2M</sub>	0.06	0.01	-0.50	-0.52	0.02	0.80	0.82	0.77	0.34	-0.60	0.47	0.55	1.00

**Table 4-4.** Correlation of monthly means from 1960–2007 San Diego 00Z radiosonde measurements. The monthly means were calculated using only those days when a subsidence inversion was observed in the radiosonde data. The various time series were detrended prior to calculation.

	DT <sub>INV</sub>	DZ <sub>INV</sub>	Z <sub>TOP</sub>	Z <sub>BASE</sub>	Dθ <sub>850</sub>	T <sub>TOP</sub>	T <sub>BASE</sub>	T <sub>850</sub>	T <sub>500</sub>	DθDZ <sub>850-500</sub>	θ <sub>TOP</sub>	θ <sub>BASE</sub>	θ <sub>2M</sub>
DT <sub>INV</sub>	1.00												
DZ <sub>INV</sub>	0.63	1.00											
Z <sub>TOP</sub>	-0.20	0.07	1.00										
Z <sub>BASE</sub>	-0.39	-0.26	0.95	1.00									
Dθ <sub>850,SC</sub>	0.76	0.57	-0.31	-0.48	1.00								
T <sub>TOP</sub>	0.47	0.28	-0.80	-0.86	0.51	1.00							
T <sub>BASE</sub>	0.12	0.05	-0.82	-0.81	0.26	0.93	1.00						
T <sub>850</sub>	0.54	0.35	-0.66	-0.75	0.61	0.96	0.86	1.00					
T <sub>500</sub>	0.25	0.23	-0.38	-0.44	0.44	0.58	0.54	0.62	1.00				
DθDZ <sub>850-500</sub>	-0.49	-0.26	0.56	0.63	-0.44	-0.79	-0.68	-0.80	-0.03	1.00			
θ <sub>TOP</sub>	0.54	0.53	-0.12	-0.29	0.46	0.70	0.56	0.79	0.50	-0.63	1.00		
θ <sub>BASE</sub>	-0.34	-0.26	-0.06	0.03	-0.23	0.38	0.57	0.41	0.31	-0.28	0.55	1.00	
θ <sub>2M</sub>	0.10	0.01	-0.60	-0.58	0.00	0.82	0.89	0.80	0.45	-0.68	0.65	0.70	1.00

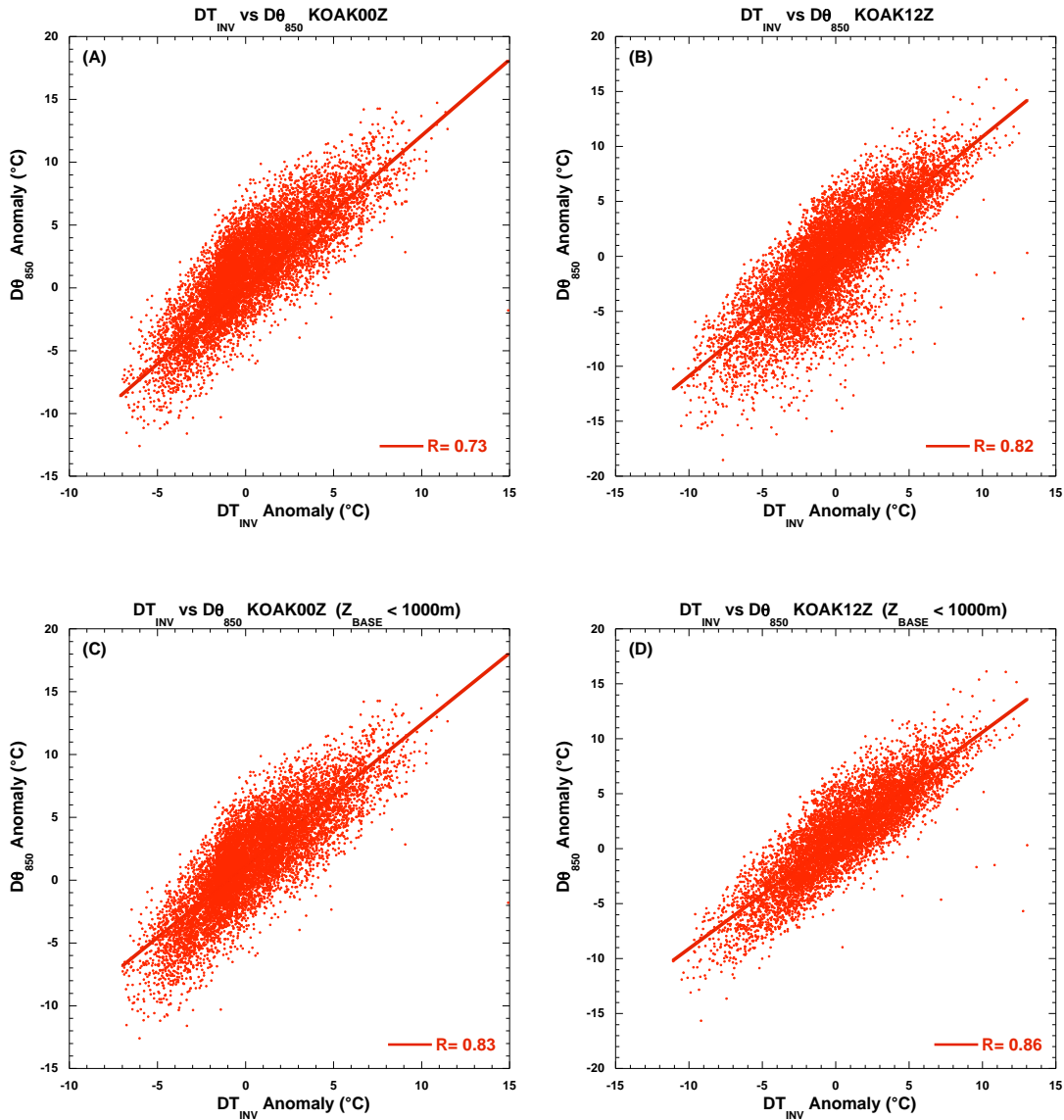


**Figure 4-6.** Scatter plots of daily  $D\theta_{850}$  vs  $DT_{INV}$  anomalies at Oakland at 00Z (left column) and 12Z (right column). For this comparison,  $D\theta_{850}$  was calculated using only radiosonde data. Data was only included for those days when a subsidence inversion was measured. Plots only including days where  $Z_{BASE} < 1000$  meters are shown in (c) and (d). The time period is from 1960–2007. The straight lines represent best linear fits, and the correlation coefficients are shown within each plot.

While certainly not conclusive, these results suggest that  $D\theta_{850}$  is generally a reasonable indication of the actual inversion strength  $DT_{INV}$ . However, it should be noted that the above comparisons were performed at only two sites (KOAK and KSAN), both of which are coastal locations.

#### ***4.5 Relationship Between Inversion Strength and Pollutant Concentrations***

Pollution levels within California's various air basins are determined in part by source emission rates and complex atmospheric chemistry relationships. Physical atmospheric variables such as temperature, humidity, wind, and inversion strength can influence emission rates, chemical reaction rates and dispersal rates. While low-level temperature inversions are only a part of the story, they play a critical role by increasing the vertical stability of the lower atmosphere and thereby inhibiting vertical mixing in the affected air basins. Surface-based inversions are often associated with light winds (weak ventilation), which also allow pollutant concentrations to increase. Figure 4-7 shows the correlation between  $D\theta_{850}$  and pollutant concentrations in the San Joaquin and South Coast Air Basins as a function of month. The monthly correlations are based on daily values of  $D\theta_{850,SJV}$  and  $D\theta_{850,SC}$  and daily average concentrations of ozone and particulate matter (PM10) (daily average at highest station) within each air basin during the period 1983-2007 (data obtained online at [www.arb.ca.gov/aqmis2/aqmis2.php](http://www.arb.ca.gov/aqmis2/aqmis2.php)). The number of pollution reporting stations within each air basin varied in time with approximately 16-22 in the SJVAB and 25-29 in the SOCAB. The solid lines in Figure 4-7 denote correlations found using all available daily values. Air temperature itself plays a significant role in the production of many air pollutants (e.g., ozone). In an effort to reduce the impact of air temperature variations on emissions, the correlations were reproduced using only those days when the daily mean  $T_{2M}$  was within  $\pm 1.0^\circ\text{C}$  of the monthly mean  $T_{2M}$  value (dashed lines in Figure 4-7). Thus in these calculations, the surface temperatures do not vary significantly and the correlations are more indicative of the role of inversion strength (i.e., temperatures aloft).

Positive correlations between  $D\theta_{850}$  and pollutant concentration are observed in nearly all months in each air basin with values as high as 0.7. Correlations between  $D\theta_{850}$  and ozone concentration are largest during the warm months while correlations between  $D\theta_{850}$  and PM10 tend to be greatest during the cool months. In the South Coast Air Basin the  $D\theta_{850}$  vs PM10 correlation values decrease markedly during October and November and may be due to elevated PM10 concentrations from brush fires that occur frequently in Southern California during this period.

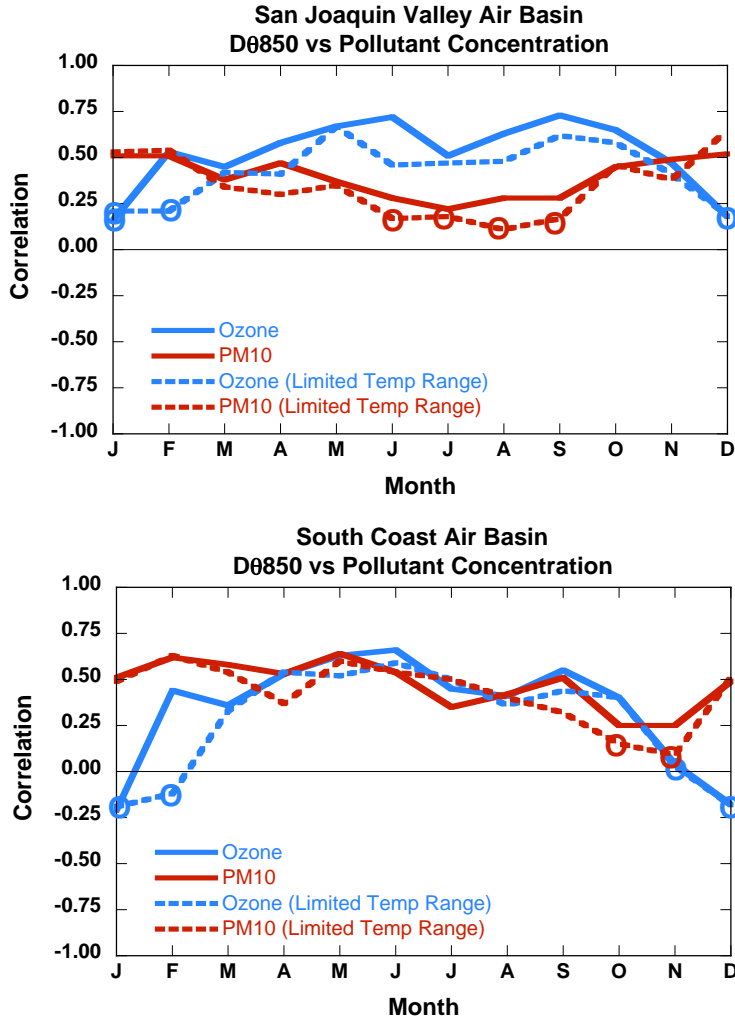


**Figure 4-7.** Correlation of daily values of  $D\theta_{850}$  and pollutant concentration in the San Joaquin (top) and South Coast (bottom) Air Basins as a function of month. Correlations are shown for ozone (blue line) and particulate matter (PM10) (red line). Solid lines are correlations found using all available days while dashed lines only used days with daily  $T_{2M}$  within  $\pm 1.0$  °C of the monthly mean value. Monthly correlations are based on detrended daily values of 12Z  $D\theta_{850}$  and average pollutant concentration within the air basin. Open circles denote correlations not significant at the 95% confidence level.

The correlations produced using only days within the limited temperature range (dashed lines in Figure 4-7) are slightly lower than corresponding correlations using all available days. This result indicates that the significant correlations are not due to temperature alone and suggests that inversion magnitude ( $DT_{INV}$ ) is an important factor determining pollution concentration levels in these air basins.

## 5.0 INFLUENCE OF LARGE-SCALE CIRCULATION AND SEA SURFACE TEMPERATURE

### 5.1 Large-Scale Circulation Patterns Associated with Inversion Strength

Geopotential height and vertical velocity fields from NCEP Reanalysis are used to investigate the relationship between the large-scale atmospheric circulation and the magnitude of inversion strength. Daily fields of 700 hPa geopotential height (H700) and 700 hPa vertical velocity (O700) from NCEP Reanalysis were composited for strong and weak inversions. For the 1979–2005 period, the H700 and O700 fields from the 30 days with the strongest and weakest inversion strengths with respect to the monthly mean were averaged to produce composite plots for the summer and winter seasons. Values of  $D\theta_{850,SJV}$  and  $D\theta_{850,SC}$  were used as the measure of inversion strength. Note that weak positive values of  $D\theta_{850,SJV}$  and  $D\theta_{850,SC}$  could occur when no increase in actual temperature with height (e.g., a recognized temperature inversion) exists. In fact, this is an advantage of using  $D\theta_{850}$  in this application as it provides a continuous measure of inversion conditions spanning from extremely strong to extremely weak cases. The composite plots for San Joaquin Valley and South Coast Air Basins are shown in Figures 5-1 and 5-2, respectively.

From these composites it is clear that quite distinct large-scale atmospheric circulation patterns are associated with strong and weak low-level inversions in California. In general at both locations in both seasons, strong (weak) inversions are associated with an upper-level ridge (trough) at 700 hPa and 500 hPa (not shown). O700 is downward (positive) for strong inversions and upward for weak inversions. Winter season H700 and O700 patterns are generally stronger and of larger horizontal extent than their summer counterparts. Analysis of the anomaly patterns (not shown) shows that during both seasons, the center of the high H700 anomaly pattern is centered slightly to the north of the air basin in question. During winter this area on the southern flank of the height anomaly appears to have some of the largest O700 anomalies.

### 30-Day Composites Based on Strongest and Weakest Inversions SJVAB 12Z $D\theta_{850}$

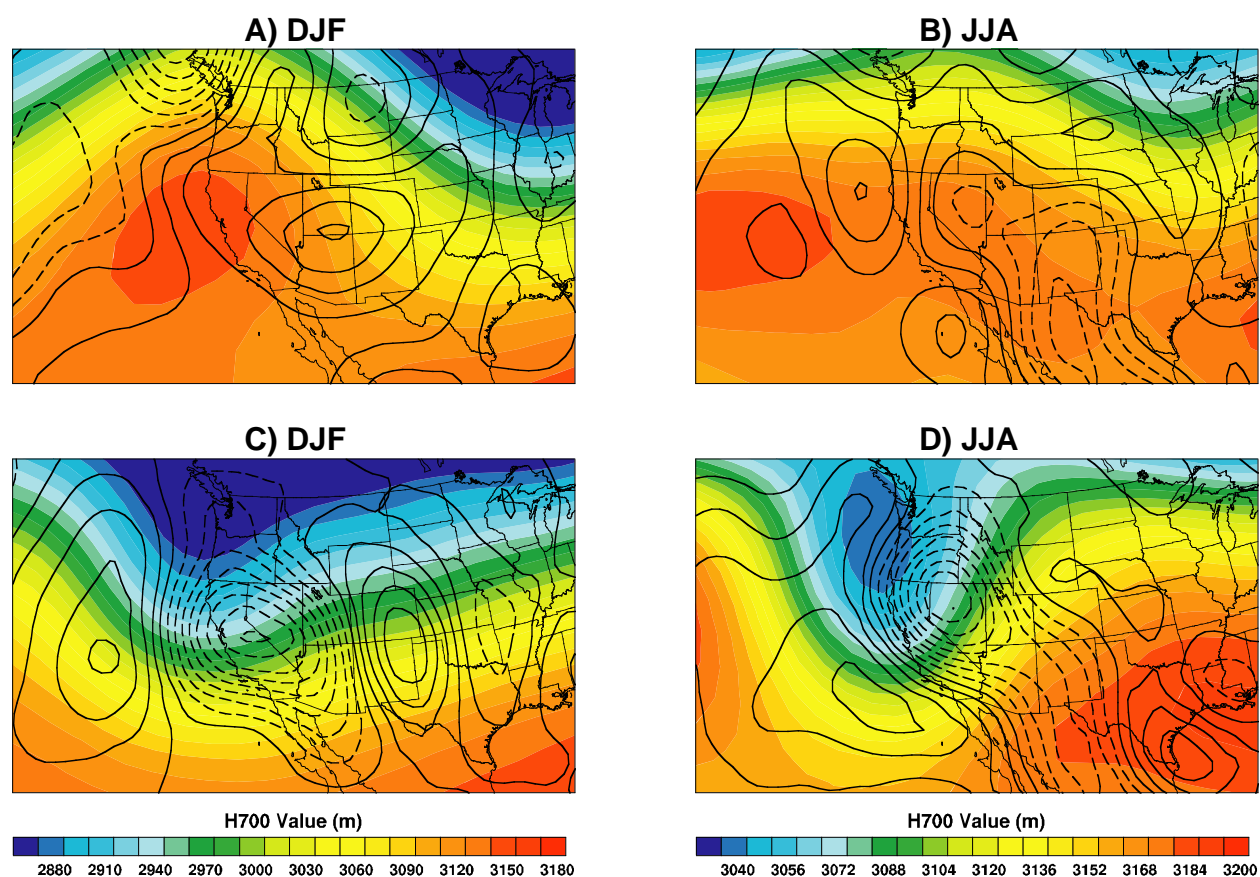


**Figure 5-1.** Mean geopotential height and vertical velocity at 700 hPa from NCEP Reanalysis product during the 30 days with the largest (a, b) and smallest (c, d) inversion magnitudes ( $D\theta_{850,SJV}$  at 12Z) at the San Joaquin Valley Air Basin during the period 1979–2005. The geopotential heights are shown by the color contours and the vertical velocities are denoted by the black contour lines. Contour intervals are 2 pascals per second ( $\text{Pa sec}^{-1}$ ) (JJA [June, July, August]) and 3  $\text{Pa sec}^{-1}$  (DJF [December, January, February]) and dashed contours indicate negative (upward) vertical velocity.

Composite maps of regional 10-meter wind from CaRD10 were made using the same procedure as described above. The 10-meter wind composites for the SJVAB are shown in Figure 5-3. During winter, strong inversions in the SJVAB are associated with quite strong easterly downslope winds over the east side of the valley (foothills of the Sierra Mountains). Within much of the SJVAB there are generally light winds with a slight anticyclonic (clockwise) circulation along the southern perimeter of the valley. The light winds allow increased surface longwave cooling during the night, aiding the daytime inversion strength. The 10-meter winds off the coast of Central California are generally northeasterly, grading to easterly winds along the

coast to the south. Throughout the SJVAB there are large and consistent values of  $D\theta_{850}$ , e.g., strong inversions, that extend north into the San Francisco Bay Area and Sacramento Valley during strong SJVAB winter inversion cases.

### 30-Day Composites Based on Strongest and Weakest Inversions SOCAB 12Z $D\theta_{850}$

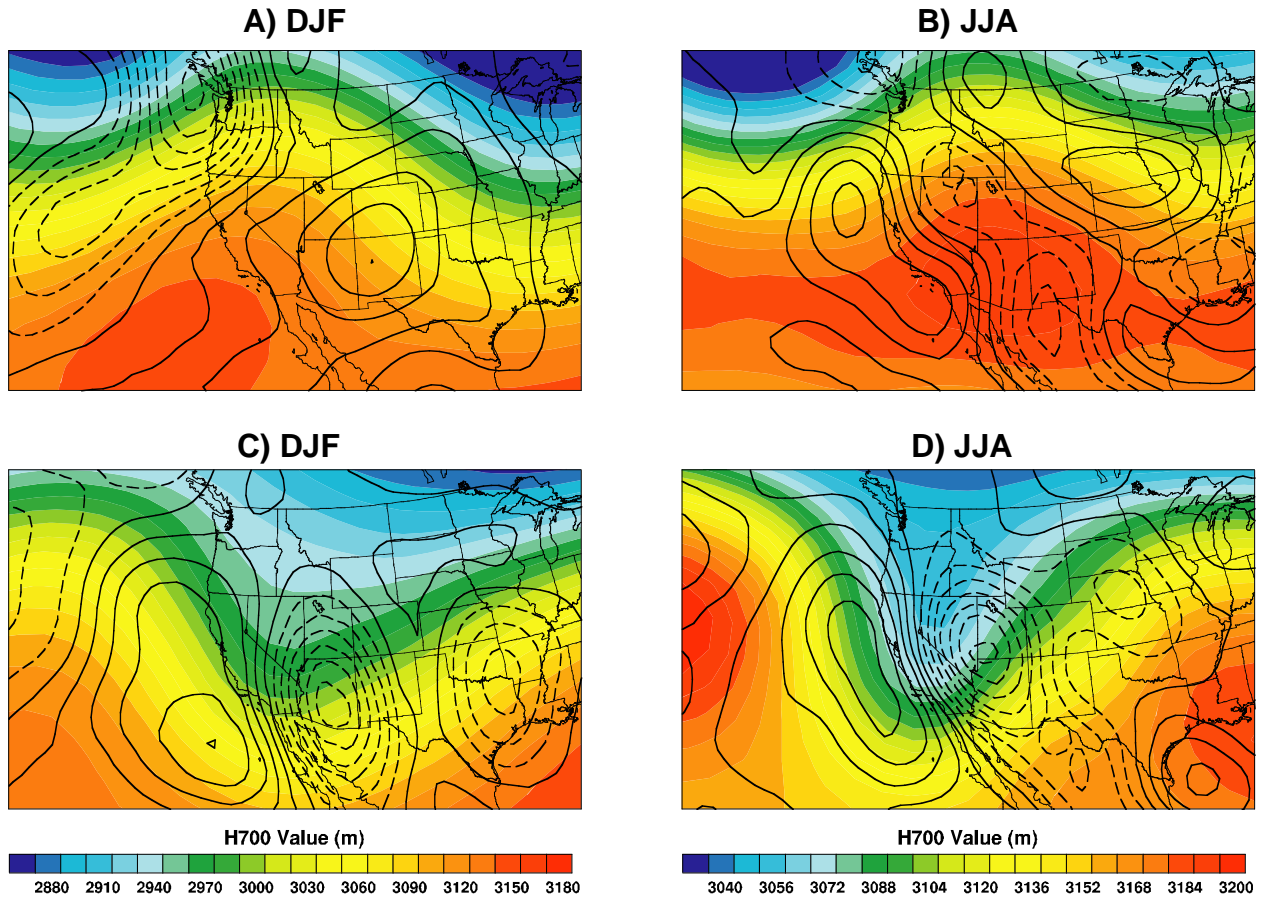


**Figure 5-2.** Mean geopotential height and vertical velocity at 700 hPa from NCEP reanalysis during the 30 days with the largest (a, b) and smallest (c, d) inversion magnitudes ( $D\theta_{850,SC}$  at 12Z) at the South Coast Air Basin during the period 1979–2005. The geopotential heights are shown by the color contours, and the vertical velocities are denoted by the black contour lines. Contour intervals are  $2 \text{ Pa sec}^{-1}$  (JJA) and  $3 \text{ Pa sec}^{-1}$  (DJF) and dashed contours indicate negative (upward) vertical velocity.

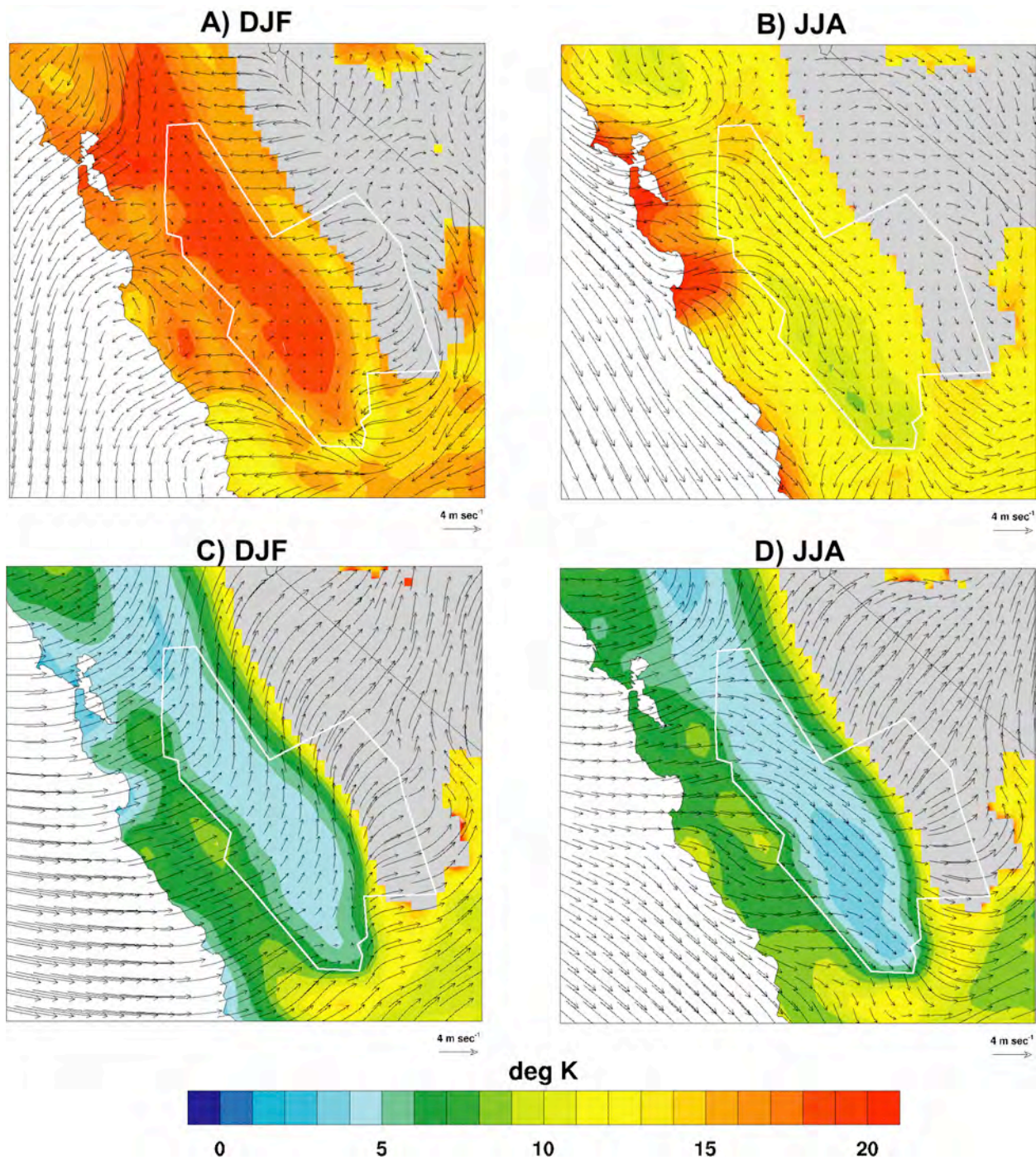


**Figure 5-3.** Average values of CaRD10  $D\theta_{850}$  and 10-meter wind during the 30 days with the largest (a, b) and smallest (c, d) observed  $D\theta_{850,SJV}$  during time period 1979–2005 for DJF (left column) and JJA (right column). The white line denotes the approximate boundary of the San Joaquin Valley Air Basin. The color filled contours indicate the CaRD10  $D\theta_{850}$  values; the vector arrows represent the 10-meter winds. Grey areas indicate where surface is above the 850 hPa level and  $D\theta_{850}$  is not defined.

Strong summer SJVAB inversions are associated with moderate northwesterly 10-meter winds throughout most of the SJVAB, with reduced velocities at the southern end. Winds over the coastal waters of Central California are northwesterly in contrast to the more northerly or northeasterly winds during winter. Inspection of the anomalous wind fields (not shown) indicates that the anomalous winds in the SJVAB and the winds offshore along the California coast are from the southeast, opposing the normal northwesterly wind flow. Lower 10-meter winds in the SJVAB during strong summer inversions would promote more accumulation of pollutants than during conditions associated with normal inversions, further increasing the likelihood of poor air quality. Additionally, the convergence in the southern part of the SJVAB could facilitate the accumulation of pollution in this area. Values of  $D\theta_{850}$  are moderately high and relatively consistent throughout much of Central California, although they are weaker in magnitude than during wintertime. Probably this is because strong summer inversions usually occur when there are extremely warm surface temperatures, while strong inversions during winter often contain relatively cool surface temperatures.

In sharp contrast to the strong inversion composite, weak SJVAB inversions during winter are associated with southwesterly 10-meter winds throughout much of Central California. These events are most likely related to passing synoptic storm systems with the slight change in direction in the SJVAB due to interaction of the wind field with the topography of the Coast Ranges and Sierras. During weak winter inversions in the SJVAB,  $D\theta_{850}$  values are much lower throughout the SJVAB, extending consistently into the Sacramento Valley and into the San Francisco Bay Area. During summer, weak SJVAB inversions are associated with strong westerly component in the winds off the coast and have a similar pattern of low  $D\theta_{850}$  values throughout the Central Valley and into the San Francisco Bay Area. These summer weak inversion cases may also be related to passing synoptic systems.

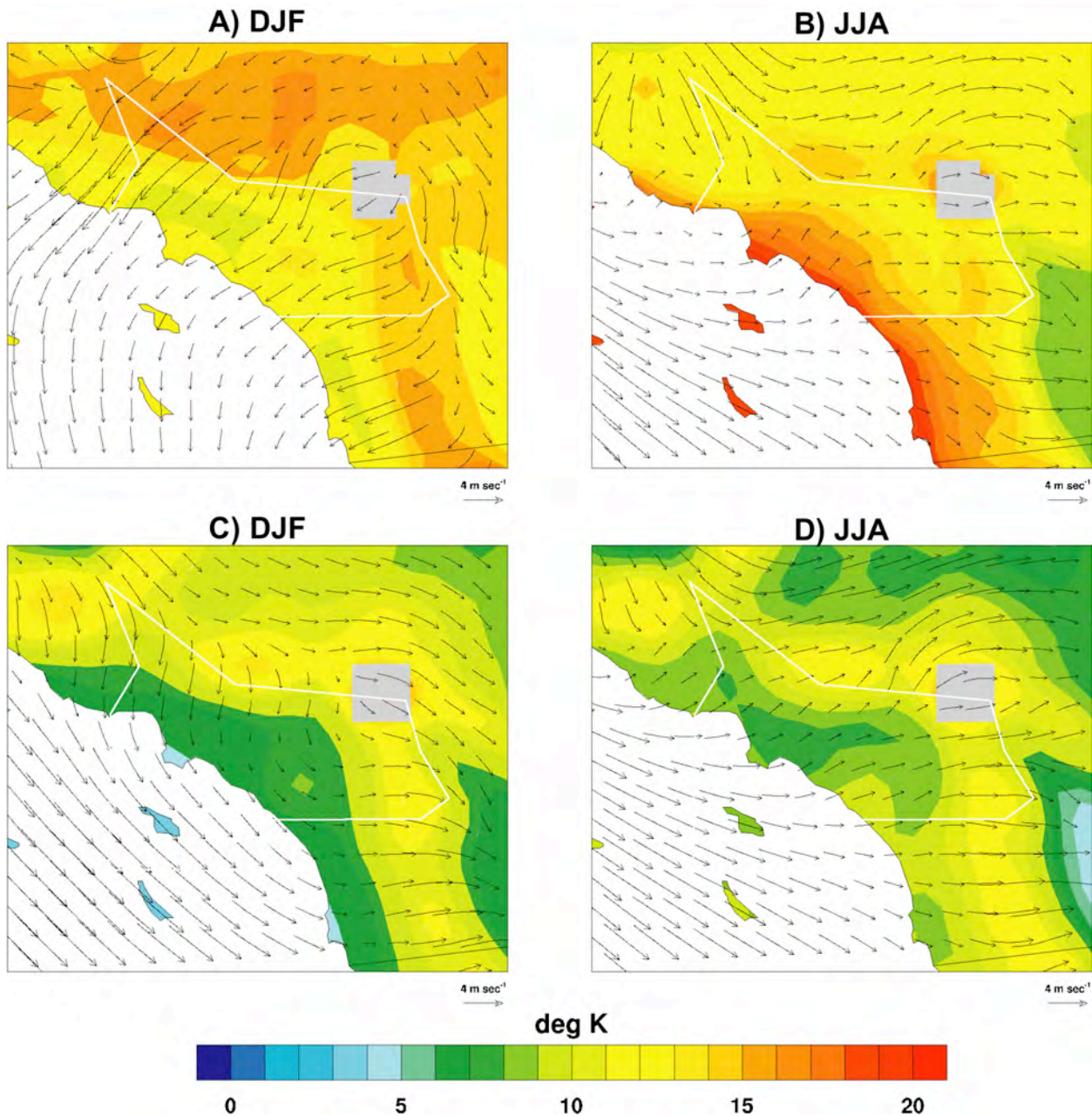


**Figure 5-4.** Average values of CaRD10  $D\theta_{850}$  and 10-meter wind during the 30 days with the largest (a, b) and smallest (c, d) observed  $D\theta_{850,SC}$  during time period 1979–2005 for DJF (left column) and JJA (right column). The white line denotes the approximate boundary of the South Coast Air Basin. The color filled contours indicate the CaRD10  $D\theta_{850}$  values while the vector arrows represent the 10-meter winds. Grey areas indicate where surface is above the 850 hPa level and  $D\theta_{850}$  is not defined.

Figure 5-4 shows the 10-meter wind composites for the South Coast Air Basin. During strong inversions in winter, strong northeasterly 10-meter winds are seen throughout the SOCAB and

have the appearance of a Santa Ana wind event. Contrastingly, weak inversion events in winter are associated with moderate north-to-northwesterly winds over most of the SOCAB. Winds over the adjacent coastal waters are also northwesterly and are larger in magnitude. As in the case for the SJVAB, wintertime weak inversion events are likely related to passing synoptic systems (as suggested by the 700 hPa composite) and are the major control of inversion strength during the winter.

During summer, there is less difference in wind direction between strong and weak inversion events over the SOCAB. In both cases, winds over coastal waters are northwesterly and onshore. Examination of wind anomalies (not shown), indicates that weak inversion events have stronger winds with a more westerly component than strong inversion events. Relatively weak values of  $D\theta_{850}$  are seen along the coastal areas, which is in strong contrast to the strong inversion case. Since the overall surface circulation pattern is similar in summer for both strong and weak inversions due to the dominance of the summertime North Pacific High, the larger-scale flow at 850 hPa looks to be the primary driver of inversion strength variability. As seen in Figure 5-2, there are generally low (high) 700 hPa heights over much of Southern California during weak (strong) inversions, which would tend to lead to cooler (warmer) than normal 850 hPa temperatures and reduced (increased) values of  $D\theta_{850}$ .

### ***5.1.1 Physical Mechanisms and Inversion Characteristics***

At the most fundamental level, temperature inversions will be strengthened if heating of the atmosphere above the inversion is greater than heating of the boundary layer and surface below it, or if cooling of the atmosphere above the inversion is less than cooling below. Inversions are weakened if the opposite relative differences in heating/cooling occur. Several mechanisms contribute to heating/cooling, including radiative flux divergence, surface fluxes, and advection. Recall that the strength of the inversion is defined as a difference of temperature between the top and the bottom of the inversion layer.

Radiatively driven surface fluxes are clearly responsible for the diurnal cycle in inversion strength over land but also play a role at longer time scales. Greater surface radiative cooling at night will strengthen the surface inversion and may result in a stronger subsidence inversion

layer the following day. Greater surface radiative heating during the day will contribute to the weakening of the inversion by increasing the temperature of the boundary layer, but this may be opposed by entrainment growth of the boundary layer that leads to a higher, but stronger inversion. An imbalance between nighttime radiative cooling and daytime radiative heating may lead to a diurnal mean change in inversion strength.

The ocean greatly minimizes radiatively driven variations in surface and boundary layer temperature and thus acts as an anchor for the potential temperature of the inversion base. Since the ocean off the coast of California is cold, there is a strong decrease in inversion strength going inland, especially on days of strong inversions (summertime Figures 5-3 and 5-4). All else being the same, advection of the marine layer inland will bring cooler boundary layer air to a location and thus strengthen the inversion there. Because hot inland surface temperatures promote the sea breeze, the cooling effect of the marine layer may act as a negative feedback and resist weakening of the inversion. The fact that onshore winds are relatively weaker when the temperature inversion is stronger (summertime Figures 5-3 and 5-4) indicates that the sea breeze does not make a substantial contribution to variability in regional inversion strength on synoptic time scales.

Another mechanism for driving temperature changes is horizontal and vertical temperature advection and adiabatic warming associated with large-scale circulation patterns. The geopotential height patterns associated with strong and weak inversions noted in the preceding section indicate the importance of large-scale circulation on inversions in California. However, these large-scale patterns do not specifically identify the actual physical mechanisms that strengthen or weaken inversions. In this section, NCEP Reanalysis products are further analyzed to help answer this question. We also examine the relative roles of mid-tropospheric and surface processes in driving temperature inversions at synoptic time scales.

Correlations between anomalies of  $D\theta_{850}$ ,  $\theta_{850}$ , and  $\theta_{2m}$  for San Joaquin Valley and South Coast Air Basins were calculated to see whether an increase in free-tropospheric temperature or a decrease in surface temperature contributed most to inversion strength. On daily to monthly time scales in all cases, the magnitudes of positive correlations between  $\theta_{850}$  and  $D\theta_{850}$  were

substantially larger than the magnitudes of negative correlations between  $\theta_{2m}$  and  $D\theta_{850}$ . In fact,  $\theta_{2m}$  was often positively correlated with  $\theta_{850}$  and  $D\theta_{850}$  and frequently exhibited the highest correlation when surface temperature lagged 850 hPa temperature by a day. These results indicate that mid-tropospheric processes are primarily responsible for driving variability in temperature inversions on sub-seasonal time scales. The presence of anomalously cold surface temperature may aid the early development of a strong temperature inversion, but as the inversion continues to evolve, surface temperature warms in response to warming in the free troposphere and thus acts to mute the strength of the temperature inversion.

An examination of temperature variance at standard pressure levels in the San Diego and Oakland soundings indicated that the 850 hPa level experienced larger changes in daily temperature than any other pressure level. Additionally, the 850 hPa level is the standard pressure that is most commonly located immediately above the inversion top and would be most indicative of how the free atmosphere impacts the inversion layer. Thus, the mechanism(s) driving variations in 850 hPa temperature must also be primarily responsible for producing strong temperature inversion events. Since radiative and turbulent processes act on somewhat long time scales (relative to a few days) in the free troposphere, we assume that advection is one of the principal drivers of 850 hPa temperature on synoptic time scales.

To test this hypothesis, finite differences were applied to the NCEP reanalysis to calculate horizontal potential temperature advection, vertical potential temperature advection, and the local rate of potential temperature change at 850 hPa and 1000 hPa for grid points near San Diego and Oakland. Total (horizontal + vertical) advection of potential temperature is correlated with the local rate of potential temperature change at values of 0.54–0.67 for both the cool and warm seasons and at both San Diego and Oakland (positive advection value indicates warming). These correlations are likely biased low due to errors resulting from the crudeness of finite difference calculations on standard pressure levels and by the lack of energy conservation in the NCEP reanalysis. Furthermore, horizontal and vertical advection are substantially anti-correlated at both locations, which would mean that the total is to some extent a difference between large quantities and thus more susceptible to the errors noted above. Correlations between horizontal and vertical advection were -0.65 and -0.75 during the cool season and -0.40 and -0.48 during the

warm season, with the correlations at Oakland larger than at San Diego. The larger anti-correlation at Oakland during both seasons is probably due to the closer proximity to the storm track resulting in more frequent and stronger influences from synoptic storm systems. At both San Diego and Oakland, variability in vertical advection dominates horizontal advection in contributing to variability in total advection during winter but contributes equally with horizontal advection to variability in total advection during summer.

The compensation between horizontal and vertical advection is a key issue for understanding 850 hPa temperature change. Subsidence causes warming at 850 hPa because air with higher potential temperature has moved down to replace air with lower potential temperature. Quasi-geostrophic dynamics, however, causes this downward motion to be associated with horizontal cold advection, which cancels much or all of the vertical warm advection. In particular, a local maximum in subsidence is typically not associated with the greatest local warming, as seen in Figures 5-1 and 5-2, because horizontal cold advection is also large there. Neither does the greatest local warming occur under the peak elevation of an upper-level ridge, since subsidence is typically weak there (Figures 5-1 and 5-2). The favorable conditions are instead the particular combination of vertical warm advection that is relatively strong and horizontal cold advection that is relatively weak. For example, subsidence is strong in the cold sector following the passage of a surface front and upper-level trough, but horizontal cold advection overwhelms vertical warm advection, so such conditions do not contribute in the composite plots. The strongest wintertime inversions are instead associated with northeasterly Santa Ana-like flow (Figures 5-3 and 5-4).

Key variables from the NCEP Reanalysis product were composited for the 30 days with the strongest inversions. Two composites were made again using values of  $D\theta_{850,SJV}$  and  $D\theta_{850,SC}$  as the measure of inversion strength. Each composite was calculated at the closest Reanalysis grid point to the appropriate site. Additionally, the composites extend 10 days prior to and 10 days after the day with maximum  $D\theta_{850}$ , allowing the investigation of the temporal evolution and interaction of various physical processes.

At both locations during both seasons, vertical warm air advection transitions from being smaller to being larger than horizontal cold air advection at 850 hPa several days prior to maximum  $D\theta_{850}$ . Potential temperature at 850 hPa thus begins increasing and hence  $D\theta_{850}$  becomes stronger. Immediately following the maximum  $D\theta_{850}$ , subsidence and vertical advection weaken and become smaller than horizontal cold advection. This causes  $D\theta_{850}$  to decrease, along with a contribution from increasing  $\theta_{2m}$ . During winter, the pattern of advection at 1000 hPa is generally similar to the pattern at 850 hPa, but during summer strong inversion cases total advection at 1000 hPa always acts to cool, due to the weakness of vertical motion near the surface and the strength of prevailing horizontal cold advection. The observed warming of summertime  $\theta_{2m}$  is likely instead driven by radiative heating, which can be strong near the surface.

For strong inversion cases in winter and summer in the South Coast Air Basin and in winter in the San Joaquin Valley Air Basin, the increase in warm total advection several days prior to maximum  $D\theta_{850}$  is driven by a strengthening of subsidence, but for the summertime SJVAB, it is instead caused by a weakening of horizontal cold advection. Weaker than average horizontal cold advection, however, is a precondition necessary for the development of strong inversion events during summer in both the SOCAB and SJVAB, as is suggested by Figures 5-3 and 5-4.

### ***5.2 Impact of Local Sea Surface Temperature on Inversion Measures***

The proximity of California to relatively cool Pacific sea surface temperatures (SSTs) may play an important role in the strength and variability of inversions in coastal regions. Strong inland surface heating can act to weaken the local inversion strength by increasing the temperature at the inversion base. The strong surface heating often initiates a sea breeze circulation that provides a relatively cool horizontal (onshore) flow near the coast that will tend to cool the inversion base and thereby increase the inversion strength and cancel out at least part of the weakening due to the surface heating. One would expect the impact of the sea breeze on inversion strength to increase as the ocean-land temperature contrast increases, unless particular synoptic conditions act to prevent this, as suggested in Figures 5-3 and 5-4.

**Table 5-1.** Correlations between monthly mean values of local SST and various inversion measures at Oakland and San Diego. Correlations greater than 0.19 at San Diego and 0.22 at Oakland are significant at the 95% confidence level.

Inversion Measure	San Diego	Oakland
$DT_{INV}$	-0.37	-0.33
$DZ_{INV}$	-0.33	-0.30
$D\theta_{850,SJV}$	—	-0.05
$D\theta_{850,SC}$	-0.31	—
$\theta_{2M,SJV}$	—	0.06
$\theta_{2M,SC}$	0.34	—

Table 5-1 contains correlations between monthly mean values of local SST and inversion measures  $DT_{INV}$ ,  $DZ_{INV}$ ,  $D\theta_{850}$ , and  $\theta_{2M}$ . Local SST is calculated as an average over several  $1^\circ \times 1^\circ$  grid cells immediately off the coast and was obtained from the Reynolds OI.v2 SST analysis extending from November 1981 to present (Reynolds et al. 2002). The correlations were based on a total of 314 months of data. The SST time series has non-negligible autocorrelation on monthly time scales that reduces the effective number of degrees of freedom. The decorrelation time of each SST time series was calculated based on the e-folding time of the autocorrelation function. After taking the SST decorrelation time into account, correlations greater than 0.19 at San Diego and 0.22 at Oakland are significant at the 95% confidence level.

Significant anti-correlations exist between SST and inversion strength (as measured by either  $DT_{INV}$  or  $D\theta_{850}$ ), indicating that cooler SSTs are associated with stronger and thicker inversions. The low correlation of  $D\theta_{850,SJV}$  is due to a reduced influence of local SST on the near surface temperatures in the San Joaquin Valley compared to the South Coast Air Basin. Relative to the South Coast Air Basin, the San Joaquin Valley is physically further away from the ocean. Additionally, most of the western edge of the San Joaquin Valley is bounded by the Coast Ranges acting as a significant topographic boundary inhibiting surface level flow between the Pacific Ocean and the Valley.

Multiple linear regression analysis was used to help isolate the impact of the local SST from any possible effects of either the El Niño/Southern Oscillation (ENSO) or the Pacific Decadal Oscillation (PDO). An initial linear regression was performed using the Southern Oscillation

Index (SOI) and PDO indices as predictors (independent variables) and  $DT_{INV}$  as the predictand (dependent variable). It was found that a maximum amount of variance was explained the regression using lead times of two months for SOI and 1 month for PDO. An additional regression, now using local SST in addition to the SOI and PDO indices, explained 50% more variance than did the initial regression, indicating that the local SST adds a significant amount of information to this relation. SST probably contributes more to inversion variability on monthly and longer time scales as atmospheric synoptic variations tend to average out.

## **6.0 INVERSION PERSISTENCE**

### ***6.1 Persistence of Strong and Weak Inversions***

To understand how strong or weak inversions align in strings of days, daily inversion strength was sorted into quartiles and used to examine the persistence of inversions. In this case, inversions were measured by the inversion strength  $DT_{INV}$ . Inversion persistence was investigated for the warm season (June-September) and for the cold season (Dec-March) using the persistence value (PV) described in Section 3. A value of  $PV_k$ , where k is the designated quartile, was calculated for each day in the 1960–2007 record. Average values of  $PV_k$  were obtained for both the warm and cold seasons (weakest inversions are in quartile 1 and strongest inversions are in quartile 4).

Average values of PV for each quartile, shown in Table 6-1, range from 0.34 to 0.78 for the warm season and from 0.35 to 0.70 for the cool season and are for the most part substantially greater than values generated using a Monte Carlo procedure,. Results are shown for both the Oakland and San Diego sites and for both the warm and cold seasons. Inversions within quartiles 1 and 4 tend to persist longer than inversions in quartiles 2 and 3. For example, during the warm season quartile 1 and quartile 4 inversions have average PV values exceeding 0.6, while quartile 2 and quartile 3 inversions have average PV values less than 0.4. In other words, extreme inversions (both weak and strong) tend to persist more than moderate inversions. This is a general result that is applicable to both warm and cold seasons, both sites, and both the 00Z and the 12Z radiosonde launch times.

**Table 6-1.** Average value of persistence parameter PV.

Designated Quartile	San Diego 12Z	San Diego 00Z	Oakland 12Z	Oakland 00Z
Warm Season				
1	0.63	0.52	0.70	0.59
2	0.41	0.39	0.41	0.34
3	0.41	0.38	0.44	0.42
4	0.67	0.64	0.78	0.64
Cold Season				
1	0.54	0.42	0.47	0.43
2	0.38	0.38	0.36	0.39
3	0.38	0.35	0.37	0.35
4	0.70	0.49	0.67	0.51

To present inversion persistence in a slightly different manner, consider how many of all of the strong inversion cases occurred in strings of two days or more. The distribution at 00Z shows that 80% and 77% of the strong summer inversions and 66% and 62% of the strong winter inversions, at Oakland and San Diego respectively, are clustered into events lasting two days or longer.

Inversion persistence tends to be stronger during the warm season than the cool season. This seasonality may be related to the more frequent synoptic events during the cold season, which reduce 850 hPa temperature through upward motion and cold vertical temperature advection. Stronger surface wind speeds during synoptic events may also increase the turbulence in the boundary layer and tend to weaken or eliminate nighttime surface temperature inversions. Inversions occurring in the early morning (12Z) also tend to be slightly more persistent than those measured in the mid-afternoon (00Z). This may be due to the multi-day tendencies of strong or weak radiation inversions that occur primarily in the early morning hours and are nearly absent in the mid-afternoon. The radiosonde sites at Oakland and San Diego have roughly the same level of inversion persistence. While Oakland is more poleward and subject to more frequent synoptic events, both locations are dominated by the North Pacific High and by marine influences that could explain some of the similar characteristics.

## 6.2 Analysis of Persistent Inversion Episodes

For this study a persistent inversion episode is defined as a string of continuous days with a strong inversion present, namely a value of  $DT_{INV}$  (00Z) within quartile 4 (quartile values determined using all values of  $DT_{INV}$  (1960-2007) at a particular site). A catalog of persistent inversion episodes lasting 2 days or longer was created and the distribution of episodes based on duration and season is shown in Figure 6-1 for each site. The number of episodes decreases markedly as duration increases and the shape of the distribution is similar for both locations. Seasonal variations are not large, however there are fewer long duration ( $> 4$  days) episodes during DJF and slightly more during JJA. Also, during MAM the relative number of short duration (2-day) episodes at Oakland is greater than at San Diego where there is a higher number of long duration (greater than 2 days in length) episodes.

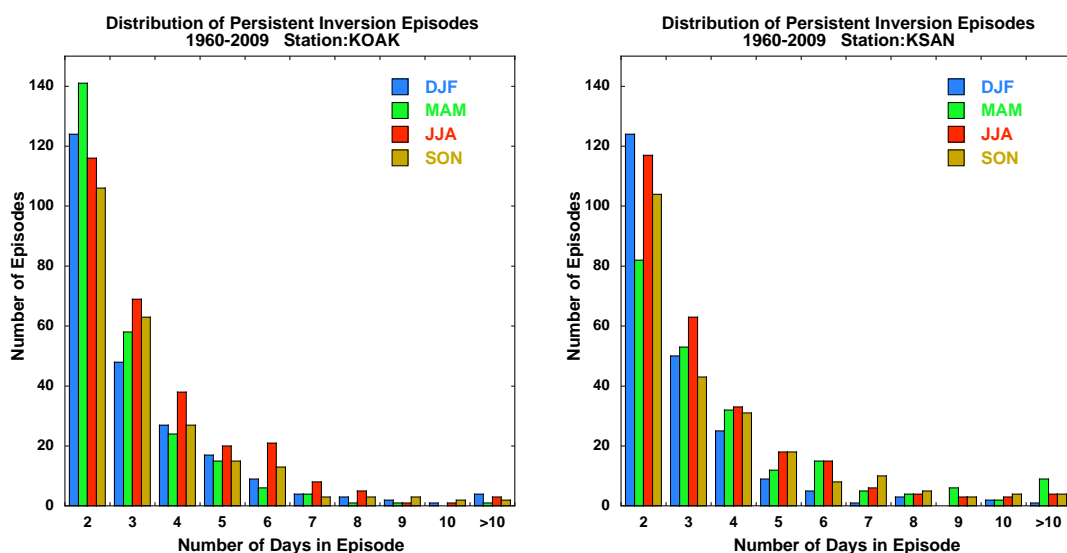


**Figure 6-1.** Distribution of persistent strong inversion episodes by season at Oakland (left) and San Diego (right) based on the episode length.

To investigate how persistent inversion episodes may be linked to large-scale atmospheric circulation patterns, composite plots of 700 hPa geopotential height anomalies (H700) were produced for episodes of 5-days or longer. Daily mean values of H700 were obtained from NCEP Reanalysis (Kalnay et al, 1996) for the 1960-2007 period and anomalies were constructed by removing daily long-term means. Two multi-day composites were produced for each site, the first was centered on the first day of the inversion episodes and the second was centered on the

ending day of the episodes. This allows examination of circulation patterns that may be responsible for the onset and dissipation of persistent episodes.

Composite H700 anomaly plots for JJA are shown in Figure 6-2. There were a total of 59 and 53 events of 5 days or longer during JJA at Oakland and San Diego, respectively. There were only 14 episodes with overlapping days (total days = 70 out of 362 possible) at both Oakland and San Diego. The left hand side column of the figure contains H700 values relative to the episode starting day (day 0) with composites ranging from 3 days prior to the start day (day -3) and out to 2 days after the start day (day 2). Composites based on the episode ending day are in the right column ranging from 2 days prior the end day (day -2) and out to 3 days after the end day (day 3). The stippling represents values that are significant at the 95% confidence level.

At Oakland (Figure 6-2a), there is a significant increase in the positive H700 anomalies value over the Pacific coast during the 3 days leading up to the start of persistent inversion episodes with peak values centered slightly offshore of Washington state. The positive height anomalies are part of an amplified wave train, in which there are alternating positive over western North Pacific, negative over Central-Eastern North Pacific, positive over U.S. West Coast, and negative over eastern U.S. There are significant negative H700 anomalies over the central north Pacific and the eastern U.S at the onset of these episodes. As the inversion episodes end, the positive H700 height anomalies centered along the U.S. west coast decrease in magnitude and retrograde from east to west. Within 2 days of the end of the episode the positive H700 anomalies are replaced by negative anomalies, however these negative anomalies are not significant at the 95% confidence level.

The JJA H700 anomaly patterns for persistent inversion episodes at San Diego (Figure 6-2b) follow a similar pattern albeit with some differences. Again the height anomaly patterns form a wave train, but the positive western Pacific anomaly center is not as prominent as for Oakland case. The H700 anomalies associated with the San Diego episodes are not as large and the center of the positive H700 anomaly over the Pacific coast is centered further south as compared to the H700 anomalies associated with the Oakland episodes.

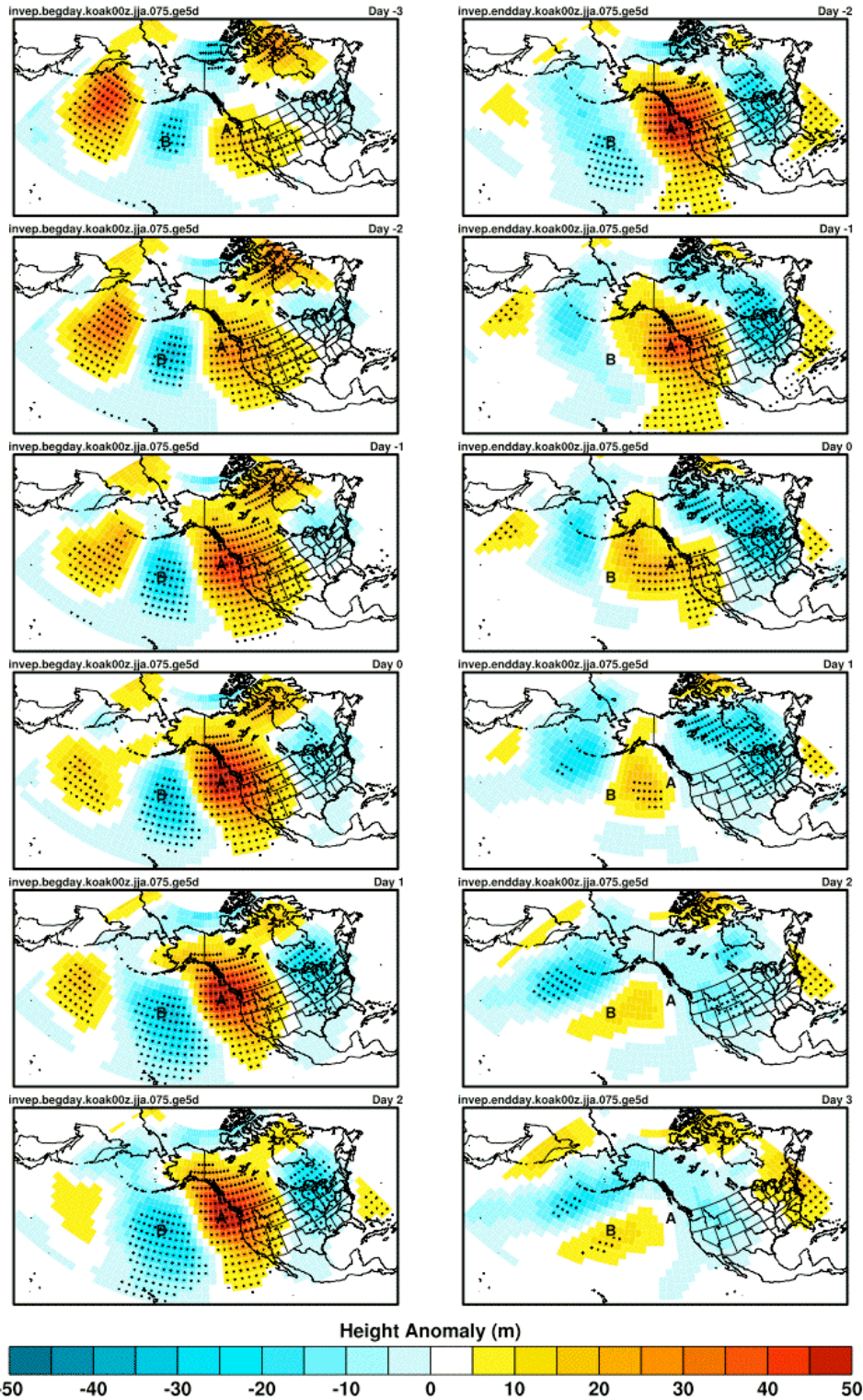


**Figure 6-2a.** Composite H700 anomaly plots for JJA based on the starting day (left column) and ending day (right column) of persistent strong inversion episodes lasting 5 days or longer at Oakland. Plots are shown for 3 days prior and 2 days after the start day and 2 days prior and 3 days after the ending day.

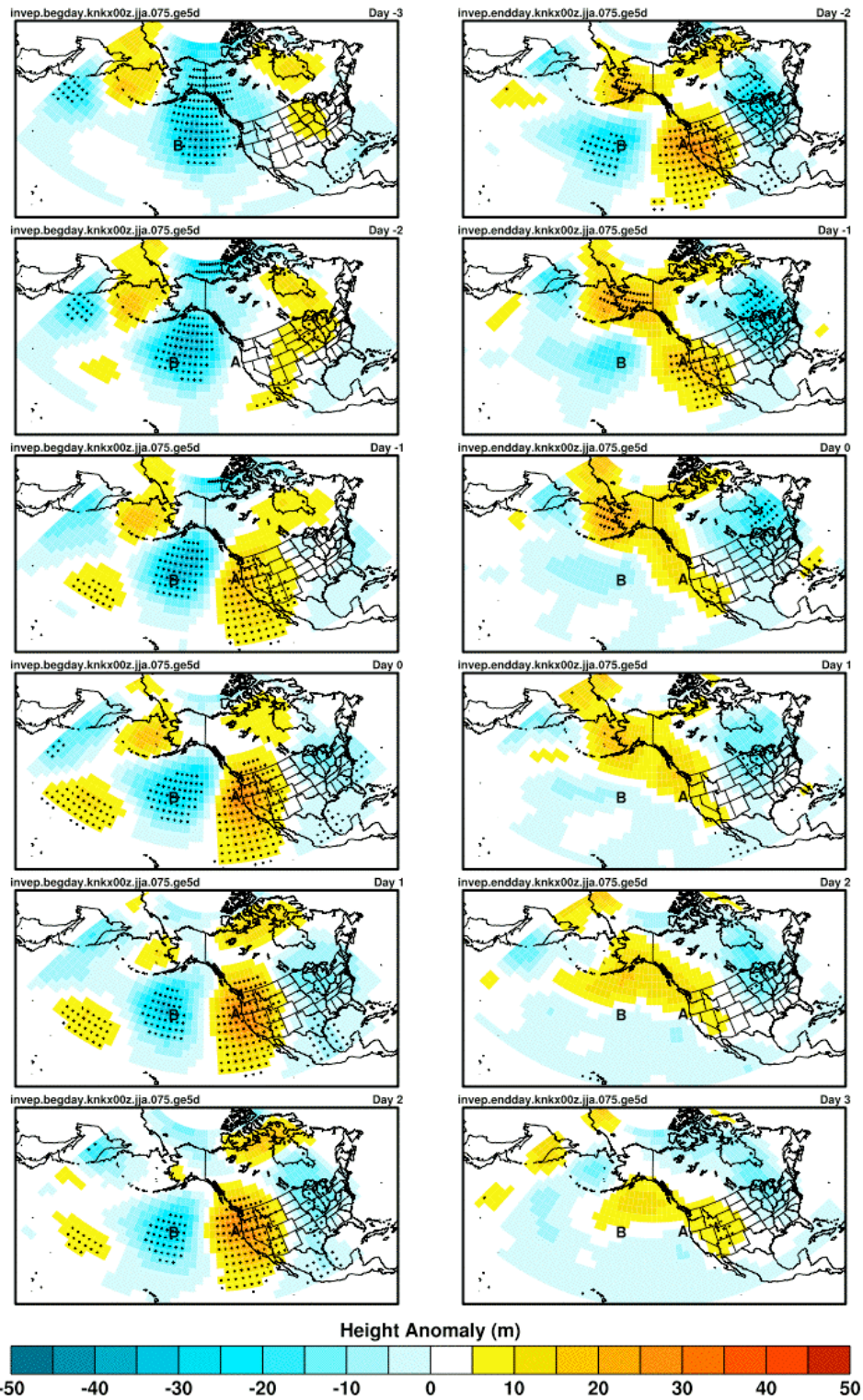
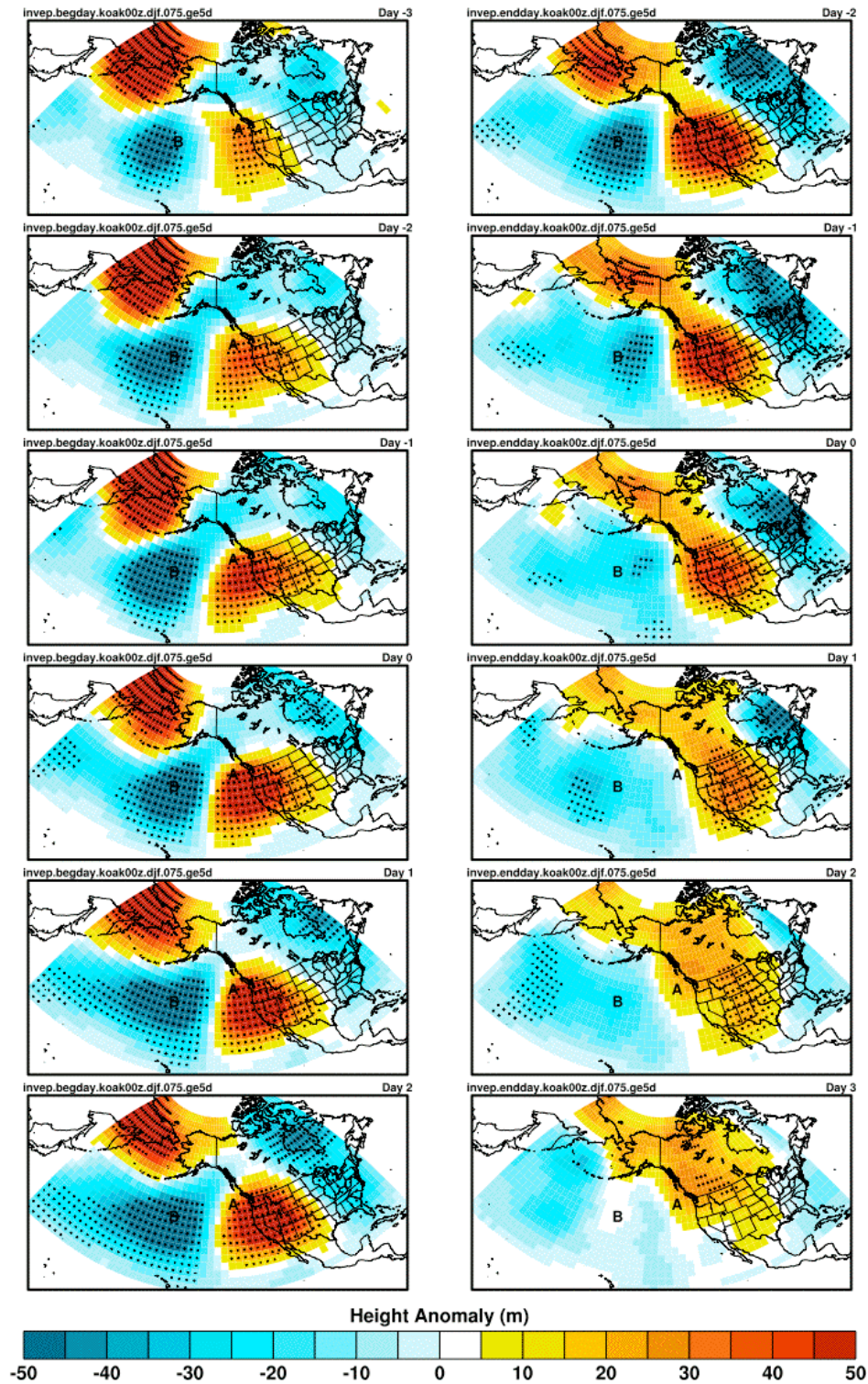


Figure 6-2b. Same as Figure 6-2a, except for San Diego.

The magnitude and horizontal extent of these H700 anomalies suggests that persistent inversion episodes of 5 days or longer are often initiated by the development of a large anomalously high pressure system located over the Pacific coast that develops in place as opposed to being advected into the region. The persistence of these inversion episodes may be associated with a blocking pattern in the large-scale atmospheric circulation that maintains the large positive H700 anomalies in place. Once the blocking mechanism weakens the region of positive H700 heights moves away from the area and the inversion episode comes to an end. The positive anomalies appear to progress from west to east which is a notable difference from the composite anomalies for Oakland.

Composite H700 anomaly plots for DJF are shown in Figure 6-3. There were a total of 40 and 21 events of 5 days or longer during DJF at Oakland and San Diego, respectively, with only 8 episodes that had overlapping days (total days = 35 out of 137 possible) at both sites. Like JJA, a wave train occurs, but more spread out with negative anomalies over central-western North Pacific and positive anomalies over Eastern Asia and western North Pacific. Positive anomaly over west coast actually extends from eastern North Pacific to Rocky Mountains. The magnitudes of the anomalies are also larger than those found in JJA. At the end of the persistent episodes, the positive H700 anomalies weaken and move toward the east. This is in contrast to the movement of these anomalies during JJA which was from east to west, indicating the winter progressive movement is most likely due to the stronger westerly flow and synoptic forcing over California during the DJF season.



**Figure 6-3a.** Composite H700 anomaly plots for DJF based on the starting day (left column) and ending day (right column) of persistent strong inversion episodes lasting 5 days or longer at Oakland. Plots are shown for 3 days prior and 2 days after the start day and 2 days prior and 3 days after the ending day.

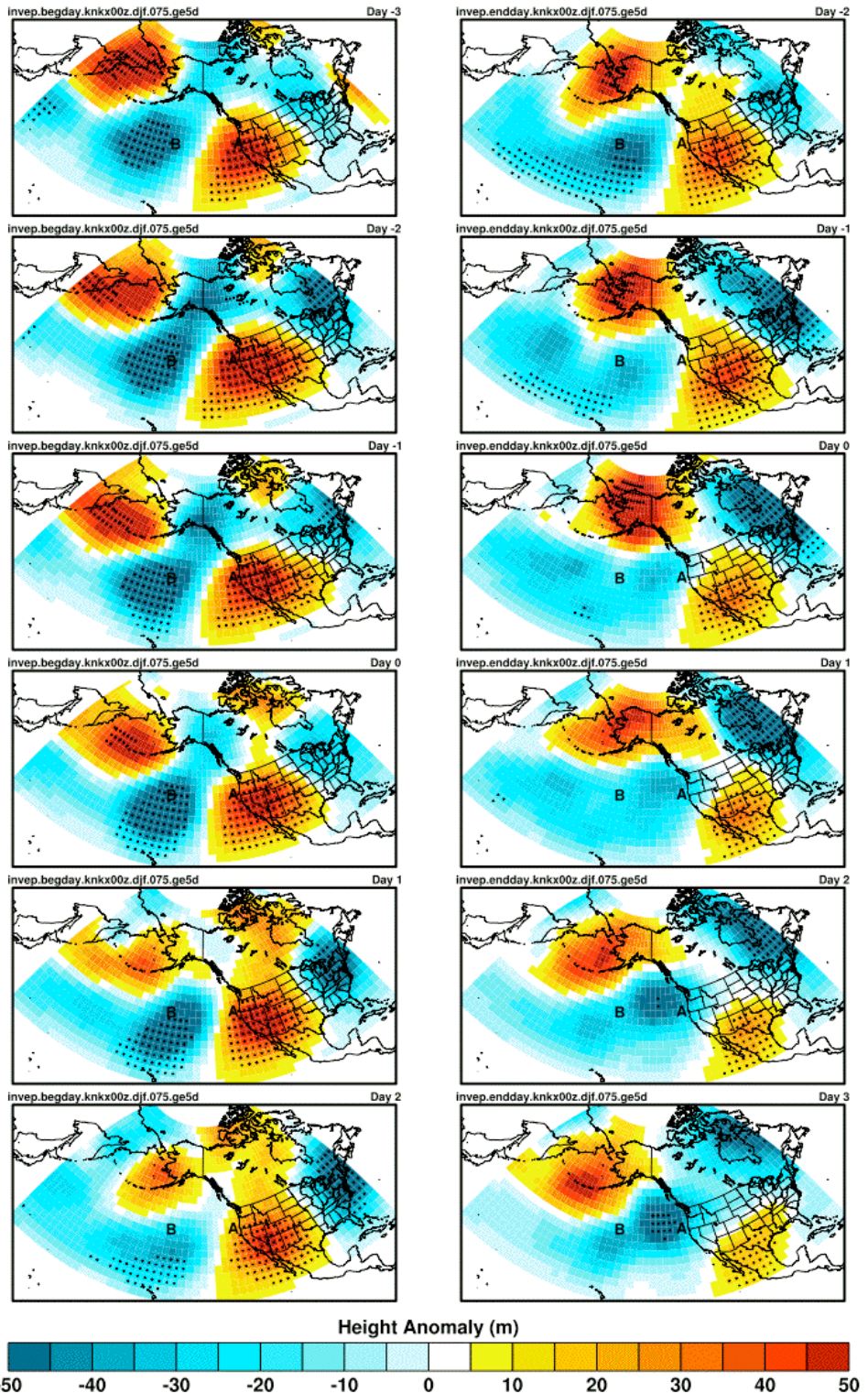
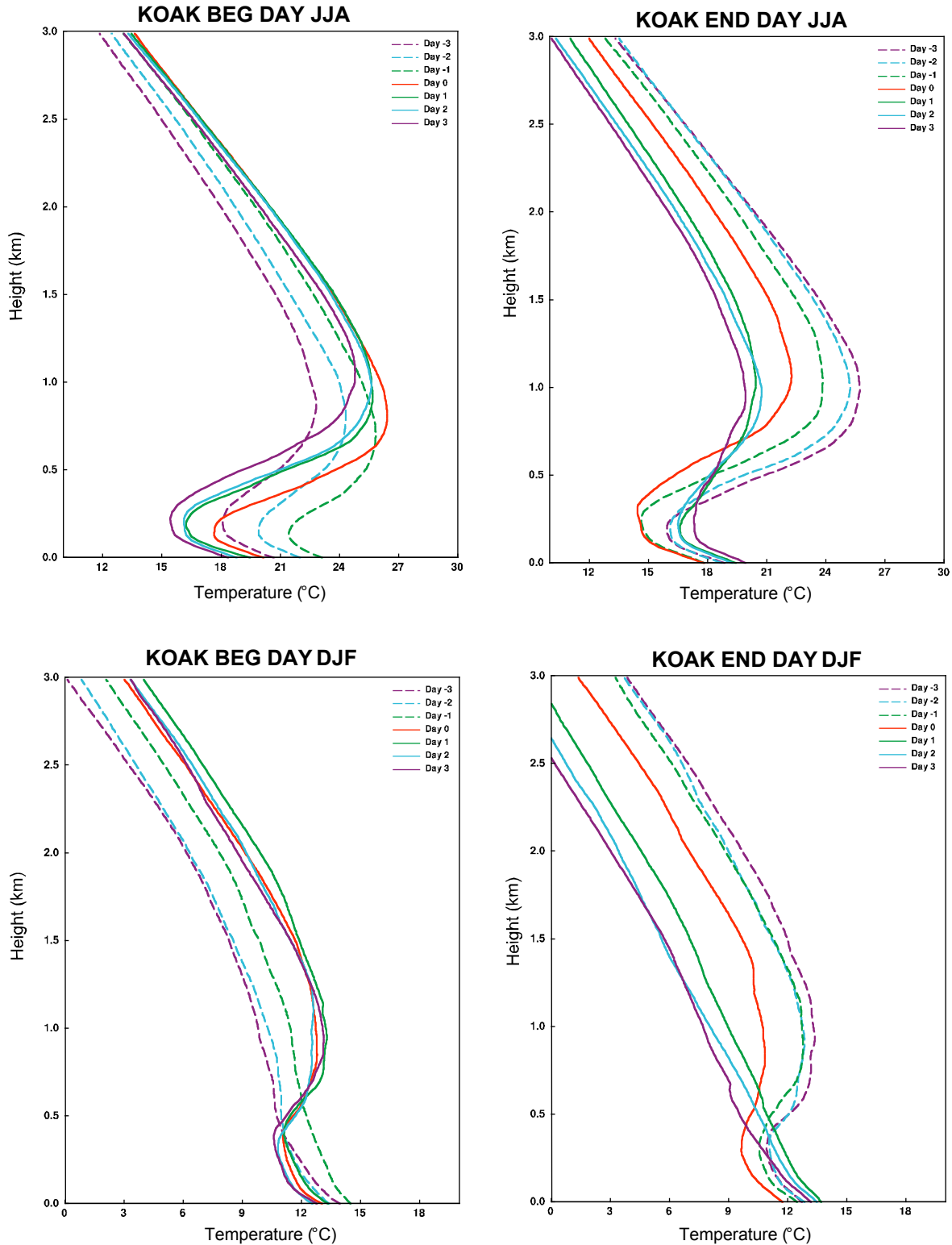
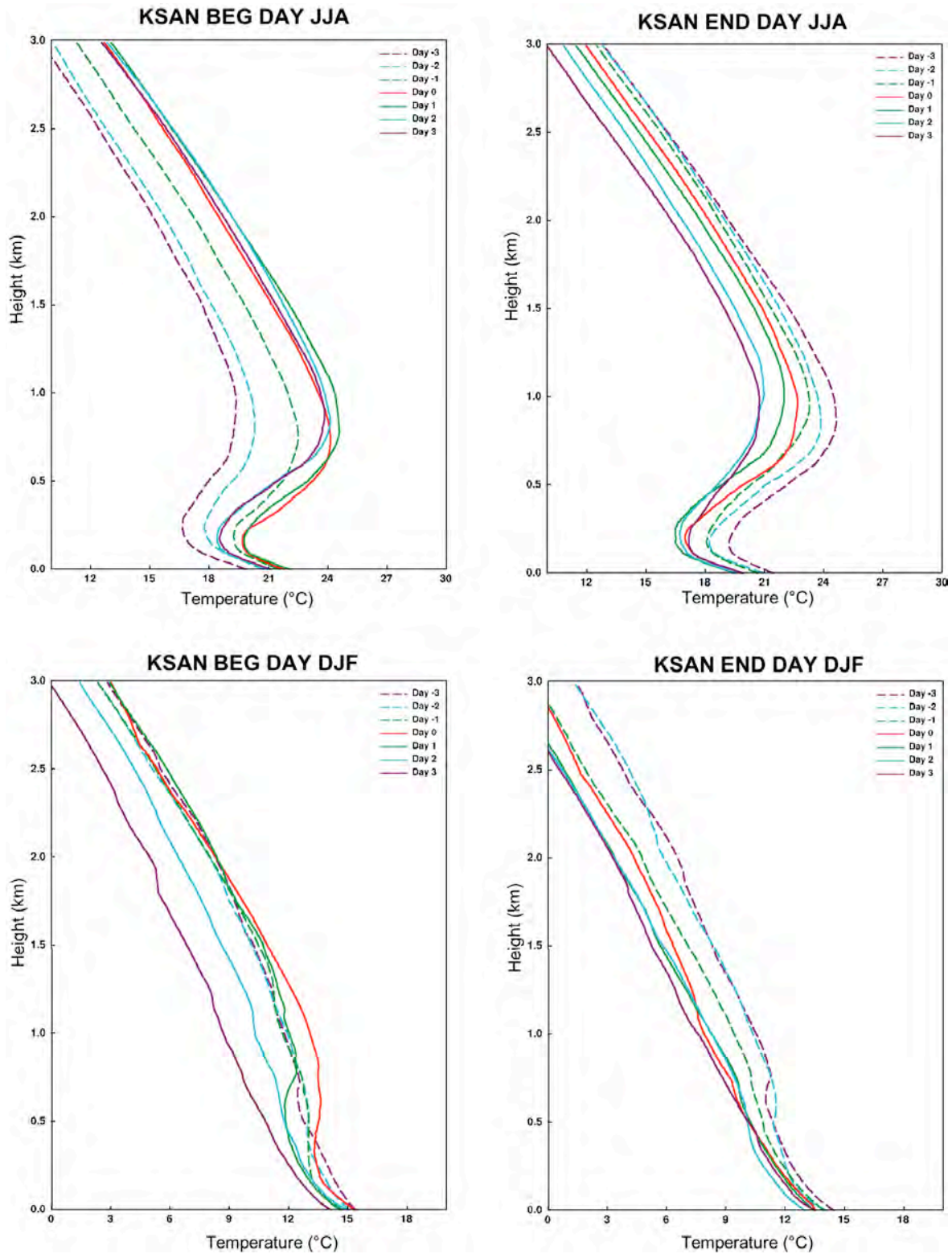


Figure 6-3b. Same as Figure 6-3a, except at San Diego.

The starting and ending days of persistent inversions lasting 5 days or longer were also used to produce composite vertical temperature profiles from the radiosonde observations shown in Figures 6-4 (Oakland) and 6-5 (San Diego). At Oakland during JJA, the days before the onset of a persistent episode are marked by warming above and below the inversion layer. During this period the inversion layer moves closer to the ground, with the top lowering more than the base resulting in a reduced inversion layer depth. The warming and height changes are associated with increasing geopotential heights as shown in Figures 6-2 and 6-3. On the first day of the episode, the temperature above the inversion continues to increase, while below the inversion the temperature decreases nearer the surface. Together, these temperature changes act to strengthen the inversion. The temperature below the inversion continues to decrease during the first few days of the episode while the temperature above the inversion remains nearly constant. The initial days of the episodes are marked by increasing inversion layer depth, primarily due to rising inversion top heights. The cooling of the boundary layer beneath the inversion during the onset of the episodes could be due to a strengthening sea breeze circulation bringing relatively cool marine air over the adjacent coastal inland areas and is discussed below in more depth. Marine stratus clouds advected over land by the sea breeze may also act to cool near surface temperatures. Two or three days prior to the end of the episodes, temperatures cool above and below the inversion. Also, the inversion layer becomes more elevated although there is little change to the overall depth of the layer. After the episodes end, temperatures above the inversion continue to cool while temperatures below the inversion warm. A decreasing sea breeze circulation would also account for this relative warming beneath the inversion. For DJF episodes at Oakland, a similar general pattern is observed although the temperature differences are not as pronounced and changes in inversion depths are not apparent.



**Figure 6-4.** Composite vertical temperature profiles for 3 days before and after the starting day (left column) and ending day (right column) of persistent strong inversion episodes lasting 5 days or longer at Oakland during JJA (top row) and DJF (bottom row).



**Figure 6-5.** Composite vertical temperature profiles for 3 days before and after the starting day (left column) and ending day (right column) of persistent strong inversion episodes lasting 5 days or longer at San Diego during JJA (top row) and DJF (bottom row).

For San Diego, the days before persistent inversion episodes during JJA are also associated with warming temperatures above and below the inversion along with decreasing inversion top and base heights, although there is little change in inversion layer depth. Once the strong persistent inversion episode begins, temperatures continue to warm above and below the inversion. The temperature increase above the inversion is greater than that below the inversion, thus strengthening the inversion. There are only minor changes in the inversion base and top height during these first few days of the episodes with a slight increase in overall layer depth. This is in contrast to changes at Oakland where temperatures below the inversion cooled once the episode started, implying that impacts from a sea-breeze circulation on the evolution of persistent inversion episodes are not as strong in San Diego during JJA. The composite profiles at San Diego during DJF show relatively slight changes between days making interpretation more difficult. However, it does appear that the inversion decays aloft suggesting a weakening of the large-scale support.

Figure 6-6 shows the composite time series of several surface (or near-surface) variables relative to +/- 5 days about the starting day of persistent JJA inversions for Oakland and San Diego. At Oakland, there is a significant increase in the coastal-inland (San Francisco-Sacramento) surface pressure gradient on day 0 (note: surface pressure measurements at Oakland were not available for much of the time period). Also, increases are observed in wind speed, cloud fraction and relative humidity and the temperature at 1pm decreases. During the preceding days, temperatures were increasing at both inland and coastal sites due to increasing geopotential heights. However, the marine influence allows more efficient nighttime cooling at coastal locations relative to inland sites and over the course of a few days will lead to increasing inland-coastal temperature differences, increasing surface pressure gradients and a stronger sea-breeze circulation. The strengthened sea-breeze circulation is also evident by decreasing surface temperature, increasing wind speed, and increasing relative humidity on day 0 at the Oakland coastal location.

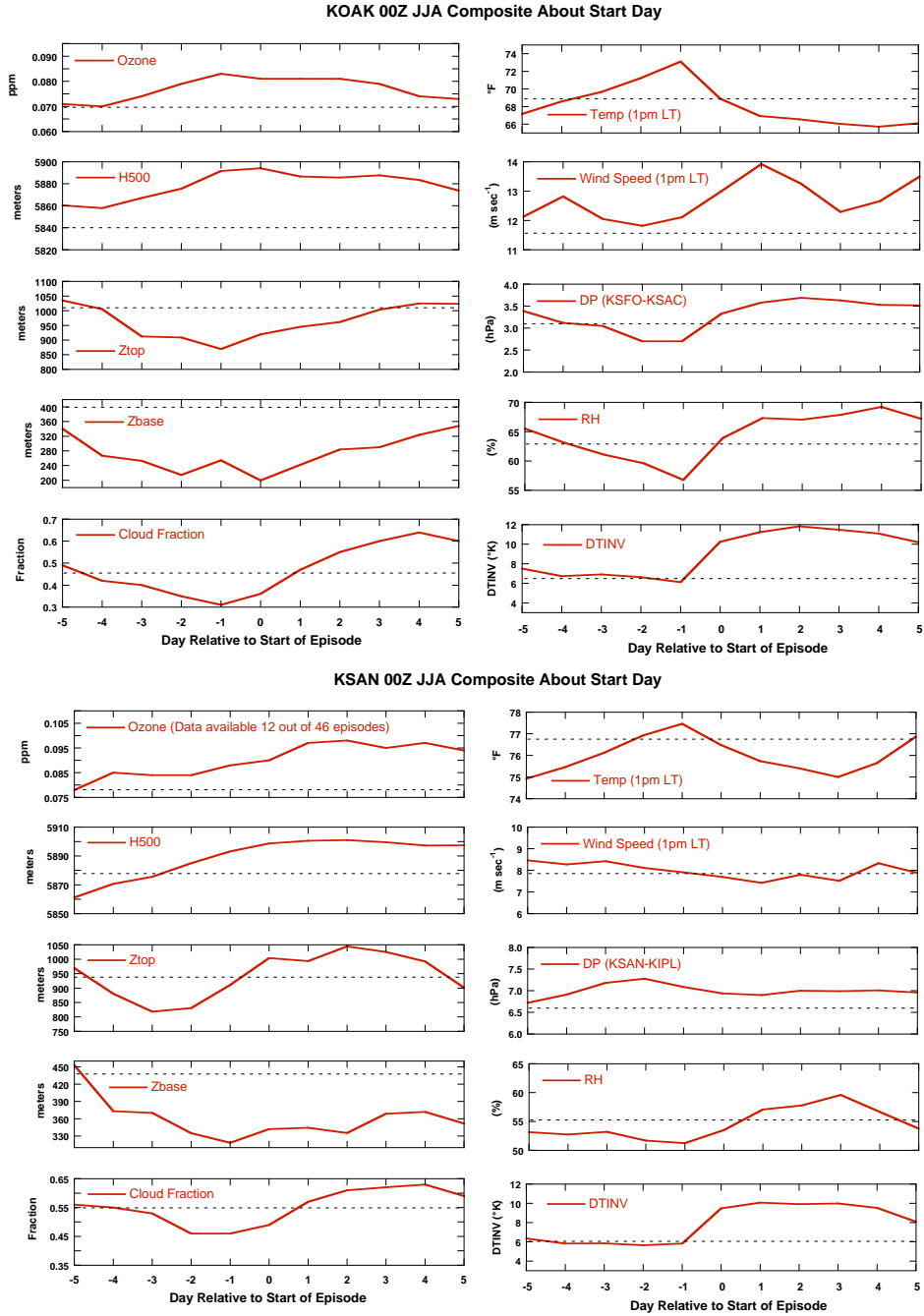


**Figure 6-6.** Composite time series of surface and near-surface variables on the starting day of persistent strong inversion episodes in JJA lasting 5 days or longer. The composite time series covers an 11-day period centered on the starting day of the persistent strong inversions. Time series are shown for Oakland (top) and San Diego (bottom).

Neither the coastal-inland surface pressure gradient (San Diego - Imperial) nor surface wind speed at San Diego shows much variability before or after the start of persistent inversion episodes. However, there is a decrease in coastal surface temperature and an increase in cloud

amount and relative humidity on day 0 at San Diego, but these changes are smaller than those noted at Oakland. Overall, this indicates that the sea-breeze circulation may have a weaker influence on the development of persistent inversion episodes at San Diego compared to Oakland. Also, the Oakland site is situated immediately adjacent to San Francisco Bay while the San Diego site is located approximately 10 km inland.

During DJF (Figure 6-7), the composite time-series of coastal-inland pressure gradient does not exhibit any significant changes around the onset of persistent inversion episodes at either location and this may be due in part to the stronger synoptic environment in place during these months. At Oakland, there is little signature of a strengthened (or weakened) sea-breeze circulation among coastal surface temperature, wind speed, cloud amount and relative humidity. However, at San Diego, there is a large increase in cloudiness and relative humidity and decreasing coastal surface temperatures, but no significant change in surface wind speed.

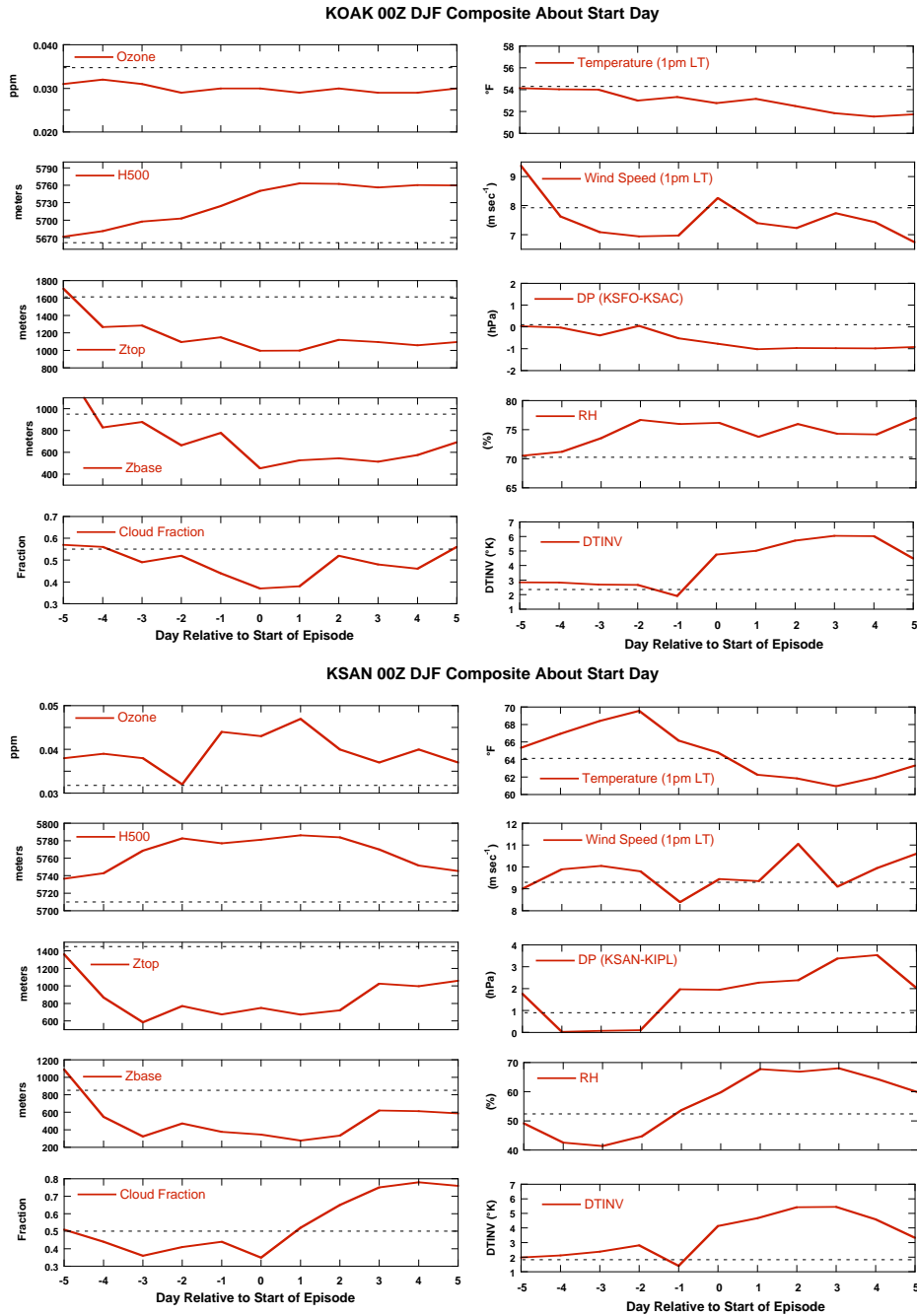


**Figure 6-7.** Composite time series of surface and near-surface variables on the starting day of persistent strong inversion episodes in DJF lasting 5 days or longer. The composite time series covers an 11-day period centered on the starting day of the persistent strong inversions. Time series are shown for Oakland (top) and San Diego (bottom).

## **7.0 TEMPORAL VARIABILITY OF INVERSION MEASURES DURING HISTORICAL PERIOD**

### ***7.1 Time Series of Inversion Strength and Inversion Depth***

To investigate how inversions may vary on interannual and multi-year time scales, time series of monthly mean  $DT_{INV}$ ,  $DZ_{INV}$ , and  $Z_{BASE}$  anomalies were constructed from radiosonde measurements at Oakland and San Diego. Additionally, time series of monthly mean  $D\theta_{850,SJV}$  and  $D\theta_{850,SC}$  anomalies were made using the radiosonde data and surface temperature measurements in the San Joaquin Valley and South Coast Air Basins.

For this analysis, the "reconstructed" radiosonde data set was utilized as discussed earlier in Section 2. The reconstructed data used a consistent set of criteria for the entire 1960-2007 historical period to determine which data levels to include. This was done to remove any potential biasing of long-term trends due to changes in the criteria used to originally report the data levels.

Time series of  $DT_{INV}$ ,  $D\theta_{850}$ ,  $DZ_{INV}$ , and  $Z_{BASE}$  are shown in Figure 7-1 (Oakland/SJVAB) and Figure 7-2 (San Diego/SOCAB). The monthly means shown in these figures only include data for subsidence inversions ( $Z_{BASE} > 50$  m). The number of days with subsidence inversions varied with month, but was generally (90% of the months) greater than 10. Radiation inversions are examined separately below. The monthly mean anomalies were calculated using monthly climatologies computed from the entire 1960–2007 period.

## Oakland/SJVAB Subsidence Inversions

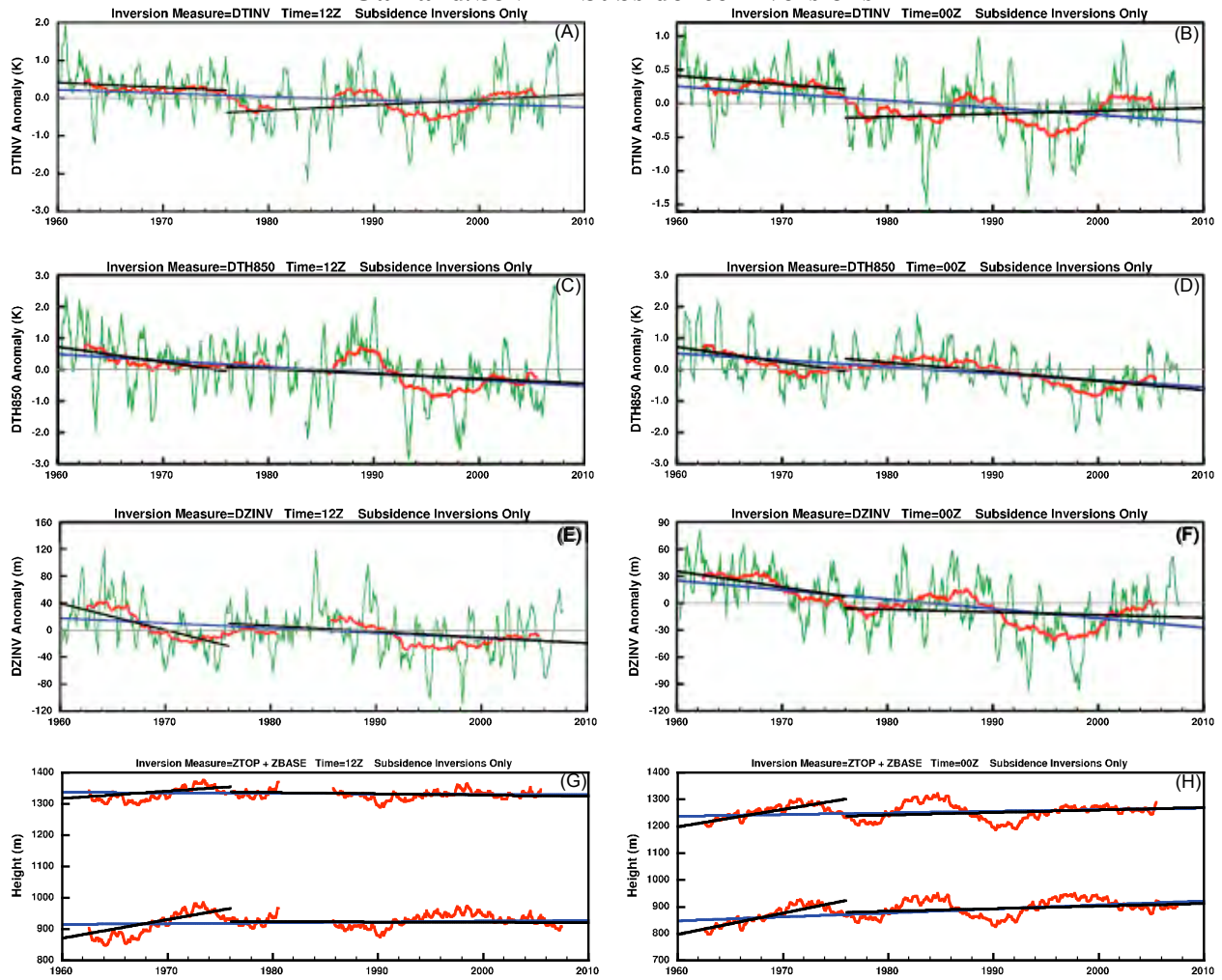


**Figure 7-1.** Time series of filtered monthly mean values of (a) 12Z  $DT_{INV}$ , (b) 00Z  $DT_{INV}$ , (c) 12Z  $D\theta_{850,SJV}$ , (d) 00Z  $D\theta_{850,SJV}$ , (e) 12Z  $DZ_{INV}$ , (f) 00Z  $DZ_{INV}$ , (g) 12Z  $Z_{TOP}$  and  $Z_{BASE}$ , and (h) 00Z  $Z_{TOP}$  and  $Z_{BASE}$  based on the Oakland radiosonde data and surface temperature measurements in the San Joaquin Valley Air Basin. For each variable a six-month running mean (green line) and a five-year running mean filter (red line) are shown except for the bottom row of plots showing  $Z_{TOP}$  and  $Z_{BASE}$ , where only the five-year running mean filtered data are shown for clarity. The straight blue lines represent a linear best fit to the data for the entire 1960-2007 period. The straight black lines represent linear fits for the periods 1960-1975 and 1976-2007. The monthly means were calculated using only days when subsidence inversions were observed. Note: Data gaps in some of the filtered data curves are due to some months with no subsidence inversions.

## San Diego/SOCAB Subsidence Inversions

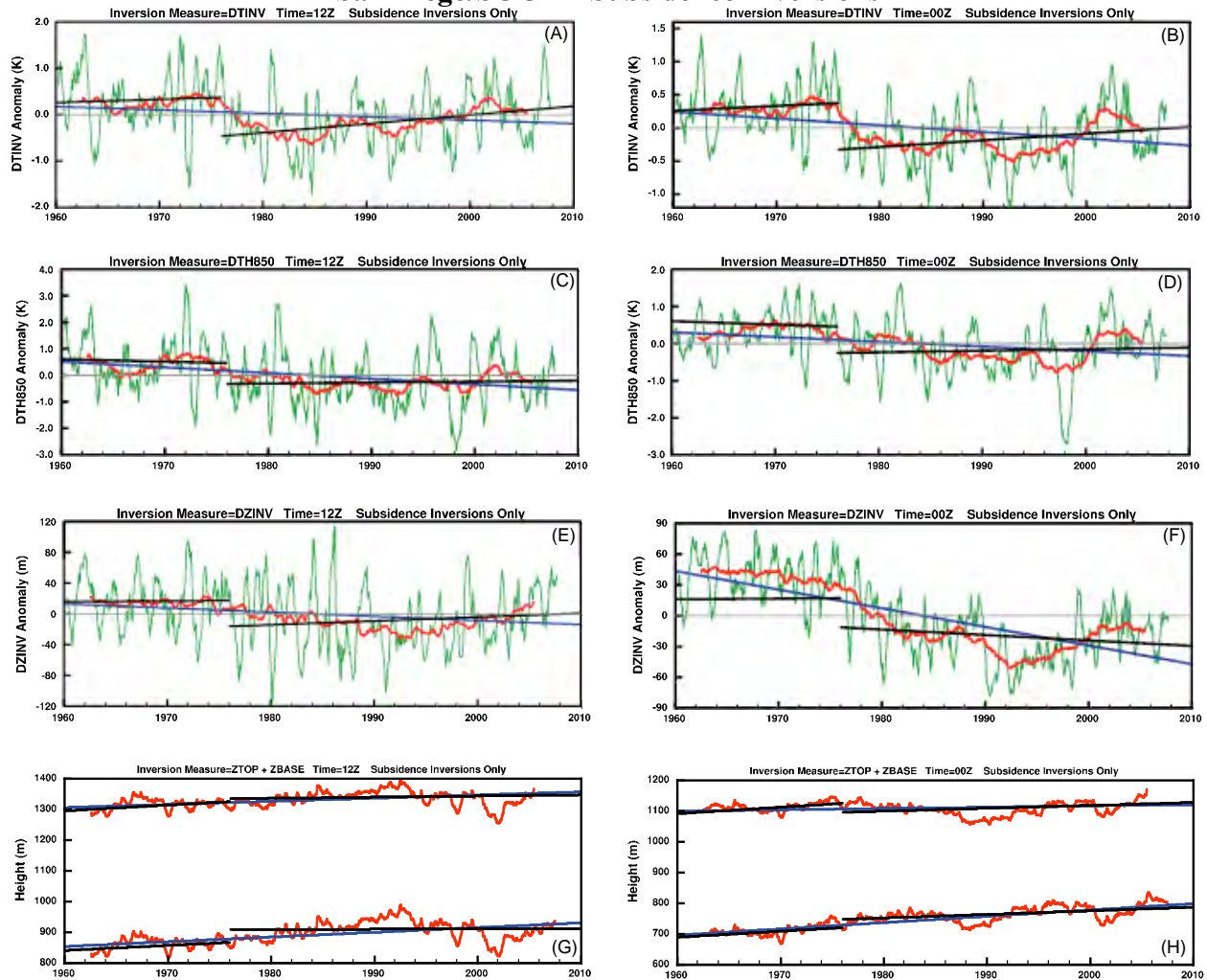


**Figure 7-2.** Time series of filtered monthly mean values of (a) 12Z  $DT_{INV}$ , (b) 00Z  $DT_{INV}$ , (c) 12Z  $D\theta_{850,SC}$ , (d) 00Z  $D\theta_{850,SC}$ , (e) 12Z  $DZ_{INV}$ , (f) 00Z  $DZ_{INV}$ , (g) 12Z  $Z_{TOP}$  and  $Z_{BASE}$ , and (h) 00Z  $Z_{TOP}$  and  $Z_{BASE}$  based on the San Diego radiosonde data and surface temperature measurements in the South Coast Air Basin. For each variable a six-month running mean (green line) and a five-year running mean filter (red line) are shown, except for the bottom row of plots showing  $Z_{TOP}$  and  $Z_{BASE}$  where only the five-year running mean filtered data are shown for clarity. The straight blue lines represent a linear best fit to the data for the entire 1960-2007 period. The straight black lines represent linear fits for the periods 1960-1975 and 1976-2007. The monthly means were calculated using only days when subsidence inversions were observed.

The time series in Figures 7-1 and 7-2 contain significant interannual and decadal variability. To determine if these fluctuations are linked to large-scale fluctuations in Pacific climate, correlations between of  $DT_{INV}$  and  $DZ_{INV}$  versus the ENSO and the PDO were computed, shown

in Table 7-1. Annual mean values of  $DT_{INV}$  and  $DZ_{INV}$  were calculated using only those days when a subsidence inversion was present; days with radiation inversions were not included. The ENSO variations were represented by the SOI and by the Niño 3.4 (East Central Tropical Pacific extending from 5°N-5°S; 190-240°E) SST, and the PDO was represented the leading principal component of monthly SST anomalies in the North Pacific Ocean poleward of 20°N, as derived by Zhang et al (1997) (available online at <http://jisao.washington.edu/pdo/>). A twelve-month running mean filter was applied to all time series. Correlations were calculated using a lead time of 1 month for ENSO and 2 months for SOI and Niño 3.4 SST. After accounting for autocorrelations in the time series, it was found that correlations greater than 0.28 are significant at the 95% confidence level.

**Table 7-1.** Correlation between 1960–2007 filtered monthly means: Inversion measures vs. SST indices. Monthly means of the inversion measures are for subsidence inversions only. The time series were detrended and then filtered using a 12-month running mean. Correlations greater than 0.28 are significant at the 95% confidence level.

	PDO Index	SOI Index	Niño 3.4
Oakland			
$DT_{INV}$ 00Z	-0.43	+0.34	-0.24
$DZ_{INV}$ 00Z	-0.29	+0.20	-0.13
$DT_{INV}$ 12Z	-0.43	+0.33	-0.25
$DZ_{INV}$ 12Z	-0.10	+0.12	-0.18
San Diego			
$DT_{INV}$ 00Z	-0.49	+0.51	-0.40
$DZ_{INV}$ 00Z	-0.54	+0.40	-0.33
$DT_{INV}$ 12Z	-0.58	+0.51	-0.43
$DZ_{INV}$ 12Z	-0.42	+0.45	-0.40

Although inversion measures of  $DT_{INV}$  and  $DZ_{INV}$  are not real strongly associated with ENSO, there are significant correlations (Table 7-1). Stronger and thicker inversions are positively correlated with the SOI Index and negatively correlated with the Niño 3.4 SST record, with correlation magnitudes of approximately 0.2–0.5. Thus, during El Niño episodes (warm SST in Central Tropical Pacific and off the California coast), weaker and thinner inversion layers tend to occur in California. The opposite is true during La Niña events, when stronger and thicker inversions occur. The correlations are largest for San Diego, indicating that the ENSO linkage

may fade northward along the California coast. Weaker inversions during El Niño episodes appear to be consistent with the tendency for strengthened westerly winds and presumably more frequent synoptic events during these cases. There is a greater tendency for horizontal warm advection during El Niño episodes, which leads to higher surface temperatures on land and the coastal ocean. Vertical cold advection occurs at 850 hPa, leading to relative cooling at that level and consequently weaker inversions. Stronger inversions during La Niñas would likely result from more frequent high-pressure situations and more vertical warm advection during these cases.

There is also a connection to PDO. Table 7-1 shows significant correlations, up to about -0.6 between these inversion measures and the PDO, at both locations. The sense of these correlations indicates that stronger and thicker inversions occur with the cool phase (relatively cool SST in the eastern Pacific off North America) of the PDO. This link is consistent with the ENSO correlation results, since the cool phase of PDO is more La Niña-like and the warm phase of PDO is more El Niño-like. Over the available historical period, inversions were stronger and thicker during the cool PDO phase during the 1960s through the mid-1970s and during the recent period after 1998, while they were weaker and thinner during the PDO warm phase that prevailed from the mid-1970s through 1998. Similar to the ENSO results, the correlations between inversion measures and the PDO are stronger at San Diego compared to Oakland.

In addition to having substantial interannual-decadal fluctuations, the inversion characteristics have undergone some notable long-term changes over the historical observation period of 1960-2007. Changes over this period were calculated using a best-fit linear trend through the monthly mean data.

Over the 48-year period, inversion strength as measured by  $DT_{INV}$  decreased at Oakland by 8% ( $0.4^{\circ}\text{C}$ ) at 12Z and by 14% ( $0.5^{\circ}\text{C}$ ) at 00Z. Comparable decreases in  $DT_{INV}$  of 6% ( $0.4^{\circ}\text{C}$ ) at 12Z and 13% ( $0.5^{\circ}\text{C}$ ) at 00Z were observed at San Diego. Separate measures,  $D\theta_{850,SJV}$  and  $D\theta_{850,SC}$ , formed from 850 hPa potential temperature from the radiosonde profiles and surface temperature from clusters of cooperative observer stations, showed changes of similar magnitude. A somewhat fragmentary record from radiosonde observations at Vandenberg Air Force Base also

exhibits similar decreases. Furthermore, the thickness of the inversion layer decreased over this time period. At Oakland,  $DZ_{INV}$  decreased by 9% (35 m) at 12Z and 14% (50 m) at 00Z, while at San Diego decreases of 6% (26 m) at 12Z and 24% (87 m) at 00Z were observed.

At both sites the decrease in inversion thickness is primarily due to a lifting of the inversion base. The altitude of the inversion top also increases during the period, but at a much slower rate. Temperature increased by 0.8–1.1°C at the inversion base while inversion top temperatures increased by 0.2–0.7°C. The larger increase in inversion base temperature resulted in the decreasing trend in  $DT_{INV}$  noted earlier. When these values are normalized with the standard deviation, the increases in inversion base temperature also appear to be more significant. Additionally, the soundings consistently show larger temperature increases at the 500 hPa level compared to 850 hPa ( $\Delta T_{500} - \Delta T_{850} \sim 0.3^\circ\text{C}$ ), which leads to an increased static stability in this region of atmosphere over both Oakland and San Diego. The increasing trend in  $T_{500}$  appears to be stronger (both in absolute and normalized terms) than the trend in  $T_{850}$ , while the trend in static stability is relatively weaker with respect to values normalized with the standard deviation.

Upon close examination of the smoothed curves in Figures 7-1 and 7-2 it appears that a "shift" in the values the inversion measures often occurred during the mid-1970s. To illustrate this, short black lines are included in these figures to show the linear trends for two sub-periods, 1960-1975 and 1976-2007. For instance, the trends in  $DT_{INV}$  at both locations and sounding times show a decrease in  $DT_{INV}$  for the 1960-2007 period, an increase is noted for the shorter 1976-2007 period. The value of  $DT_{INV}$  decreased significantly over a very short period of time in the mid-1970s and is responsible for the opposite trends. Trends in the inversion thickness over the 1976-2007 period generally show a decreasing trend, but the magnitude of the decrease is generally less than that seen for the longer 1960-2007 period.

It is possible that the climate shift in the mid-1970s related to the PDO may be responsible for these different trends. As discussed earlier, there are significant correlations between the PDO index and  $DT_{INV}$  and  $DZ_{INV}$ . It is also possible that changes in radiosonde equipment and/or criteria used to process the raw radiosonde data are responsible. The trends shown in Figures 7-1 and 7-2 were derived using the "reconstructed" radiosonde data sets described in Section 2 that

attempt to reduce ambiguities related to such changes in equipment and/or procedures. However, it is quite possible that not all the impacts from these changes were removed.

Other attempts have also been made to adjust radiosonde data to remove inconsistencies arising from changes in procedures and/or instrumentation. To aid in the application of this information to climate change studies, corrections to global radiosonde data sets have been made by Free et al. (2005) (RATPAC), Thorne et al. (2005) (HadAT2), and Haimberger (2005) (RAOBCORE). Each of these studies used a different and independent methodology to determine the temperature adjustments to remove inhomogeneities. The San Diego radiosonde data was included in all three studies, while the Oakland radiosonde data was included in only two of the studies. Unfortunately, the adjustments only apply to the standard pressure levels and are generally not available between the surface and 850 hPa where the vast majority of low-level temperature inversions are located. For this reason these adjustments were not directly used in the above analysis.

Investigation of trends in the adjusted temperature datasets, however, may provide some insight into the reliability of trends found in Figures 7-1 and 7-2. Each of the adjusted radiosonde data sets yielded similar increasing trends in  $T_{850}$  over the 48-year period at San Diego that averaged about  $0.2^{\circ}\text{C}$  ( $0.4^{\circ}\text{F}$ ) larger than what was found with the original radiosonde data. This would imply that the decreasing trend in  $D\theta_{850,SC}$  may be about  $0.2^{\circ}\text{C}$  ( $0.4^{\circ}\text{F}$ ) too large in magnitude, since the surface temperatures were already subject to a correction procedure. One of the two adjusted radiosonde data sets available for the Oakland site (HadAT2) consistently produced a more positive  $T_{850}$  trend than was in the original radiosonde data, and the other (RAOBCORE) consistently produced a more negative trend. This implies that the uncertainty in the Oakland trends is larger than what may be estimated from the original data alone, especially considering that the three data sets did not agree on the sign of the wintertime Oakland  $T_{850}$  trend. When combined with the surface data, the three radiosonde data sets indicate that wintertime  $D\theta_{850,SJV}$  experienced a trend that was near zero or increasing.

If the adjustments to the radiosonde temperature data are uniform in height below the 850 hPa level, then there would probably be little if any change to the  $DT_{INV}$  trends calculated here.

Additionally, trends in the thickness of the inversion layer  $DZ_{INV}$  would also be minimally affected, since the inflection points in the temperature profile would not change if a continuous temperature adjustment was applied.

Nonetheless, changes to equipment and/or algorithms used to derive radiosonde heights and temperatures could impart artificial trends to the radiosonde heights and temperatures. It is more likely that any artificial trend would affect the calculated trend at a particular level such as inversion base or inversion top. It is less likely that an artificial trend would have a significant impact on the difference between values at two different levels such as  $DT_{INV}$  or  $DZ_{INV}$  unless there has been a change in sensor response time. Although the radiosonde models examined by Gaffen (1994) were not used in the United States, if the technology was similar, then there are likely to have been no significant changes in sensor response time between the mid 1970s until at least the early 1990s.

Correlations between various inversion measures are displayed in Tables 7-2 to 7-5 for both daily values and monthly means. These correlations were calculated using only days when a subsidence inversion was measured with the resulting time series detrended. Results are presented at the 00Z launch time to maximize the occurrence of subsidence-type inversions to prevent biases in monthly means. Several of the measures are strongly correlated ( $r > 0.5$ ,  $p < 0.01$ ). These include a strong positive correlation between  $DT_{INV}$  and  $DZ_{INV}$  on monthly time scales, indicating that stronger/weaker inversions are also thicker/thinner in vertical extent. Strong anti-correlations exist for the temperature and height at the base and top of the inversion layer for both daily and monthly time scales. Additionally,  $T_{TOP}$  and  $T_{BASE}$  are strongly correlated with  $T_{850}$  and to a lesser extent with  $T_{500}$ . In general, the correlations between the various temperatures decrease as the physical distance between the locations increase. The thickness of the inversion is not significantly correlated with either  $Z_{TOP}$  or  $Z_{BASE}$ , a reflection of the two height measures being so strongly correlated, and thus the difference was not too well correlated with either measure. The stability of the atmospheric layer between 850 hPa and 500 hPa is strongly correlated to  $T_{850}$ , but weakly correlated with  $T_{500}$ . This perhaps indicates that the dynamics driving the temperatures at the 850 hPa level are more relevant to low-level temperature inversions in California than the dynamics at 500 hPa.

**Table 7-2.** Correlation of daily values from 1960–2007 Oakland 00Z radiosonde measurements. The correlations were calculated using only days when a subsidence inversion was observed in the radiosonde data. The various time series were detrended prior to calculation.

	DT <sub>INV</sub>	DZ <sub>INV</sub>	Z <sub>TOP</sub>	Z <sub>BASE</sub>	Dθ <sub>850</sub>	T <sub>TOP</sub>	T <sub>BASE</sub>	T <sub>850</sub>	T <sub>500</sub>	DθDZ <sub>850-500</sub>	θ <sub>TOP</sub>	θ <sub>BASE</sub>	θ <sub>2M</sub>
DT <sub>INV</sub>	1.00												
DZ <sub>INV</sub>	0.46	1.00											
Z <sub>TOP</sub>	-0.08	0.16	1.00										
Z <sub>BASE</sub>	-0.25	-0.21	0.93	1.00									
Dθ <sub>850,SJV</sub>	0.34	0.27	-0.36	-0.45	1.00								
T <sub>TOP</sub>	0.38	0.19	-0.73	-0.79	0.58	1.00							
T <sub>BASE</sub>	-0.08	-0.02	-0.75	-0.73	0.46	0.89	1.00						
T <sub>850</sub>	0.45	0.29	-0.51	-0.61	0.68	0.91	0.76	1.00					
T <sub>500</sub>	0.18	0.16	-0.23	-0.29	0.38	0.55	0.50	0.60	1.00				
DθDZ <sub>850-500</sub>	-0.38	-0.20	0.41	0.48	-0.48	-0.60	-0.46	-0.66	0.21	1.00			
θ <sub>TOP</sub>	0.43	0.47	0.31	0.14	0.32	0.42	0.24	0.59	0.45	-0.30	1.00		
θ <sub>BASE</sub>	-0.44	-0.31	0.28	0.39	-0.01	0.11	0.34	0.19	0.28	0.03	0.53	1.00	
θ <sub>2M</sub>	0.28	0.12	-0.34	-0.38	-0.07	0.66	0.58	0.68	0.44	-0.42	0.48	0.27	1.00

**Table 7-3.** Correlation of monthly means from 1960–2007 Oakland 00Z radiosonde measurements. The monthly means were calculated using only those days when a subsidence inversion was observed in the radiosonde data. The various time series were detrended prior to calculation.

	DT <sub>INV</sub>	DZ <sub>INV</sub>	Z <sub>TOP</sub>	Z <sub>BASE</sub>	Dθ <sub>850</sub>	T <sub>TOP</sub>	T <sub>BASE</sub>	T <sub>850</sub>	T <sub>500</sub>	DθDZ <sub>850-500</sub>	θ <sub>TOP</sub>	θ <sub>BASE</sub>	θ <sub>2M</sub>
DT <sub>INV</sub>	1.00												
DZ <sub>INV</sub>	0.70	1.00											
Z <sub>TOP</sub>	-0.24	0.03	1.00										
Z <sub>BASE</sub>	-0.46	-0.36	0.94	1.00									
Dθ <sub>850,SJV</sub>	0.47	0.46	-0.35	-0.48	1.00								
T <sub>TOP</sub>	0.52	0.37	-0.75	-0.83	0.53	1.00							
T <sub>BASE</sub>	0.12	0.10	-0.76	-0.74	0.38	0.91	1.00						
T <sub>850</sub>	0.55	0.43	-0.61	-0.71	0.57	0.96	0.85	1.00					
T <sub>500</sub>	0.28	0.33	-0.29	-0.38	0.36	0.65	0.62	0.71	1.00				
DθDZ <sub>850-500</sub>	-0.48	-0.26	0.57	0.61	-0.44	-0.68	-0.56	-0.67	0.04	1.00			
θ <sub>TOP</sub>	0.52	0.53	-0.02	-0.19	0.40	0.67	0.52	0.77	0.66	-0.40	1.00		
θ <sub>BASE</sub>	-0.42	-0.33	0.14	0.25	-0.08	0.23	0.47	0.30	0.40	-0.01	0.51	1.00	
θ <sub>2M</sub>	0.23	0.10	-0.41	-0.42	-0.22	0.67	0.67	0.67	0.52	-0.41	0.56	0.43	1.00

**Table 7-4.** Correlation of daily values from 1960–2007 San Diego 00Z radiosonde measurements. The correlations were calculated using only days when a subsidence inversion was observed in the radiosonde data. The various time series were detrended prior to calculation.

	DT <sub>INV</sub>	DZ <sub>INV</sub>	Z <sub>TOP</sub>	Z <sub>BASE</sub>	Dθ <sub>850</sub>	T <sub>TOP</sub>	T <sub>BASE</sub>	T <sub>850</sub>	T <sub>500</sub>	DθDZ <sub>850-500</sub>	θ <sub>TOP</sub>	θ <sub>BASE</sub>	θ <sub>2M</sub>
DT <sub>INV</sub>	1.00												
DZ <sub>INV</sub>	0.34	1.00											
Z <sub>TOP</sub>	-0.02	0.30	1.00										
Z <sub>BASE</sub>	-0.14	-0.05	0.94	1.00									
Dθ <sub>850,SC</sub>	0.55	0.32	-0.29	-0.42	1.00								
T <sub>TOP</sub>	0.33	0.10	-0.75	-0.82	0.48	1.00							
T <sub>BASE</sub>	-0.06	-0.03	-0.79	-0.81	0.28	0.92	1.00						
T <sub>850</sub>	0.40	0.21	-0.56	-0.66	0.65	0.91	0.80	1.00					
T <sub>500</sub>	0.15	0.13	-0.22	-0.27	0.32	0.43	0.39	0.46	1.00				
DθDZ <sub>850-500</sub>	-0.32	-0.13	0.46	0.53	-0.48	-0.69	-0.60	-0.76	0.22	1.00			
θ <sub>TOP</sub>	0.46	0.57	0.29	0.09	0.31	0.42	0.25	0.55	0.32	-0.37	1.00		
θ <sub>BASE</sub>	-0.33	-0.12	0.16	0.21	-0.18	0.25	0.49	0.30	0.22	-0.17	0.57	1.00	
θ <sub>2M</sub>	0.06	0.01	-0.50	-0.52	0.02	0.80	0.82	0.77	0.34	-0.60	0.47	0.55	1.00

**Table 7-5.** Correlation of monthly means from 1960–2007 San Diego 00Z radiosonde measurements. The monthly means were calculated using only those days when a subsidence inversion was observed in the radiosonde data. The various time series were detrended prior to calculation.

	DT <sub>INV</sub>	DZ <sub>INV</sub>	Z <sub>TOP</sub>	Z <sub>BASE</sub>	Dθ <sub>850</sub>	T <sub>TOP</sub>	T <sub>BASE</sub>	T <sub>850</sub>	T <sub>500</sub>	DθDZ <sub>850-500</sub>	θ <sub>TOP</sub>	θ <sub>BASE</sub>	θ <sub>2M</sub>
DT <sub>INV</sub>	1.00												
DZ <sub>INV</sub>	0.63	1.00											
Z <sub>TOP</sub>	-0.20	0.07	1.00										
Z <sub>BASE</sub>	-0.39	-0.26	0.95	1.00									
Dθ <sub>850,SC</sub>	0.76	0.57	-0.31	-0.48	1.00								
T <sub>TOP</sub>	0.47	0.28	-0.80	-0.86	0.51	1.00							
T <sub>BASE</sub>	0.12	0.05	-0.82	-0.81	0.26	0.93	1.00						
T <sub>850</sub>	0.54	0.35	-0.66	-0.75	0.61	0.96	0.86	1.00					
T <sub>500</sub>	0.25	0.23	-0.38	-0.44	0.44	0.58	0.54	0.62	1.00				
DθDZ <sub>850-500</sub>	-0.49	-0.26	0.56	0.63	-0.44	-0.79	-0.68	-0.80	-0.03	1.00			
θ <sub>TOP</sub>	0.54	0.53	-0.12	-0.29	0.46	0.70	0.56	0.79	0.50	-0.63	1.00		
θ <sub>BASE</sub>	-0.34	-0.26	-0.06	0.03	-0.23	0.38	0.57	0.41	0.31	-0.28	0.55	1.00	
θ <sub>2M</sub>	0.10	0.01	-0.60	-0.58	0.00	0.82	0.89	0.80	0.45	-0.68	0.65	0.70	1.00

**Table 7-6.** Correlation of low-frequency subsidence inversion variability (five-year running mean filter) from 1960–2007 Oakland 00Z radiosonde measurements. The various time series were detrended prior to calculation.

	DT <sub>INV</sub>	DZ <sub>INV</sub>	Z <sub>TOP</sub>	Z <sub>BASE</sub>	Dθ <sub>850</sub>	T <sub>TOP</sub>	T <sub>BASE</sub>	T <sub>850</sub>	T <sub>500</sub>	DθDZ <sub>850-500</sub>	θ <sub>TOP</sub>	θ <sub>BASE</sub>	θ <sub>2M</sub>
DT <sub>INV</sub>	1.00												
DZ <sub>INV</sub>	0.80	1.00											
Z <sub>TOP</sub>	0.13	0.37	1.00										
Z <sub>BASE</sub>	-0.47	-0.38	0.72	1.00									
Dθ <sub>850,SJV</sub>	-0.16	0.18	0.00	-0.13	1.00								
T <sub>TOP</sub>	0.24	0.14	-0.63	-0.74	0.47	1.00							
T <sub>BASE</sub>	-0.44	-0.39	-0.67	-0.37	0.55	0.77	1.00						
T <sub>850</sub>	0.14	0.11	-0.46	-0.54	0.61	0.95	0.79	1.00					
T <sub>500</sub>	0.01	0.19	0.21	0.07	0.42	0.36	0.32	0.47	1.00				
DθDZ <sub>850-500</sub>	-0.13	0.04	0.66	0.62	-0.33	-0.74	-0.59	-0.70	0.30	1.00			
θ <sub>TOP</sub>	0.44	0.62	0.45	-0.02	0.57	0.41	0.09	0.56	0.63	-0.09	1.00		
θ <sub>BASE</sub>	-0.80	-0.67	0.01	0.51	0.42	0.08	0.60	0.28	0.35	-0.02	0.09	1.00	
θ <sub>2M</sub>	0.36	-0.03	-0.56	-0.53	-0.29	0.67	0.38	0.57	0.14	-0.51	0.10	-0.12	1.00

**Table 7-7.** Correlation of low-frequency subsidence inversion variability (five-year running mean filter) from 1960–2007 San Diego 00Z radiosonde measurements. The various time series were detrended prior to calculation.

	DT <sub>INV</sub>	DZ <sub>INV</sub>	Z <sub>TOP</sub>	Z <sub>BASE</sub>	Dθ <sub>850</sub>	T <sub>TOP</sub>	T <sub>BASE</sub>	T <sub>850</sub>	T <sub>500</sub>	DθDZ <sub>850-500</sub>	θ <sub>TOP</sub>	θ <sub>BASE</sub>	θ <sub>2M</sub>
DT <sub>INV</sub>	1.00												
DZ <sub>INV</sub>	0.90	1.00											
Z <sub>TOP</sub>	0.18	0.43	1.00										
Z <sub>BASE</sub>	-0.81	-0.74	0.30	1.00									
Dθ <sub>850,SC</sub>	0.74	0.67	0.20	-0.56	1.00								
T <sub>TOP</sub>	0.48	0.49	-0.32	-0.75	0.50	1.00							
T <sub>BASE</sub>	-0.66	-0.54	-0.47	0.22	-0.35	0.34	1.00						
T <sub>850</sub>	0.21	0.24	-0.26	-0.44	0.41	0.90	0.56	1.00					
T <sub>500</sub>	-0.28	-0.11	0.05	0.16	-0.05	0.27	0.53	0.57	1.00				
DθDZ <sub>850-500</sub>	-0.51	-0.34	0.31	0.59	-0.45	-0.54	0.07	-0.31	0.61	1.00			
θ <sub>TOP</sub>	0.58	0.77	0.53	-0.42	0.61	0.63	-0.08	0.60	0.32	-0.19	1.00		
θ <sub>BASE</sub>	-0.93	-0.80	-0.08	0.79	-0.57	-0.26	0.77	0.08	0.47	0.45	-0.29	1.00	
θ <sub>2M</sub>	-0.66	-0.56	-0.37	0.32	-0.81	0.03	0.73	0.19	0.43	0.29	-0.27	0.66	1.00

There is also similar low-frequency variability between many of the inversion measures.

Correlations of low-frequency subsidence inversion variability for several inversion measures are displayed in Tables 7-6 and 7-7, for Oakland and San Diego, respectively. The low frequency data were obtained by applying a five-year running mean filter through the monthly mean data. This filtering has the effect of reducing the independent number of observations to something on the order of 10 (48 years divided by 5), with correlations greater than 0.59 being significant at the 95% confidence level.

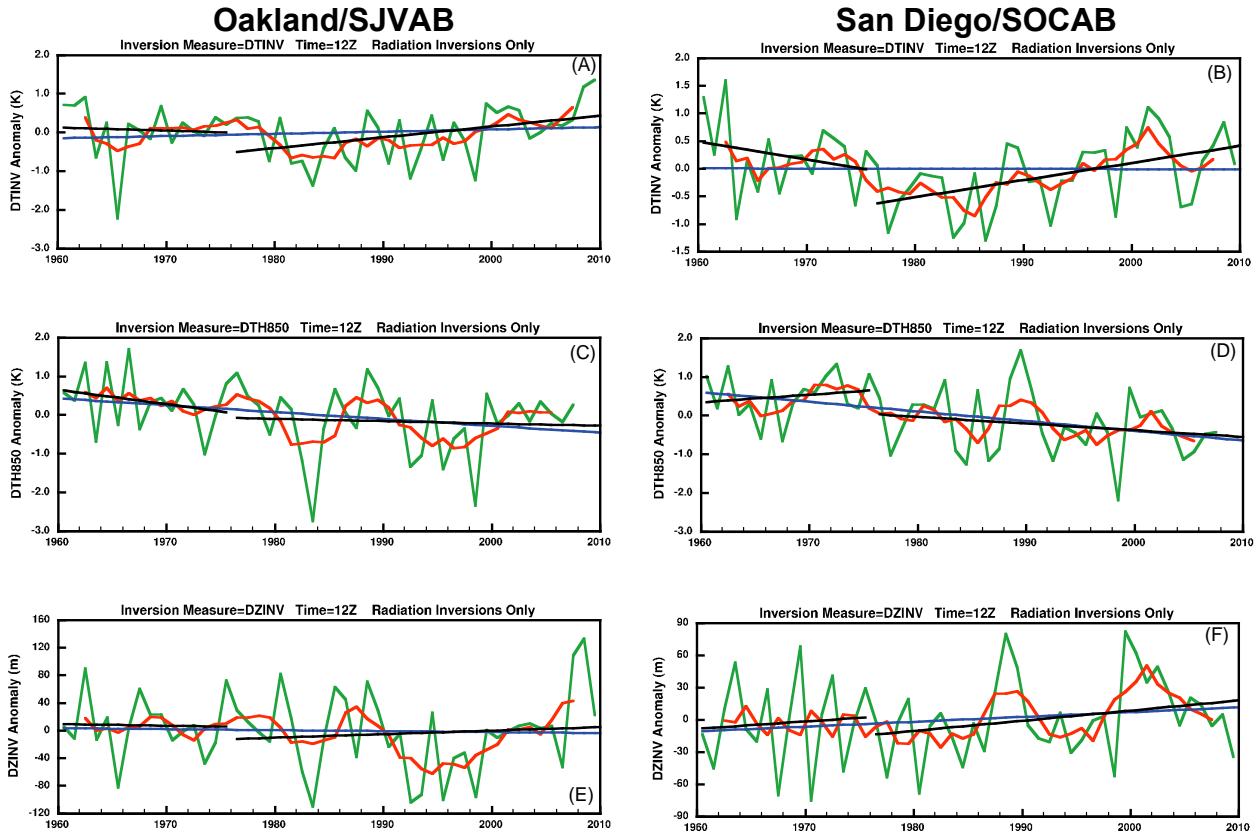
At both Oakland and San Diego, the low frequency variability of  $DT_{INV}$  and  $DZ_{INV}$  are strongly correlated. Similar correlation strengths were found for both sets of inversion measures at the daily and monthly time scales. Interestingly, the correlation between  $DT_{INV}$  and  $T_{BASE}$  is much stronger for low-frequency variability than it is on either daily or monthly time scales at both sites. Conversely, correlations between  $DT_{INV}$  and  $T_{850}$  are much stronger on the daily and monthly time scales. This may imply that changes in surface-based processes over the length of the historical data may play a significant role in the low-frequency variability of  $DT_{INV}$ , while processes in the lower-to-middle atmosphere are more important for the shorter daily and monthly timescales.

Figure 7-3 contains time series of annual mean  $DT_{INV}$  and  $DZ_{INV}$  anomalies for radiation inversions at Oakland and San Diego. Annual means were used rather than monthly means, as there are very few radiation inversions during summer months. Additionally, only data at 12Z is plotted since very few radiation inversions are observed at 00Z (local afternoon). The number of days per year with radiation inversions at 12Z varied from 69 to 159. Similar to subsidence inversions, both the inversion strength  $DT_{INV}$  and inversion depth  $DZ_{INV}$  are decreasing over the 48-year time period examined.

### ***7.2 Time Series of Strong and Weak Inversion Frequency***

The frequency and duration of strong or weak inversion episodes could be an important consideration in air quality and health impacts. Quartile values of inversion strength are determined for each calendar month by sorting all  $DT_{INV}$  values over the 1960–2007 period. In the following analyses, to investigate effects of possible secular changes in the occurrence of strong or weak inversions, the inversion series was first detrended and later, the inversion occurrences were examined from the original (not detrended) series. Linear interpolation between the monthly values was used to calculate daily quartile values for each day of the year (monthly values were placed at midpoint of each month). Strong and weak inversions are defined as in Section 3. The frequency of strong inversions for a given month is the number of days when  $DT_{INV}$  exceeds  $Q_3$  (number of days when  $DT_{INV}$  less than  $Q_1$  for frequency of weak inversions) divided by the total number of days.

## Radiation Inversions



**Figure 7-3.** Time series of annual mean values of  $DT_{INV}$  (a, b),  $D\theta_{850}$  (c, d),  $DZ_{INV}$  (e, f), based on radiosonde data and surface temperature measurements in the San Joaquin Valley ( $D\theta_{850,SJV}$ ) and South Coast ( $D\theta_{850,SC}$ ) Air Basins. The green line shows the annual mean data, while the red line show a five-year running mean. The straight blue lines represent a linear best fit to the data for the entire 1960-2007 period. The straight black lines represent linear fits for the periods 1960-1975 and 1976-2007. The annual means were calculated using only days when radiation inversions were observed at 12Z.

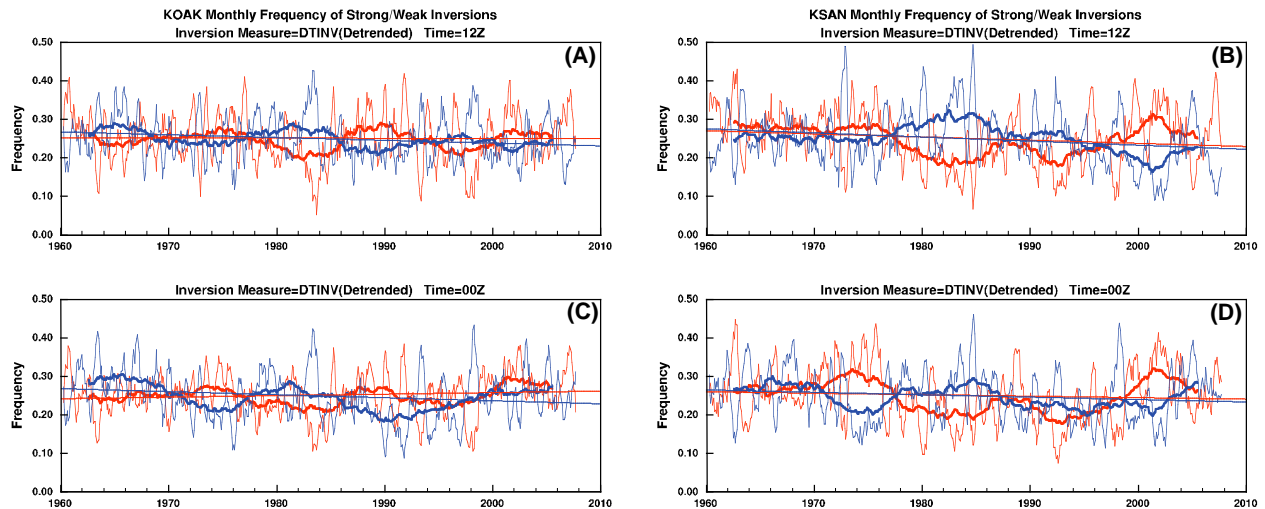


**Figure 7-4.** Time series of monthly frequency of strong and weak inversions at Oakland (a, c) and San Diego (b, d). Red curves show the frequency of strong inversions while the blue curve shows the frequency of weak inversions. The data was smoothed using a six-month running mean (thin lines) and five-year running mean (thick curves) filters. The straight lines represent a linear best fit. Strong inversions are defined when  $DT_{INV}$  exceeds the third quartile and weak inversions are defined when  $DT_{INV}$  is less than the first quartile value. Quartiles were calculated for each calendar month using detrended daily values of  $DT_{INV}$  derived from radiosonde measurements over the 1960–2007 period at each site.

Figure 7-4 contains the time series of monthly frequency of strong and weak inversions at Oakland and San Diego determined from the detrended series of inversion strength. The mean frequency of strong and weak inversions over the entire 48-year period is each 25%. However, values for individual months can vary significantly from this mean value, ranging from 0% to 77% of days within the month. There is also significant interannual and decadal variability in both strong and weak inversion frequency. The high activity inversion epoch from 1973–1977 was a period in which strong inversions occurred, in aggregate over the five-year period, 30% of the time, while the low activity inversion epoch from 1983–1987 was a period when strong inversions occurred only 19% of the time on average over that five-year period. Generally, the frequency of strong inversions varies inversely from that of weak inversions. A noteworthy exception occurred between 1995–2000, when both strong and weak inversion at 00Z increased in frequency at both locations.

Because the  $DT_{INV}$  time series were detrended prior to computing the strong/weak inversion frequencies, long-term trends in inversion strength,  $DT_{INV}$ , have no impact on the occurrence

frequency of strong inversions, shown in Figure 7-4. As a result, any significant long-term trends in Figure 7-4 are due to changes in the shape of the frequency distribution of  $DT_{INV}$ . For example, if the  $DT_{INV}$  frequency distribution became broader (assume equal changes on both sides of the median) over time, this would not change the overall strength of the inversions, but would produce an increase in the frequency of strong/weak inversion occurrences. A change to a more narrow distribution would similarly not change the overall strength but would have the opposite effect in reducing the frequency of strong and weak inversions.

However, there may be long-term trends in  $DT_{INV}$  that would affect the strong/weak inversion frequency. To gauge this impact, the frequency of strong inversions was recalculated using the original non-detrended  $DT_{INV}$  time series, and Table 7-8 shows the number of strong inversion days per year for the first and second half of the 1960–2007 study period. At San Diego, there were about 15-18 fewer strong inversion days per year during the second half of the time period, compared to a long-term average of about 91 strong inversion days per year. The difference at Oakland was not as large, with about 4-7 fewer strong inversion days per year during the second half of the period.

**Table 7-8.** Average number of strong inversion days per year based on time series of  $DT_{INV}$  that was not detrended. Values are given for the first and second half of the period.

	1960–1983	1984–2007
KSAN 12Z	98.1	83.3
KSAN 00Z	99.5	81.5
KOAK 12Z	89.2	85.5
KOAK 00Z	92.5	85.3

Differences in the number of strong inversions are even more apparent when shorter time periods are examined. For example, at San Diego there were on average 110 strong inversions per year during the five-year period 1973–1977. During 1983–1987 there were only 71 strong inversions per year, or a reduction, relative to the high activity 1973–1977 period, of 39 strong inversions per year. These differences illustrate that while there are inversions on most days in California, low-frequency variability in inversion strength (along with other inversion characteristics) is an important feature of the environment.

## 8.0 PROJECTED VARIABILITY OF INVERSION MEASURES FOR 2010-2099 PERIOD

Meteorological patterns play a dominant role in the occurrence and strength of low level inversions and thus the determination of air pollution concentrations in California, as has been demonstrated in the prior Sections. It is expected that climate change will significantly affect meteorological patterns in California over the next several decades. The analysis of the historical structure and variability of low-level inversions, and the regional and hemispheric atmospheric patterns that influence them, can be used to project the frequency and intensity of low level inversions in the next several decades. A range of climate and atmospheric projections, over the 21<sup>st</sup> Century, are available from recent global climate model (GCM) simulations conducted by the IPCC Fourth Assessment by different models using different greenhouse gas emission scenarios. The GCM's used in this report are shown in Table 8-1. In this section an investigation is presented to understand potential changes in factors that would affect low level inversions in California over the next century.

**Table 8-1.** Climate models from the IPCC AR4 used in the present study.

Acronym	Modeling Group	Horizontal Resolution ° lon x ° lat	Number of Vertical Levels
CNRM	Centre National De Recherches Meteorologiques	2.81 x 2.81	45
GFDL	Geophysical Fluid Dynamics Laboratory	2.50 x 2.00	24
MIROC	National Institute for Environmental Studies	2.81 x 2.81	20
MPI	Max Planck Institute	1.88 x 1.88	31
NCARc	National Center for Atmospheric Research	1.41 x 1.41	26
NCARp	National Center for Atmospheric Research	2.81 x 2.81	26

### *8.1 Cluster Analysis*

The analysis in Section 3 showed that strong and weak inversions are associated with distinct large-scale atmospheric circulation patterns. Our goal in the following sections is to use large-scale circulation patterns to predict the strength of the inversion magnitude anomaly. The methodology uses pattern correlations to compare a particular monthly mean field to a group of commonly observed (e.g. in historical reanalysis products) circulation patterns. The pattern correlations along with the variance within each monthly mean circulation field will then be used as predictors in a regression analysis to predict the monthly mean inversion magnitude anomaly.

To find commonly recurring patterns within selected large-scale atmospheric circulation fields (e.g., 500 hPa height) this study employs the method of cluster analysis (Anderberg, 1973). Cluster analysis measures the distance between individual members of a dataset and identifies subgroups where members of the subgroup possess some amount of similarity. The input to the analysis is the monthly mean fields throughout the entire period of interest and the output will be a set of  $N$  patterns (clusters). Once the clusters are defined, an individual monthly mean field can be compared to each of the cluster patterns (e.g. using pattern correlations, RMS differences, etc.). Cluster analysis is a technique often used in the social sciences and has also been employed for a variety of meteorological applications (Fernau and Samson, 1990; Gong and Richman, 1995; Jakob and Tselioudis, 2003; Gordon et al, 2005).

### **8.1.1 Method**

Our technique used to derive the cluster patterns closely follows the k-means method described in Anderberg (1973). The following description of our technique is for the daily 500 hPa height fields, but applies easily to other large-scale fields.

Data from NCEP Reanalysis 1 is used to supply monthly mean 500 hPa anomaly (based on 1960-1999 climatology) fields from 1960-2007 (total of 576 months). From these global fields, only the subset from 30°N-50°N, 90°W-150°W was used in the analysis. The boundaries of the region were chosen to be i) large enough to produce cluster patterns that in general contained both positive and negative anomalies; and ii) small enough to include only large-scale patterns significant to California. These boundaries are a subjective choice, but experiments with larger and smaller subset fields yielded similar overall results.

An outline of the procedure is:

- 1) The clusters are "initialized" by randomly selecting  $N_C$  seed clusters from the 576 available monthly fields (the choice of  $N_C$  is discussed below).
- 2) One at a time, the remaining  $576 - N_C$  clusters are assigned to "closest" of the  $N_C$  seed clusters where RMS differences are used to determine the "distance". Once a monthly

field is assigned to a cluster, the cluster centroid is recalculated, where the centroid is the average over all members of this cluster calculated at each grid point. This updated centroid is then used in the assignment of the next monthly field.

3) Loop through all 576 monthly fields again and find closest cluster. If this is a different cluster than was previously used for the monthly field, then assign this month to the new cluster and recalculate the centroids of the gaining and losing clusters. This step is repeated until convergence (i.e., no change in cluster membership).

4) Once convergence is achieved, there are  $N_C$  clusters each with a population of months. The centroid and variance within each cluster are calculated and saved.

Since the clusters are initiated randomly, a different set of clusters is obtained each time the above procedure is performed. Usually the final cluster patterns are similar from run to run, but occasionally significant differences result. In the current study, the above procedure (steps 1-4) was performed  $N_{RUN}$  times and at the end of each run, the variance within each cluster was computed. An overall variance for each run is found by summing the weighted cluster variances over all  $N_C$  clusters with each cluster variance weighted by the cluster frequency.

$$V_{RUN} = \sum F_i \cdot V_i, \text{ where } i = 1, N_C$$

The value of  $N_{RUN}$  was set to 100 and the run with the lowest value of  $V_{RUN}$  was used to supply the cluster patterns for that variable.

In the above procedure, the number of cluster patterns  $N_C$  is set at the beginning. As the value of  $N_C$  is increased, the difference or distance between the resulting cluster patterns decreases. Thus, the clustering analysis has competing goals, that is to produce the largest number of cluster patterns while keeping the patterns significantly different from each other. To solve this problem, the largest possible value of  $N_C$  was used as long as no two cluster patterns had a pattern correlation of greater than 0.50. While this procedure uses a subjective limit of 0.50, it is

an improvement over some previous studies that used an arbitrary and pre-determined limit for  $N_c$ .

### ***8.1.2 Cluster Patterns for H500 and O700 Monthly Mean Anomalies***

Cluster patterns were calculated for a number of large-scale variables at the 500 hPa and the 700 hPa pressure levels. Results from regression equations predicting inversion magnitude anomalies (described below) showed that the maximum amount of variance was reproduced using monthly mean anomalies of the 500 hPa geopotential height (*H500*) and the 700 hPa vertical velocity (*O700*). Inclusion of other variables did not significantly increase the effectiveness of the regression and were disregarded for computational ease. Our algorithm produced 4 cluster patterns for *H500* anomalies (*H500'*) and 6 cluster patterns for *O700* anomalies (*O700'*).

The resulting four monthly mean *H500'* cluster patterns are shown in Figure 8-1. Also displayed in the figure is the overall frequency of each cluster as well as for the seasonal cycle and for each year in the record (1960-2007). It is worth noting that all four of the derived *H500'* cluster patterns appear as physically realistic and plausible monthly *H500* anomalies.

The lead *H500'* cluster pattern has an overall frequency of 32% (i.e., 32% of the monthly mean anomalies from reanalysis data were assigned to this pattern) and shows a broad area of mild negative height anomalies across most of the domain. This first cluster is moderately more frequent in the warm months and has been decreasing in frequency over the period of record. The second cluster pattern is approximately opposite that of the first and displays a broad area of mild positive height anomalies across the region with an overall frequency of 26% and has been increasing in frequency over the period. The long-term trends in frequency for these first two cluster patterns are consistent with warming temperatures over the 1960-2007 period leading to widespread increases in geopotential heights.

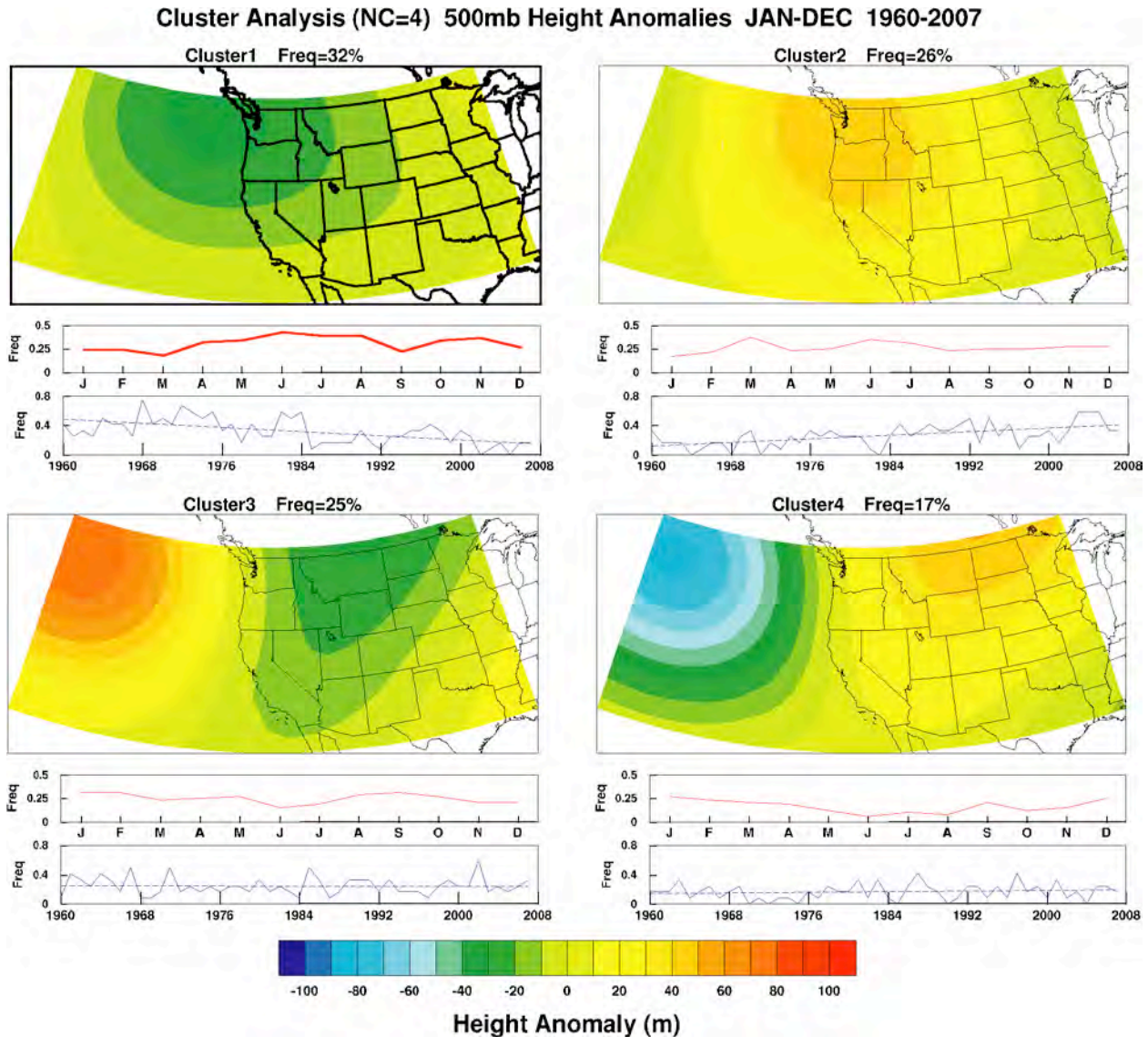


**Figure 8-1.** The four leading cluster patterns of monthly mean 500 hPa geopotential height anomalies for the 1960-2007 period. Also shown for each pattern are the mean annual cycle (red curves) and annual mean time series (solid blue curves) of the frequency of occurrence. The long-term trends are illustrated by the dashed blue lines.

The remaining 2 *H500'* clusters show stronger and less broad anomaly patterns. Cluster 3 contains a region of strongly positive height anomalies over the Northwest Pacific and moderate negative height anomalies over the Western U.S. In cluster 4 there are strong negative height anomalies over the Northwest Pacific and moderate positive height anomalies over the Western U.S. and is nearly opposite that of cluster 3. These last two cluster patterns have frequencies of

25% and 17%, respectively. Cluster 4 appears more frequently in the cold months, while the frequency of cluster 3 does not appear to have much of a seasonal signal. Neither of these last 2 H500 cluster patterns displays any noticeable long-term trends in frequency.

Figure 8-2 displays the six *O700'* cluster patterns and in general have less broad patterns with more spatial variability compared to the *H500'* clusters. The leading *O700'* cluster pattern has a frequency of 39% and consists of relatively small positive and negative anomalies across the entire domain and occurs much more frequently in the warm months. In contrast, the remaining five clusters each have very distinct areas of positive and/or negative anomalies and in general are more frequent during the cooler months. Cluster 2 shows a distinct north-south pattern with strong negative *O700'* values (upward velocity anomalies) over the Pacific Northwest with more moderate positive anomalies over the Southwestern U.S. The frequency of this cluster pattern has decreased somewhat over the 1960-2007 period. Clusters 3 and 4 both show strong positive *O700'* anomalies along the Pacific coast, but differ in the location with the positive anomalies centered over the Pacific Northwest in cluster 3 and further south over California in cluster 4. The frequency of cluster 3 has increased slightly while the frequency of cluster 4 has decreased slightly over the 1960-2007 period.

The last 2 clusters both show strong negative *O700'* values over California, but differ in other regions. Over the Northeastern Pacific, cluster 5 has moderate negative *O700'* anomalies while cluster 6 has strong positive vertical velocity anomalies. In cluster pattern 6, the negative velocity anomalies over California extend further east (compared to cluster 5) and there is a moderate area of positive vertical velocity anomalies centered over southeastern Colorado.

Cluster Analysis (NC=6) 700mb Omega Anomalies JAN-DEC 1960-2007

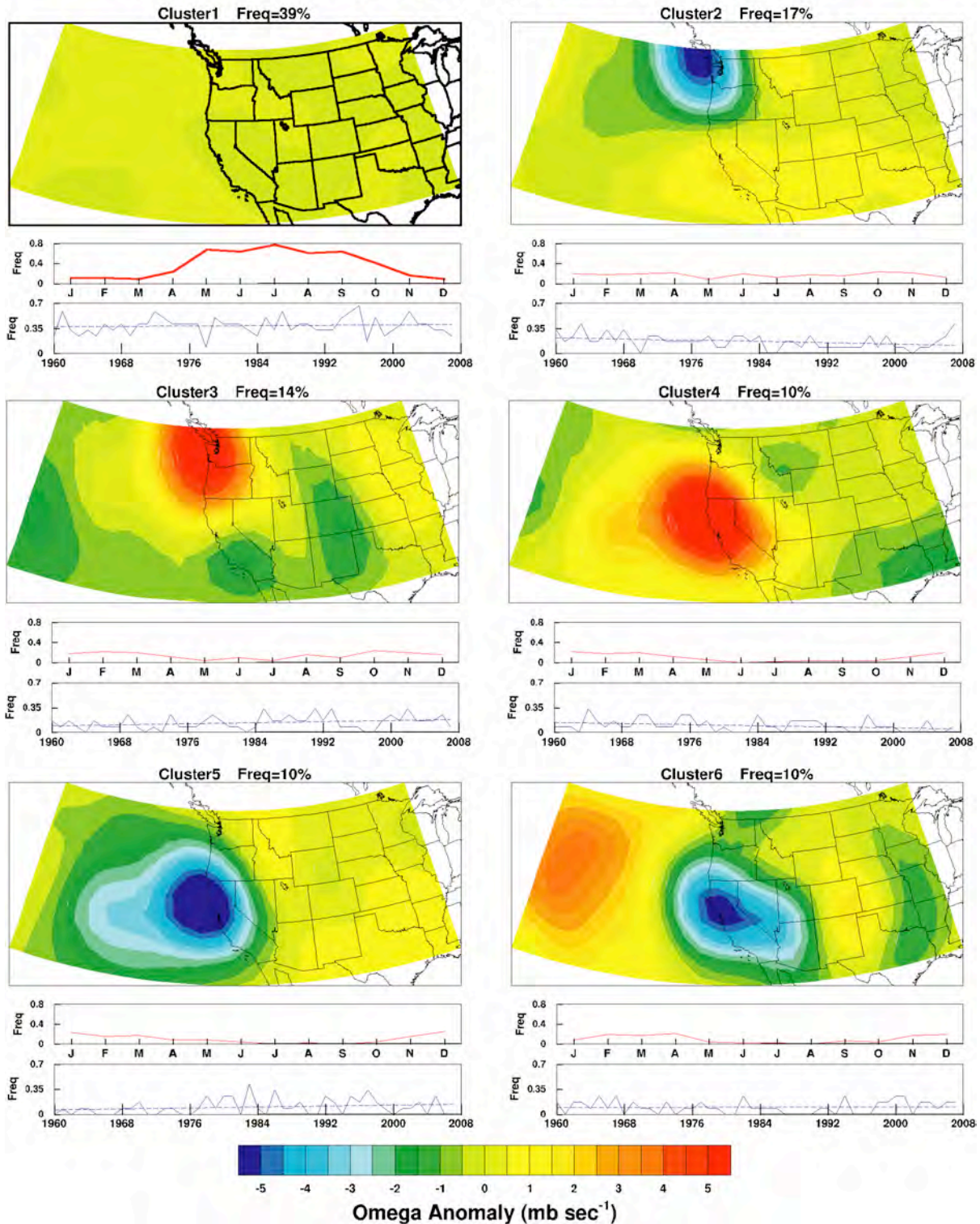


**Figure 8-2.** The six leading cluster patterns of monthly mean 700 hPa vertical velocity anomalies for the 1960-2007 period. Also shown for each pattern are the mean annual cycle (red curves) and annual mean time series (solid blue curves) of the frequency of occurrence. The long-term trends are illustrated by the dashed blue lines.

The cluster patterns in Figures 8-1 and 8-2 represent a set of atmospheric circulation conditions that could affect meteorological patterns over California and will be used together in the following section to derive regression equations predicting the inversion magnitude at both the SJVAB and SOCAB. Prior to deriving the regressions, it is reasonable to ask what is the variability of the inversion magnitude at each site across the individual patterns. In other words, do these patterns represent conditions in which both strongly positive and negative  $D\theta_{850}$  anomalies are likely to be found? Table 8-2 shows the mean value of  $D\theta_{850}$  associated with each of the 10 cluster patterns. These values were calculated by averaging  $D\theta_{850}$  over those months assigned to each cluster pattern during the 1960-2007 period. It is clear from the 10 cluster patterns represent conditions that on average yield both positive and negative inversion magnitude anomaly values. There are also some clusters patterns where the inversion magnitude anomaly is close to zero. Additionally, the anomalies at the two sites differ greatly for the same cluster pattern. For instance,  $O700'$  cluster pattern 3 is associated with moderately strong positive  $D\theta_{850}$  anomalies at the SJVAB and mild-to-moderate negative  $D\theta_{850}$  anomalies at the SOCAB. Overall there appears to be a wide range of anomaly values at both sites which provides confidence that regressions utilizing all the cluster patterns will be able to simulate a significant portion of the  $D\theta_{850}$  anomaly variability.

**Table 8-2.** Mean  $D\theta_{850}$  anomaly values over those months assigned to each  $H500'$  and  $O700'$  cluster pattern. Months assigned to cluster patterns based on NCEP Reanalysis monthly mean fields over the 1960-2007 period. (Units = °C)

	<i>H500'</i> Cluster Patterns				<i>O700'</i> Cluster Patterns					
	1	2	3	4	1	2	3	4	5	6
SJVAB 12Z	-0.98	1.26	0.05	-0.78	-0.09	0.13	0.81	1.94	-1.26	-2.70
SJVAB 00Z	-0.51	0.76	0.01	-0.16	0.00	0.08	0.59	0.67	-0.47	-1.05
SOCAB 12Z	-0.27	0.60	-0.69	-0.26	-0.15	1.00	-0.56	0.39	-0.31	-1.84
SOCAB 00Z	-0.01	0.30	-0.32	-0.01	-0.02	0.32	0.00	-0.47	0.33	-0.36

## 8.2 Regression Models

One goal of this study is to obtain an estimate of how low-level temperature inversions in California may evolve as the climate changes. Currently, large-scale global GCMs are the principle tool for estimating climate change, but these lack sufficient horizontal resolution to

provide meaningful estimates on fine spatial scales needed to resolve California's air basins. Additionally, it is still a research issue to determine whether GCM results downscaled to finer horizontal resolution for regional studies have sufficient model physics to replicate accurately the processes that control near-surface temperatures (e.g., sea/land interface, mountains).

In the following section, regression models are used to estimate low-level temperature inversion magnitude solely from large-scale atmospheric circulation fields. More specifically, monthly fields of *H500'* and *O700'* from NCEP Reanalysis together with the cluster patterns derived above are used to predict the monthly mean inversion magnitude anomaly. The motivation for this is that large-scale fields from GCM studies are expected to be more realistic than near-surface fields due highly variable topography of California.

### 8.2.1 Method

Pattern correlations between NCEP Reanalysis monthly mean *H500'* and *O700'* fields and each of the corresponding cluster patterns are first produced. Pattern correlations are calculated for each month in the record, thus there is an array of pattern correlations NC x 576, where NC=10 (4 for *H500'* and 6 for *O700'*) and 576 months for the 48 years 1960-2007. In this analysis, an "uncentered" correlation statistic (Wigley et al, 2000) is used:

$$R_{UNC} = \frac{\sum (\Delta x \cdot \Delta y)}{N \sqrt{\frac{1}{N} \sum \Delta x^2} \sqrt{\frac{1}{N} \sum \Delta y^2}}$$

instead of the more commonly applied "centered" correlation:

$$R_{CEN} = \frac{\sum ((\Delta x - \overline{\Delta x}) \cdot (\Delta y - \overline{\Delta y}))}{N \sqrt{\frac{1}{N} \sum (\Delta x - \overline{\Delta x})^2} \sqrt{\frac{1}{N} \sum (\Delta y - \overline{\Delta y})^2}},$$

where in our application,  $\Delta x$  and  $\Delta y$  represent the *H500'* (or *O700'*) anomalies from a particular cluster pattern and reanalysis and the summation is over all spatial grid points in the domain.

In later sections, this method will be applied to  $H500$  and  $O700$  anomaly fields from GCM climate projections that generally predict widespread increasing geopotential heights. If for a particular month, a GCM  $H500'$  field is close to uniform across the domain, then the correlation is calculated between this field and one of the cluster patterns that is also close to uniform across the domain. A centered correlation would probably result in a negligible correlation since the mean  $H500$  anomaly is removed leaving essential noise to correlate with the cluster pattern. An uncentered correlation does not remove the mean  $H500$  anomaly and would most likely result in a significant correlation. A comparison of results using each correlation statistic is shown below in Section 8.2.2.

These monthly pattern correlations together with the variance within each monthly mean field are then used as predictors in multiple linear regression analyses to estimate the monthly mean inversion magnitude ( $D\theta_{850}$ ) anomaly. Multiple linear regression analysis determines a linear relationship between independent variables (here the pattern correlations and variances) and the dependent variable (monthly mean inversion magnitude anomaly). The relationship is chosen such that it produces the minimum root mean square (RMS) difference between observed and predicted monthly mean inversion magnitude anomalies. The reader is referred to Wilks (2006) for further information on multiple linear regression analysis. The models used in this study contained a total of 12 predictors (4  $H500'$  correlations, 6  $O700'$  correlations, the  $H500'$  variance and the  $O700'$  variance). The variances of each field ( $V_{H500'}$  and  $V_{O700'}$ ) are also included as predictors to provide a measure of the amplitude of a given pattern which cannot be determined by the pattern correlations alone.

Separate regressions were performed for each location (SJVAB and SOCAB), each sounding time (00Z and 12Z), and each season (DJF, MAM, JJA, and SON). The predicted time series of inversion magnitude anomalies were compared against measured values with the correlations and explained variances reported in Table 8-3.

The highest correlations are found during the winter and spring months while the lowest are usually during summer. Inversion magnitude variability is at a minimum during summer and

this may explain the reduction in predictability during this season. Correlations were also higher at 12Z compared to 00Z, perhaps because daytime (00Z) processes, such as heating and sea breeze influences, controlling the observed inversion structure are more variable than those during the early morning hours (12Z), making the daytime inversion series noisier.

**Table 8-3.** Correlations and explained variance from regressions estimating monthly mean inversion magnitude anomaly.

Site (time)	DJF	MAM	JJA	SON	ANNUAL
SJVAB 12Z	0.89/79%	0.89/80%	0.78/62%	0.84/71%	0.87/75%
SJVAB 00Z	0.69/48%	0.63/39%	0.70/49%	0.69/47%	0.69/47%
SOCAB 12Z	0.80/64%	0.84/71%	0.56/32%	0.69/48%	0.75/56%
SOCAB 00Z	0.67/45%	0.75/56%	0.48/23%	0.52/27%	0.62/39%

In the following sections, these regressions will be applied to GCM climate change projections where tropospheric temperatures and geopotential heights are increasing in time. Can regressions computed during relatively cool months be successively applied to another set of months where the temperatures are generally higher?

To answer this question, another regression was computed to predict the inversion magnitude anomaly at SJVAB at 12Z. This regression was *computed* using only those months where the monthly mean California temperature was below the climatological monthly mean (mean California temperatures obtained from the National Climatic Data Center's U.S. Climate Division Dataset). During the 1960-2007 period there were 287 cold months and 289 warm months using the above definition. The regression was then *applied* to climatologically warm months. The correlation between the predicted time series and measurements was 0.82 during the cold months and 0.79 during the warm months. The similarity in correlations suggests that the regression equations are independent of temperature anomalies.

### 8.2.2 *Uncentered Correlations vs Centered Correlations*

The regression results above used *uncentered* pattern correlations between R1 monthly *H500'* and *O700'* fields and the corresponding cluster patterns as predictands. Another set of regressions was produced using *centered* pattern correlations as predictands to estimate the inversion magnitude anomaly. Figure 8-3 shows a comparison of inversion magnitude

anomalies from observations, the regressions using uncentered pattern correlations, and the regressions using centered pattern correlations. The inversion magnitude anomalies are compared as a function of a normalized mean 500 hPa anomaly ( $\overline{H500'_N}$ ). For each month in the period 1960-1999, a value of  $\overline{H500'_N}$  was calculated,

$$\overline{H500'_N} = \frac{\overline{H500'}}{\sigma_{H500'}},$$

$$\sigma_{H500'} = \sqrt{V_{H500'}}$$

where  $\overline{H500'}$  and is the mean  $H500'$  over the domain. Monthly mean inversion magnitude anomalies from observations and the two sets of regressions are averaged over bins of  $\overline{H500'_N}$ , where the bin widths were selected to insure at least 15 months within each bin.

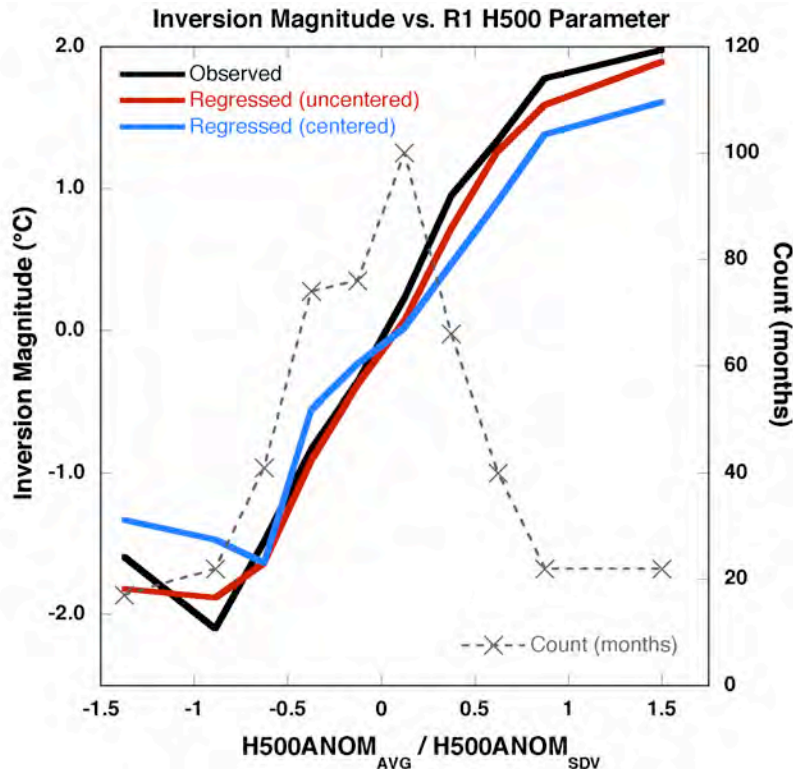


**Figure 8-3.** Comparison of inversion magnitude anomalies from observations (black), regressions using uncentered pattern correlations (red), and regressions using centered pattern correlations (blue) within bins of the normalized mean 500 hPa anomaly. The number of months within each bin is shown by the dashed grey line and the crosses denote the midpoints of each bin.

Regressed estimates of inversion magnitude anomalies using uncentered correlations compare more favorably to observations than those using centered correlations. The differences between the two regressed estimates are most striking at large positive and negative values of  $\overline{H500}'_N$ . Larger absolute values of  $\overline{H500}'_N$  represent those months with large and relatively uniform  $H500$  anomalies across the domain. This illustrates the advantage of using uncentered correlations since for GCM climate projections, the relative population of months within bins with large positive values of  $\overline{H500}'_N$  increases due to increasing temperatures and geopotential heights.

### ***8.3 Regressed Inversion Magnitudes for Historical Period 1960-1999***

The regression models were then applied using monthly mean  $H500$  and  $O700$  anomaly fields from six climate models run over the historical period. The variance over the model  $H500'$  and  $O700'$  fields and the pattern correlations between each field and the corresponding cluster patterns are computed and used as predictors in the regressions to predict 12Z inversion magnitude anomalies at SJVAB and SOCAB. Regressions for 12Z were used due to higher correlations to observations at both SJVAB and SOCAB sites. Separate regressions were used for each season. Table 8-4 shows the inversion magnitude anomaly mean and standard deviation during the 1960-1999 period from each regression. Results from regressions using NCEP Reanalysis  $H500'$  and  $O700'$  fields are also included. The last row in Table 8-4 shows values from radiosonde and surface measurements.

The individual regressions all produce similar overall means and monthly variability (as measured by the standard deviation). Compared to observations regressed inversion magnitude anomalies generally have a slight negative bias and underestimate monthly variability during the 1960-1999 period. The observed seasonal variation of variability and differences between the two sites are well captured by the regressed estimates. Both observed and regressed estimates of monthly mean inversion anomalies display largest variability during winter at the SJVAB and during spring at the SOCAB. The smallest observed variability is in summer at each site and is also well-reproduced by the regression results.

**Table 8-4.** 12Z Inversion magnitude ( $D\theta_{850}$ ) anomaly monthly means and standard deviation of monthly means at SJVAB (top) and SOCAB (bottom) predicted from regressions using monthly mean  $H500$  and  $O700$  anomaly fields from 6 climate models and NCEP Reanalysis1. Also shown are values from observations. Values calculated over the 1960-1999 period. Separate regressions were used for the each season and the annual results are an average over all months.

SJVAB12Z	DJF		MAM		JJA		SON		ANNUAL	
	Avg	$\sigma$	Avg	$\sigma$	Avg	$\sigma$	Avg	$\sigma$	Avg	$\sigma$
MPI	-0.04	2.73	-0.25	1.48	-0.04	1.04	-0.37	1.77	-0.18	1.87
GFDL	0.08	2.66	-0.20	1.39	-0.00	1.11	-0.25	1.87	-0.09	1.86
CNRM	0.04	2.41	-0.06	1.33	0.04	1.00	-0.03	1.45	-0.00	1.64
MIROC	0.18	2.59	-0.19	1.74	-0.06	1.13	-0.13	1.81	-0.05	1.90
NCARc	0.21	2.65	-0.27	1.54	0.05	0.95	-0.46	1.72	-0.12	1.84
NCARp	0.24	2.26	-0.17	1.65	-0.04	1.08	-0.37	1.60	-0.08	1.71
R1	0.13	2.59	-0.22	1.58	-0.08	1.01	-0.19	1.69	-0.09	1.81
OBS	0.00	2.86	0.00	1.83	0.00	1.30	0.00	2.04	0.00	2.09

SOCAB12Z	DJF		MAM		JJA		SON		ANNUAL	
	Avg	$\sigma$	Avg	$\sigma$	Avg	$\sigma$	Avg	$\sigma$	Avg	$\sigma$
MPI	-0.35	1.68	-0.20	1.52	-0.01	1.06	-0.24	1.32	-0.20	1.42
GFDL	-0.18	1.51	-0.16	1.52	0.01	1.25	-0.22	1.38	-0.14	1.42
CNRM	-0.19	1.48	-0.13	1.59	0.23	1.10	-0.02	1.21	-0.03	1.37
MIROC	-0.11	1.66	-0.23	1.81	0.03	1.19	-0.13	1.43	-0.11	1.54
NCARc	-0.21	1.59	-0.21	1.49	0.03	0.90	-0.34	1.33	-0.18	1.36
NCARp	-0.11	1.47	-0.20	1.69	0.06	1.22	-0.34	1.21	-0.15	1.42
R1	-0.07	1.52	-0.21	1.67	-0.07	0.94	-0.23	1.26	-0.14	1.38
OBS	0.00	1.85	0.00	1.97	0.00	1.70	0.00	1.86	0.00	1.84

#### 8.4 Regressed Inversion Magnitudes for Future Period 2010-2099

The seasonal regression models developed earlier are now applied to estimate future trends in inversion magnitude at the SJVAB and SOCAB sites. Pattern correlations between monthly mean  $H500'$  and  $O700'$  fields from the six climate models during the period 2010-2099 and corresponding cluster patterns along with the variance within the model monthly mean  $H500'$  and  $O700'$  fields are used as predictors in the seasonal regression models. Results from climate model results incorporating both A2 and B1 emission scenarios were employed.

Regressed results from each climate model were first averaged over three 30-year periods (2010-2039, 2040-2069, and 2070-2099) and then combined to form an "ensemble" mean for the period (Note: periods start in 2010 as not all models provided data for years 2000-2010). This was done

at each site and for both emission scenarios with the results shown in Figure 8-4. There are individual plots for each season as well as for the combined 12-month annual period. The error bars on each curve represent the standard deviation between 30-year means from the six climate models. Also included on each curve is a point representing regressed results from the six climate models for the 40-year 1960-1999 historical period.

Results from all regressions predict larger inversion magnitudes during the 2010-2099 period relative to the 1960-1999 historical period. There is a generally increasing trend of inversion magnitude at both sites and during all seasons, however the rate of increase tends to slow down, and sometimes levels off, toward the end of modeled period. Estimated increases in inversion magnitude are generally larger with the A2 emission scenario compared to the B1 scenario.

There are some notable differences in the estimated change of inversion magnitude at the two sites, primarily during the DJF and JJA seasons. At the SJVAB, estimated increases in inversion magnitude are largest during DJF and smallest during JJA, while the largest increases at the SOCAB are found during JJA. These differences are in part due to the varied response of inversion magnitude at each site for a given atmospheric circulation pattern. For instance, during months when the atmospheric 500 hPa field (as given by reanalysis) looks most like *H500* cluster pattern 3, inversion magnitude anomalies at SJVAB are minimal, while at SOCAB, there are strong negative anomalies (see Table 8-2). Strong differences in response are also noted for several other cluster patterns. Thus, as certain atmospheric circulation patterns become more/less frequent, the impact on inversion magnitude may differ significantly at the two sites.

The regression estimates of inversion magnitude show increasing trends into the future. After the year 2060 the error bars shown in Figure 8-4 are all above the zero line implying that the estimated changes in inversion magnitude have risen above the natural noise threshold. Another test to address whether the estimated changes are meaningful is to determine when the estimated changes become greater than half of the standard deviation of the historical observed values which is 0.4°C at both the SJVAB and SOCAB. This method also indicates that, based on the regression model estimates, increases in inversion strength become "detectable" by about 2060.

**Inversion Magnitude Anomalies from Seasonal Regressions  
6-Model Means Error Bars = StandDev Between Model Averages**

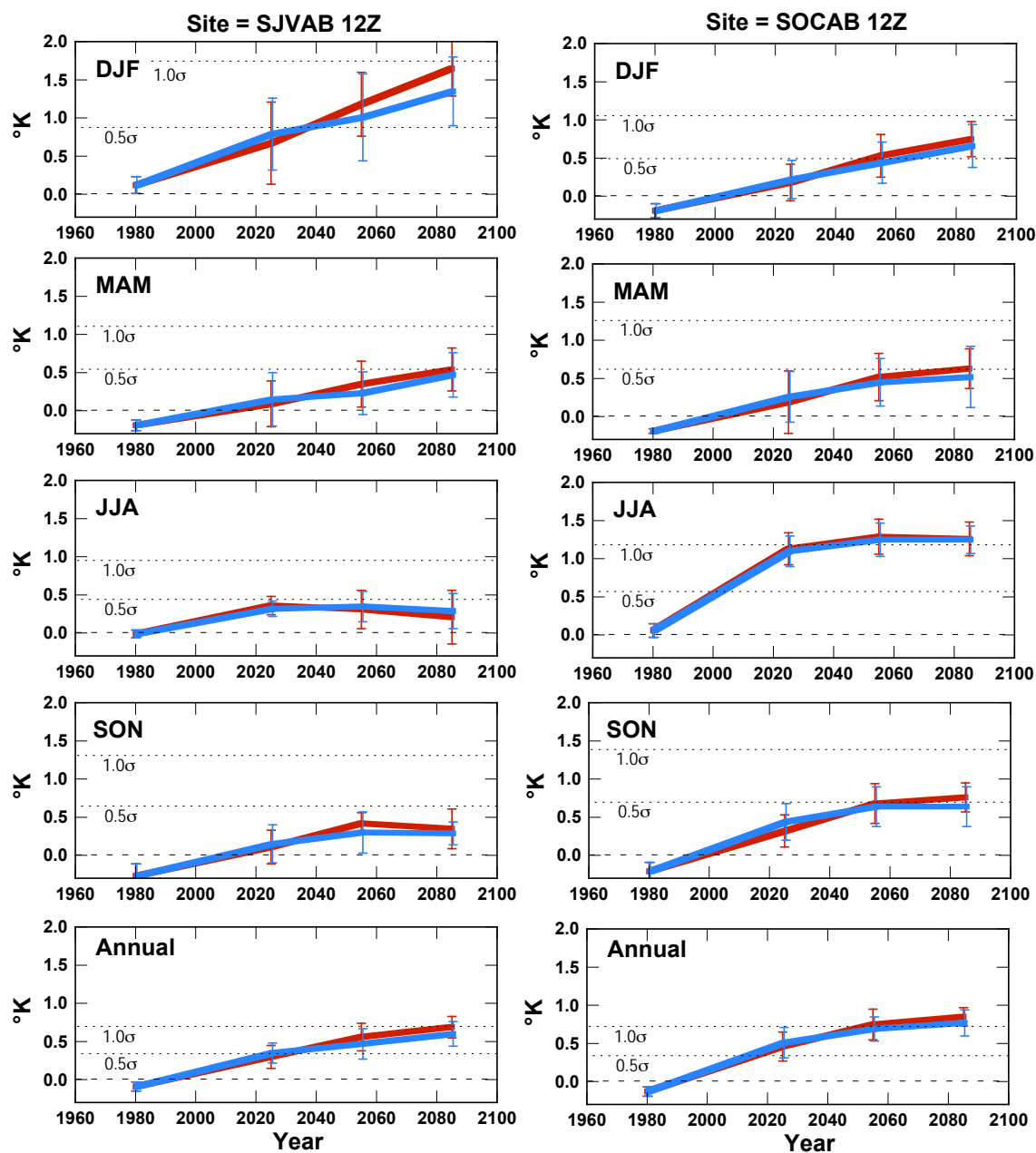


**Figure 8-4.** Future changes in inversion strength based on regression estimates for the San Joaquin Valley (left column) and South Coast (right column) Air Basins for each 3-month season as well as an annual mean. Results shown have been averaged over the six climate models and over a 40-year historical period (1960-1999) and three 30-year future periods. Results are based on the two emission scenarios B1 (blue curves) and A2 (red curves). The error bars on each curve denote the standard deviation between 30-year means from the six climate models within each time period.

As the atmospheric circulation evolves in the climate model projections, the average pattern correlation between the model monthly mean  $H500'$  and  $O700'$  fields and each of the corresponding cluster patterns also changes. The evolution of the average pattern correlation for each cluster pattern is shown in Figure 8-5. The pattern correlations are averaged over the six climate models and three 30-year periods spanning 2010-2099 as well as the 40-year historical period 1960-1999. The variance within the model fields associated with each cluster pattern also changes during this period. Figure 8-6 shows the mean  $V_{H500'}$  and  $V_{O700'}$  over all months assigned to each of the clusters, where each month is assigned to the cluster that yields the largest positive pattern correlation.

During the historical period, all mean pattern correlations between model fields and the cluster patterns are near zero. Subsequent to the historical period, there are significant changes in the mean pattern correlations, with much larger variations for the  $H500'$  cluster patterns compared to the  $O700'$  patterns.

The largest changes are seen in the first two  $H500'$  cluster patterns that represent very spatially broad circulation features. The mean pattern correlation between model fields and the first  $H500'$  cluster pattern becomes strongly negative while the mean correlation associated with the second  $H500'$  pattern becomes strongly positive. The first  $H500'$  pattern contains generally negative height anomalies across the domain while the second is composed of generally positive anomalies and the changes in the mean pattern correlations are consistent with a warming climate and overall larger 500 hPa heights relative to the 1960-1999 base period. The majority of the estimated increase in inversion strength shown in Figure 8-4 is due to increasing positive pattern correlations between climate model fields and  $H500'$  cluster pattern 2.

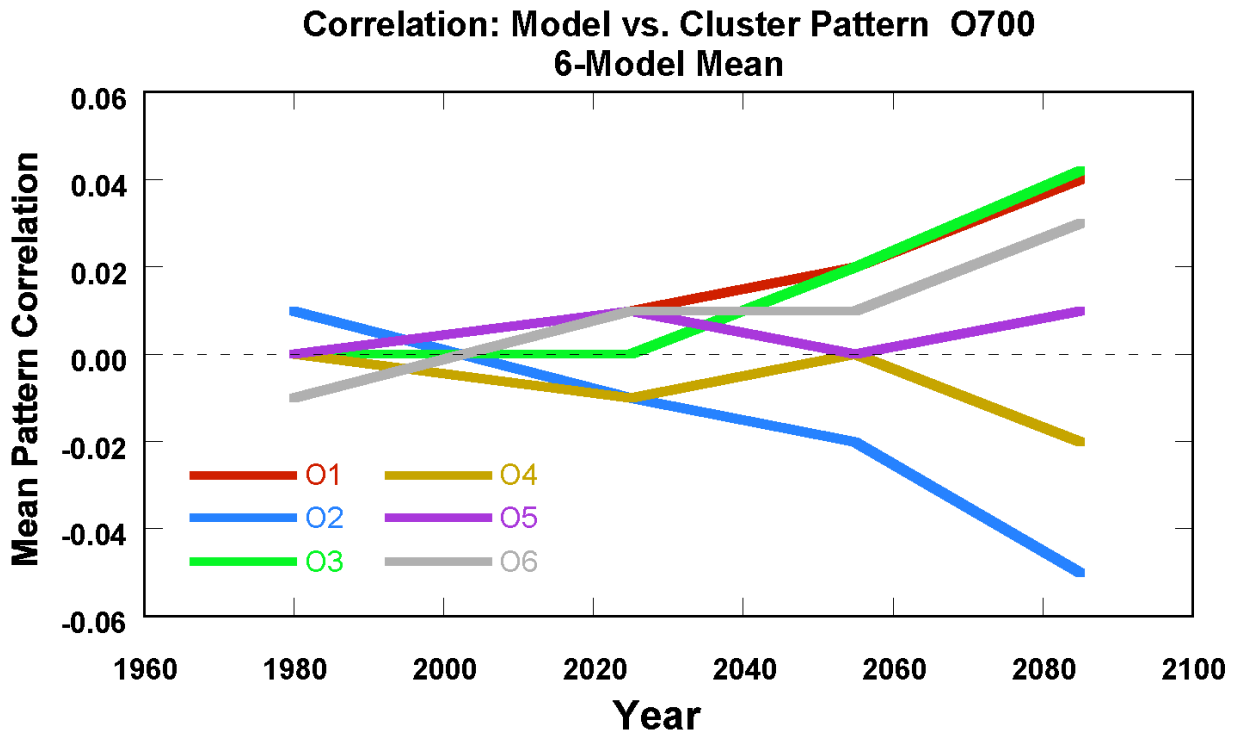
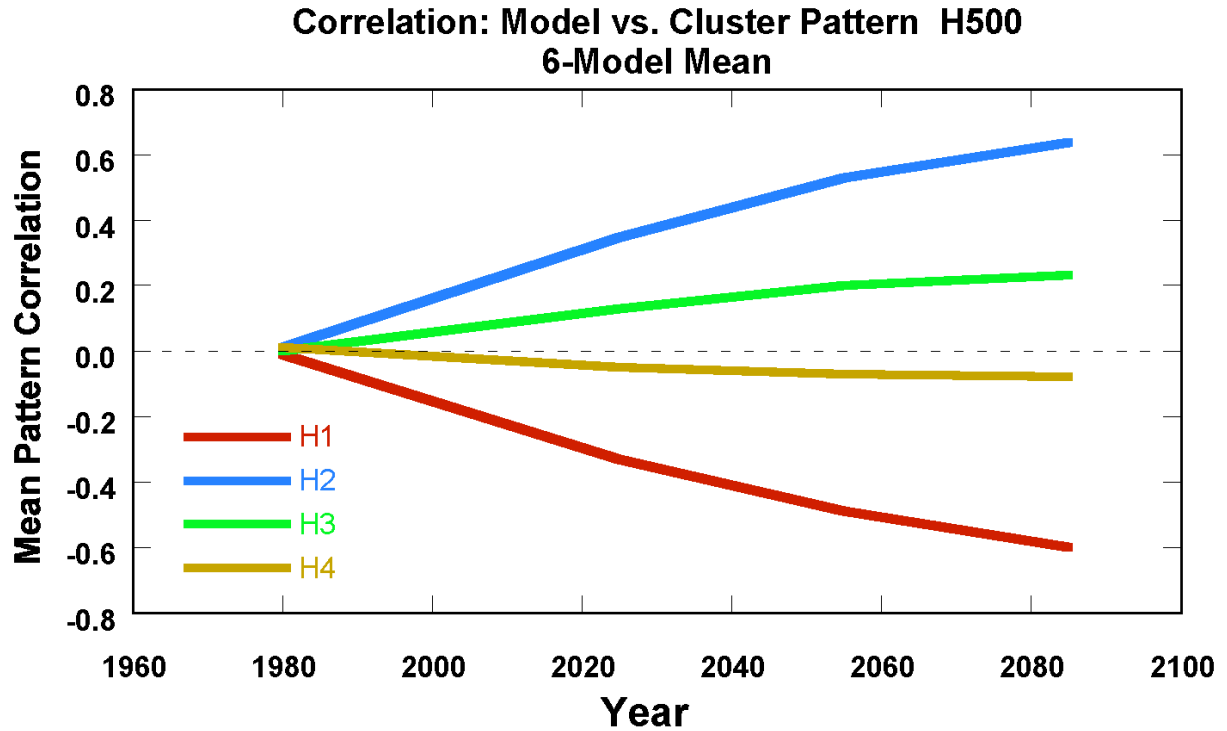


**Figure 8-5.** Evolution of the average pattern correlation between climate model fields and the H500' (top) and O700' (bottom) cluster patterns. The pattern correlations were averaged over the six climate models and three 30-year periods spanning 2010-2099 as well as the 40-year 1960-1999 historical period. Note: the scale of the y-axis variable differs between the two plots.

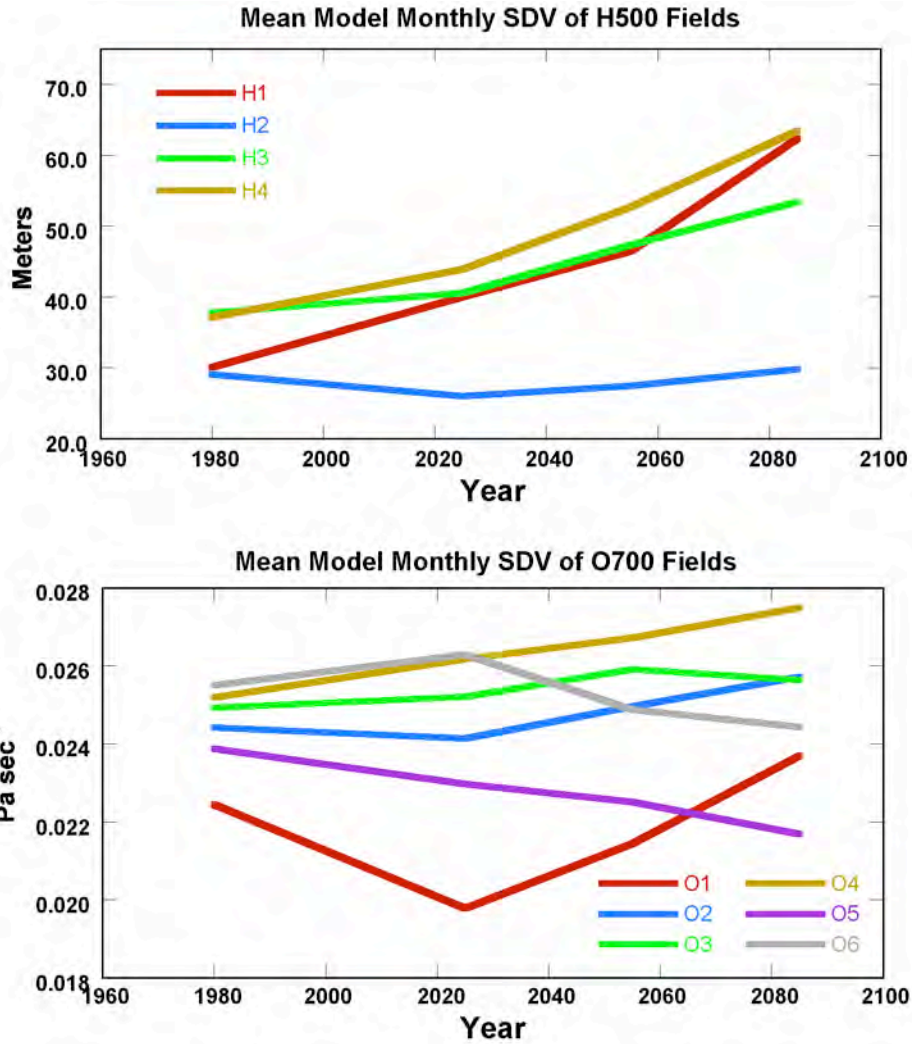


**Figure 8-6.** The average standard deviation within model fields associated with each H500' (top) and O700' (bottom) cluster pattern. The standard deviations were averaged over the six climate models and three 30-year periods spanning 2010-2099 as well as the 40-year 1960-1999 historical period.

The variability of monthly *H500'* fields associated with the first *H500'* cluster increases strongly during the modeled period. The above results imply that over time modeled *H500'* fields become less like *H500'* cluster pattern 1, but when they do, the amplitude of the anomaly pattern is stronger relative to those occurrences in the historical period. In contrast, the variability of monthly *H500'* fields associated with *H500'* cluster pattern 2 remains approximately constant over the model integration period. Thus, the model projections suggest that there will be more months where the *H500'* anomaly field resembles *H500'* cluster 2, but there will not be an appreciable change in the amplitude of the anomaly pattern.

There are smaller but significant changes in the mean pattern correlation between model fields and *H500'* cluster patterns 3 and 4. The mean pattern correlation associated with the third *H500'* cluster pattern becomes more positive in the climate model projections, while correlations with the fourth *H500'* cluster pattern becomes slightly more negative. These last two *H500'* clusters consist of more spatially varying features and may explain the differences in predicted changes in inversion magnitude between the SJVAB and SOCAB sites. The spatial variability of modeled monthly *H500'* fields assigned to these clusters also increases suggesting stronger spatial gradients between regions of anomalously high and low 500 hPa heights.

The increase in mean pattern correlation of *H500'* cluster pattern 3 is particularly interesting. This pattern consists of a trough of low heights over the Western U.S., however the trough is aligned with a southwesterly-to-northeasterly orientation. Due to this orientation, the response of inversion magnitude is quite different in the SJVAB compared to the SOCAB (see Table 8-2). During the historical period, when this *H500'* pattern was prevalent slight positive inversion magnitude anomalies were noted in the SJVAB, however moderate negative inversion magnitude anomalies were observed in the SOCAB. *H500'* cluster pattern 3 is most frequent during the winter months and increases in the pattern correlation between climate model fields and this cluster pattern may help explain the weaker increases in the SOCAB relative to the SJVAB during the winter season (Figure 8-4).

Four of the *O700'* cluster patterns are associated with slightly increasing positive pattern correlations. Interestingly, three of these four cluster patterns have negative anomalies (increasing upward velocities) over the general California region, while the two *O700'* cluster patterns with decreasing pattern correlations (2 and 4) both have positive anomalies (increasing downward velocities) over most of California. However, modeled results averaged together (not shown) indicate no significant changes in the 700 hPa vertical velocity (relative to the 1960-1999 base period) over the California region during the integration period. The lack of any noticeable difference in *O700'* is probably due to the relatively small (perhaps insignificant) changes in the mean pattern correlations and/or spatial variability of the modeled *O700'* fields.

The regressions employed in this study use relationships between monthly mean atmospheric circulation anomaly fields and derived cluster patterns to estimate inversion magnitude. These relationships were formed using data from the historical period. An obvious concern is whether the relationships will hold in a future climate where circulation patterns are most likely to change. One possibility is that the regressions could produce large and unprecedented (positive or negative) anomalies using *H500* and *O700* fields from climate model projections. It is certainly possible that larger anomalies could occur in the future, relative to what is observed presently. However, the prediction of such large anomalies would be probably be beyond the limits of the present scheme and could lead to misleading results. To some extent, the use of pattern correlations to relate the monthly mean circulation anomaly fields to the cluster patterns helps alleviates the possibility of unrealistically large anomalies since the correlations have a finite range from -1 to 1. However, there is no such control on the variance within modeled *H500'* and *O700'* monthly mean fields.

The frequency of monthly mean inversion magnitude anomalies from observations and from the regressed estimates are shown in Figure 8-7. Data from the regressed estimates are shown for both the historical period 1960-1999 and the future period 2010-2099. During the historical period, the frequency of inversion magnitude anomalies from both observations and regressions match fairly well. The distribution of the observed anomalies is slightly wider and is likely due to the regression underestimating extreme events. The range of regressed anomaly estimates during the future period is the same as that during the historical period. The main difference between the estimated anomalies of the two periods is that during the future period there are more positive (and less negative) anomalies compared to the historical period. At no time do the regressed estimates produce extreme or unprecedented inversion magnitude anomalies.

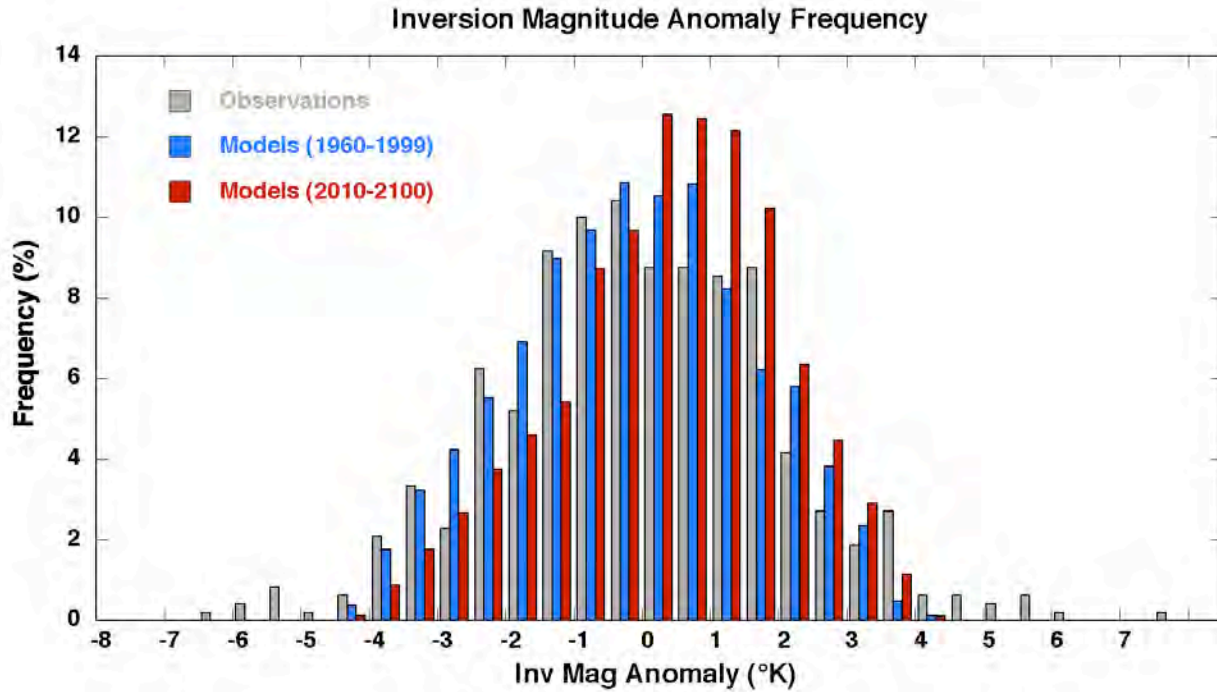


**Figure 8-7.** Frequency of monthly mean inversion magnitude anomalies from observations (grey), and regressed estimates during historical period (blue) and future period (red).

### ***8.5 Inversion Magnitude Projections Directly from Climate Models***

Future trends in inversion magnitude, as measured by  $D\theta_{850}$ , can also be estimated directly from the results of the climate model projections of  $\theta_{850}$  and near-surface temperature. As noted earlier, these direct model estimates are probably representative of a much broader area than individual air basins in California due to relatively coarse horizontal resolution. Additionally, limitations and approximations in model physics may also lead to further uncertainty in the estimates. Nonetheless, a comparison of results obtained from the regression analysis to direct estimates from climate models will allow us to more accurately gauge confidence in the estimated trends.

Future trends in the inversion magnitude anomaly as computed directly from the six climate model projections are shown in Figure 8-8. As before, results from the climate models are averaged over the 40-year historical period 1960-1999 and three 30-year periods spanning 2010-2099. Error bars on the curves denote the standard deviation between the individual model

estimates. The estimated trends for both the A2 and B1 emission scenarios are presented for each season as well as the 12-month annual mean.

The direct model estimates of inversion magnitude show increasing trends in all seasons and at both sites, similar to trends found via the regressions, albeit the trends are not as strong as those found using the regressions and there is not as much variation in trends between the seasons. Also, the rate of increase appears to increase slightly towards the end of the 2010-2099 period in contrast to a leveling off found in the regressed estimates. The direct model estimates also indicate that the increasing trends are stronger at the SOCAB in all seasons relative to the SJVBA.

**Inversion Magnitude Anomalies Directly from Climate Models**  
**6-Model Means Error Bars = Standard Deviation Between Model Averages**

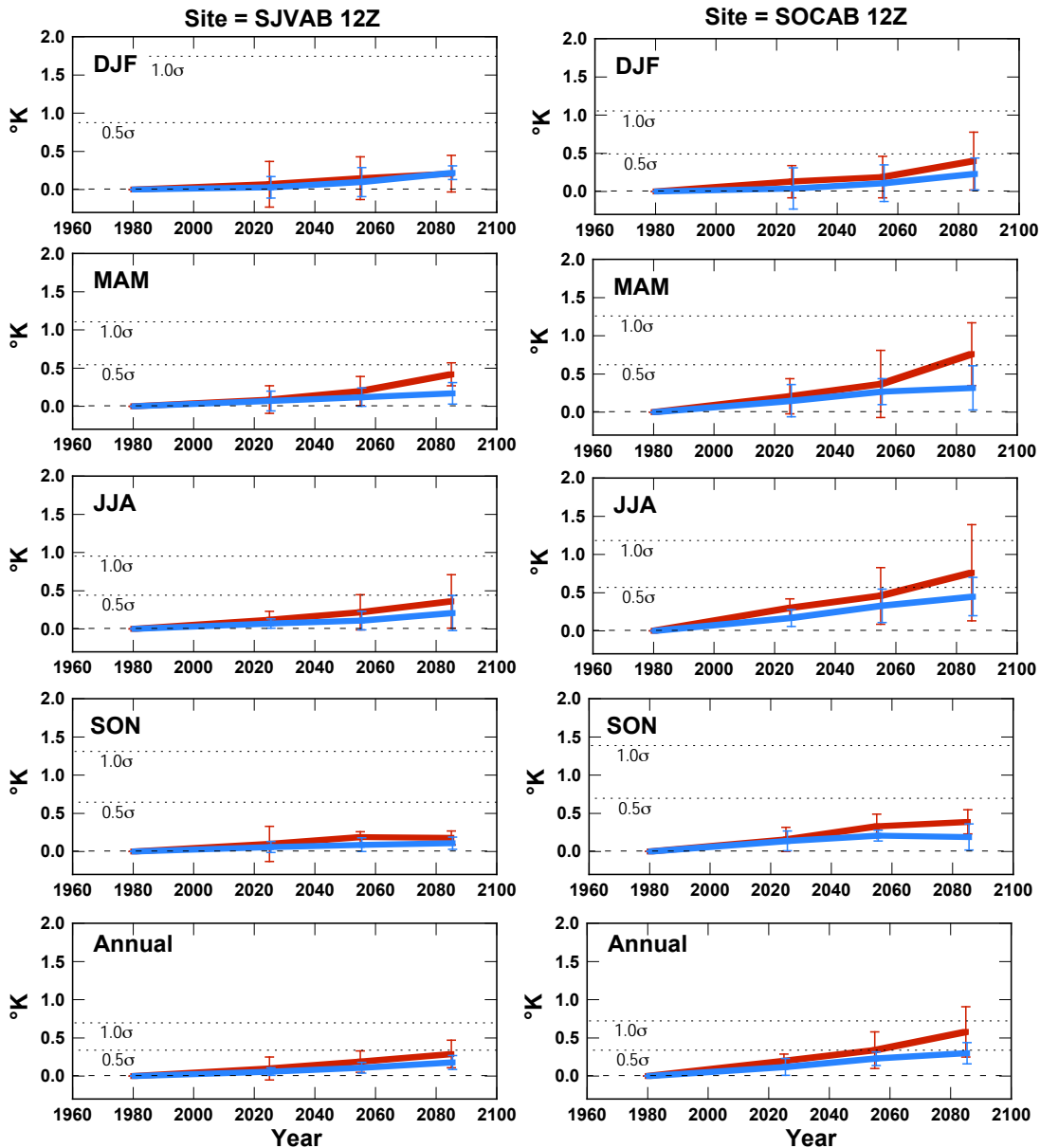


**Figure 8-8.** Future changes in inversion strength based on direct model estimates for the San Joaquin Valley (left column) and South Coast (right column) Air Basins for each 3-month season as well as an annual mean. Results shown have been averaged over the six climate models and over a 40-year historical period (1960-1999) and three 30-year future periods. The error bars on each curve denote the standard deviation between 30-year means from the six climate models within each time period.

## **9.0 CONCLUSIONS**

From five decades of radiosonde records at Oakland and San Diego and associated observational data, the structure, variability and persistence of low-level temperature inversions in California were considered. Additionally, links between inversion characteristics and large-scale atmospheric circulation patterns were investigated. Finally, projections of future inversion strength at the San Joaquin Valley and South Coast Air Basins were produced using relationships between large-scale circulation patterns and monthly mean inversion strength derived from historical data. A more in-depth summary of the research contained in this report is provided in the following sections.

One of the limitations of this work is the lack of long-term observed vertical air profiles within the air basins of interest. Routine radiosonde locations in California are located only at coastal sites. This necessitated combining upper-air temperature measurements from the radiosondes with near-surface temperatures from available stations within the air basins to calculate an inversion measure  $Dq850$  applicable to the air basins. Additionally, the lack of high-quality long-term surface temperature measurements within individual air basins also limits the characterization of inversions within an air basin to a basin-wide average.

This study also combined subsidence and marine air inversions into a single category. Subsidence inversions are relatively large-scale features which would not be expected to display much variability on length scales of the air basins. However, marine air inversions are generally limited to coastal areas and some inland valley sites and this can create large differences in inversion structure within an individual air basin. This study does not resolve any differences across individual air basins.

### ***9.1 Inversion Climatology and Characteristics***

The California locale, under the influence of the subsiding North Pacific High air mass, is a productive environment for low-level inversions. Low-level inversions are nearly ubiquitous, with some form of low-level inversion nearly always present at both Oakland and San Diego. Two measures of inversions, one directly from radiosonde profiles and one from radiosonde upper air temperature combined with surface temperature observations, provide a consistent

picture of the nature of inversions in the region. On average, inversions are strongest and most frequent in summer. They are still often present in winter, although on average not as strong or as frequently occurring. Shallow (base < 50 m) radiation inversions occur at night about 30%–40% of the time and generally break down during the day (often morning). During the day, deeper subsidence inversions were found about 60%–70% of the time during winter, while in summer they were present in some form on almost all days (> 99%).

Subsidence inversions vary in several important ways, including altitude of base and top, their thickness ( $DZ_{INV}$ ), and the strength of temperature difference across the inversion ( $DT_{INV}$ ). Most inversion measures, including  $DZ_{INV}$  and  $DT_{INV}$  possess a strong seasonal cycle, in both magnitude and variability.

Variations in the frequency of inversion strength are quite strong – a high inversion month may have up to 24 days with strong inversions, while a low inversion month might not have any strong inversion days. The temperature change within the inversion during strong inversion episodes is markedly larger than that when weak inversions prevail—the temperature difference ( $DT_{INV}=T_{TOP}-T_{BASE}$ ) during strong inversions at San Diego typically exceeds 10°C (18°F) in summer and 7.5°C (13.5°F) in winter, while during weak inversions it is typically less than 6°C (10.8°F) in summer and 2.5°C (4.5°F) in winter. Strong inversions (defined as within the upper quartile) are usually thicker, with an average inversion thickness of 610 m in summer and 370 m in winter. Weak inversions (lower quartile) are usually thinner, with an average inversion thickness of 420 m in summer and 180 m in winter. Comparable differences are found at Oakland. These variations create conditions more or less susceptible to bad air quality in California’s problem air basins. For example, the monthly frequency of strong inversions at San Diego is correlated with monthly fluctuations in ozone concentration at  $R=0.42$ , and with monthly fluctuations in sulfate particulate matter at  $R=0.61$  (both of these correlations exceed the 99% confidence level).

## ***9.2 Influence of Large-Scale Circulation and Sea Surface Temperature***

The spatial coherence of the strength and other properties of low-level inversions in California air basins is quite strongly determined by larger-scale atmospheric circulation pattern. Strong

inversions result when anomalously high pressure is present over California, while anomalously low pressure is associated with weak inversions. The location of the center of these anomalous pressure systems may have important regional implications as well; strong/weak inversions at a particular location appear more likely when the pressure center is not directly overhead (i.e., the sounding location is on the flank of a nearby anomalously high or low pressure).

At sub-seasonal time scales, of the variables considered in this study, the one exhibiting the closest association to the strength of temperature inversions is the 850 hPa temperature. This association appears in spite of the fact that surface temperature changes generally co-vary with 850 hPa temperature fluctuations and thus act to mute inversion strength. Variations in 850 hPa temperature are dominated by variations in vertical and horizontal temperature advection, as discussed in Section 5.1. Specifically, 850 hPa temperature increases when warm vertical temperature advection outweighs cold horizontal temperature advection. This usually is caused by an increase in subsidence, but a weakening of cold horizontal advection also contributes. At seasonal and longer time scales, surface and radiative processes may contribute more strongly to changes in inversion strength.

While there are inversions of varying intensity and structure on most days in California, low-frequency variability in inversion strength (along with other inversion characteristics) is a feature of the historical record that may have important implications for future changes. The frequency of occurrence of strong inversions varies on interannual to decadal time scales. For example, at San Diego there were periods of high activity during 1973–1977 with 110 strong inversions per year and periods of low activity during 1983–1987 with only 71 strong inversions per year. This variability is associated, to some extent, with the variability of sea surface temperature (SST) along the California coast, in the sense that periods with warmer than average SST tend to have weaker, thinner inversions and periods with cooler SST tend to have stronger, thicker inversions, as described in Section 5.2. The composite geopotential height anomalies for strong and weak inversions quite clearly indicate that the inversion structure is driving the same changes in atmospheric circulation and synoptic patterns that characterize these warm or cool ocean spells. These links to SST carry through to interannual and interdecadal time scales, with consistent links to the El Niño/Southern Oscillation (ENSO) and to the Pacific Decadal Oscillation (PDO).

The warm and cool phases, respectively, of ENSO and PDO feature somewhat similar patterns of SST along the California coast, with the warm phases tending to have anomalously warm SST along the California coast, and vice versa for the cool phases. There is a weak association to ENSO, in the sense that warm ENSO events tend to produce fewer strong inversions. Over decadal time scales, the structure of inversions in California is linked to the Pacific Decadal Oscillation (PDO), wherein stronger and thicker inversions occur with the cool phase (relatively cool SST in the eastern Pacific off North America) of the PDO, and vice versa. The correlations between inversion measures and the PDO are stronger at San Diego than at Oakland.

### ***9.3 Inversion Persistence***

Strong or weak inversions tend to occur in spells, 73% of the strong inversions at the two primary locations (San Diego and Oakland) occurred during spells of two days or longer. These multi-day episodes are set up by larger-scale atmospheric conditions. Strong and weak inversion situations tend to persist longer than do moderate inversions, presumably in response to the lifecycle of synoptic patterns and possibly also affected by persistent influences from the Earth's surface.

The onset of persistent inversion episodes are associated with increasing positive geopotential height anomalies over the Pacific coast along with increasing negative height anomalies over eastern U.S. This "bipole" of high and low height anomalies is important as the increasing horizontal gradient of geopotential heights helps create downward vertical velocities over the region of positive height anomalies that are an important factor in the formation and maintenance of low-level temperature inversions.

Composites of mid-tropospheric geopotential heights indicate that a high amplitude wave train from the western North Pacific across to eastern U.S. creates blocking mechanisms that are responsible for "holding" these height anomaly patterns in place. The stationary nature of this wave train allows persistent inversion episodes of 5 days or more to develop. These episodes occur in both summer and winter. As these persistent inversion episodes break down, the area of positive height anomalies decrease and progress eastward in winter. However during summer, the composites indicate that the area of positive height anomalies tend to retrograde toward the

west as the strong inversion episodes break down. This difference is most likely due to the stronger mid-latitude westerlies and more active storm track over California during winter. During summer, the mid-latitude storm track is usually stationed consistently poleward of California and would not have as much impact on the advection of these height anomalies.

Positive geopotential height anomalies are only one part of the complex structure that builds up during persistent inversion episodes along the California coastal region. Persistent episodes at Oakland do not begin until there is substantial onshore advection of marine air onto the coastal region through a sea-breeze circulation. At San Diego, the start of persistent episodes is also marked by an increase in cool moist air near the surface, but the strength of the sea breeze circulation does not appear as strong as at the Oakland location.

Most climate model projections suggest that the inland - coastal temperature contrast will increase as global temperatures rise (Cayan et al, 2009). This increased temperature contrast would magnify the onshore pressure gradient that normally occurs along the California coastline during summer months leading to an increase in the strength of the sea-breeze circulation. The historical evidence shown here suggests that an increased sea-breeze circulation could lead to an increase in the magnitude and frequency of persistent inversion episodes in the California coastal region in the future.

#### ***9.4 Temporal Variability of Inversion Measures during Historical Period***

There are intriguing long period changes in the inversion structure—the radiosonde records and associated observational data reveal a rich set of interlinked changes between the 1960s and now:

- Subsidence inversion top heights have risen over time by about 0–50 m.
- Subsidence inversion base heights have risen by about 20–100 m.
- Subsidence inversion base temperatures of have risen over time approximately 0.9°C–1.1°C.
- Subsidence inversion top temperatures have also risen, but not as much as the inversion base temperature.

- Overall subsidence inversion strengths, as measured by the  $T_{\text{TOP}}$  minus  $T_{\text{BASE}}$ , have decreased by  $0.4^{\circ}\text{C}$ – $0.5^{\circ}\text{C}$ , amounting to declines of about 6%–14% at Oakland and San Diego.
- Lapse rates of the overlying lower-middle troposphere have increased (more stable).
- The number of days with strong inversions have declined, amounting to about a 6% decrease at Oakland and about a 20% decrease at San Diego.

However, within the 1960-2007 historical radiosonde data record, there appears to be a noticeable shift in many measured inversion characteristics at both Oakland and San Diego during the mid-1970s that may be associated with the PDO-related climate shift that occurred at approximately the same time. After the mid-1970s, inversion magnitude ( $DT_{\text{INV}}$ ) exhibits an increasing trend while the decreasing trend in inversion thickness ( $DZ_{\text{INV}}$ ) is reduced at both locations. This shift during the mid-1970s makes it more difficult to interpret any trends in inversion characteristics during the historical period.

It is also possible that the changes in inversion structure and  $DT_{\text{INV}}$  and  $D\theta_{850}$  inversion strength measures may have been affected by instrumental changes in radiosondes or by changes in the processing and sampling of the radiosondes over the period of record. Changes in surface conditions or surface temperature sampling could also introduce spurious changes in inversion characteristics. However, a number of analyses of the primary radiosonde records at San Diego and Oakland indicate that the changes in frequency, strength and vertical structure of inversions cannot be attributed solely to instrumental or data processing changes. Besides the evidence presented, a number of additional analyses (not shown here) were conducted. In these new additional tests, the radiosonde observations were re-sampled at a lesser number of standard levels in order to remove possible effects from changes in the vertical resolution of the temperature profile. The additional results confirmed the original findings—they yielded, qualitatively, the same trends that were obtained from the original radiosonde observations. Nonetheless, additional work is needed to address the uncertainties in these trends to determine more definitively if they have been affected by procedural or instrumentation changes in the radiosonde record.

Three adjusted radiosonde data sets with independent methods for correcting inhomogeneities produced decreasing trends in  $D\theta_{850,SC}$  that are close to the value of the decreasing trend in the original data. Trends for Oakland and the SJVAB are more uncertain, however, since the two available adjusted radiosonde data sets produce trends that are respectively more positive and more negative than the original trend. They indicate that the wintertime  $D\theta_{850,SJV}$  trend was near-zero or decreasing, and that the summertime  $D\theta_{850,SJV}$  trend that was near-zero or increasing. Our present conclusion that there is a substantial portion of the changes in inversions characteristics is that are not simply artifacts of changes in measurement and data processing. If this is the case, these changes are likely related to change in processes that are associated with larger-scale atmospheric circulation changes—this is evidenced by commensurate trends of the temperature and the height of the top of the inversion. However, there have also been important trends at the base of the inversion—warmer temperatures and higher inversion base—that are linked to changes in surface temperature and possibly other surface characteristics. Novakov et al. (2008) suggest that a decrease in black carbon aerosol concentrations since 1990 have led to increased surface temperatures by allowing more solar radiation to be transmitted through the atmosphere to be absorbed at the surface. The surface temperature increase combined with reduced solar absorption in the atmosphere would, if occurring above the boundary layer, act to weaken temperature inversions. Whether these are predominately effects of changes in larger-scale atmospheric circulation or whether they are also affected by local surface influences that affect the temperature near the surface and the flux of heat and other properties into the boundary layer is still not understood. More work is needed to understand how these processes have affected, historically, low-level temperature inversions in California. Because these processes may change as climate changes, it is important to understand them in order to better understand if they could alter inversion structure or occurrences in the future.

### ***9.5 Projected Changes in Inversion Strength during 2010-2099 Period.***

Direct estimates of inversion magnitude from the climate model output show increasing trends in all seasons and at both sites. This result is reinforced by the finding that similar trends are obtained using statistical regressions from a set of salient circulation patterns. The trends obtained directly from the climate models are not as strong as those found using the regressions and from the direct estimates there is not as much variation in trends between the seasons. The

rate of increase from the direct model-derived estimates appears to increase slightly towards the end of the 2010-2099 period in contrast to a leveling off found in the regressed estimates. The direct model estimates also indicate that the increasing trends are stronger at the South Coast Air Basin in all seasons relative to the San Joaquin Valley Air Basin.

The average pattern correlations between climate model fields and the various cluster patterns displayed significant changes during the 2010-2099 period (Figure 8-5). In general, those cluster patterns associated with positive inversion magnitude anomalies in the SJVAB and SOCAB showed increasingly positive pattern correlations. Significant changes in the average pattern correlation were also noted for some cluster patterns that have different impact on the inversion magnitude anomalies in the SJVAB and SOCAB and helps explain the variability in the projected inversion magnitude at these two locations.

The increasing trends in inversion strength shown by the regressions are mostly due to increasing frequency of large-scale positive height anomalies centered over the Pacific coast, the large scale pattern which has historically explained the largest fraction of the variability of inversion strength ( $D\theta_{850}$ ).

This cluster pattern is similar to patterns associated with persistent strong inversion episodes (Figures 6-2 and 6-3). The increased likelihood of strong positive height anomalies over the Pacific coast would imply an increase in pollution within both the San Joaquin and South Coast Air Basins (Section 4-5). The magnitude of the increase in  $D\theta_{850}$  during the 2070-2099 period (relative to the historical period) from the direct model estimates range from 0.11°C to 0.42°C in the SJVAB and 0.19°C to 0.76°C for the SOCAB, while the regressions estimate increases of 0.21 to 1.65°C for the SJVAB and 0.52 to 1.26°C for the SOCAB. Based on the regression estimates, the increase in inversion strength rises above the natural variability and becomes detectable around the year 2060.

The uncertainty in the regression estimates can be broken into two parts: uncertainty related to the statistical regression model and uncertainty related to the variation in the various climate model projections. A relatively simple measure of uncertainty in the regression model can be

constructed by examining the results during the 1960-1999 historical period shown in Table 8-4. When the regression model is applied using the *H500'* and *O700'* fields from NCEP Reanalysis the average estimated inversion magnitude anomaly over the 1960-1999 period varies from -0.2 to 0.2°C which represents the average error as the observed anomaly is 0 by definition.

The model ensemble mean projected trends in inversion magnitude were shown in Figure 8-4. There was considerable variation between individual model projected trends as indicated by the error bars in Figure 8-4. However, all individual model projected trends indicated an increasing trend in the annual mean inversion magnitude over the 2010-2099 period. For seasonal means, increasing inversion magnitudes were projected by 45 of the 48 individual model trends (48 = 6 models \* 2 scenarios \* 4 seasons) for the SJVAB. At the SOCAB, 47 of the 48 individual model estimates projected increasing trends in inversion magnitude. The individual model projections varied by about +/- 0.4°C about the ensemble mean at both SJVAB and SOCAB. A conservative estimate of the combined uncertainty due to both the regression model and the climate models is on the order of +/- 0.6°C.

### ***9.6 Recommendations for Future Work***

- Continued work to evaluate high resolution dynamical model performance in simulating the structure of low level inversions in coastal and inland valley air basins in California. Along with this evaluation, use models to study processes and variability of inversion characteristics. IN particular, Single-Column Models (SCMs) could be employed to estimate inversions within California's air basins, but require forcing derived from observations or models that have a fine enough horizontal resolution to investigate the individual South Coast and San Joaquin Valley air basins.
- Future work should aim to distinguish between subsidence inversions and marine-air inversions as it is likely that future trends in these individual inversion types may vary for a given air basin. Since marine-air inversions exhibit strong variability across individual air-basins, changes in this type of inversion could lead to strong changes in the variability of inversions across an air basin. The use of relatively new RWP/RASS sites within the air basins could help with this effort.

- Investigate other sources (than radiosondes) of vertical temperature observations, including aircraft temperature observations and Radio Acoustic Sounding System (RASS) atmospheric profilers as a source of information on the variability of inversion structure.
- Examining coastal-inland temperature gradients on historical time scales could be used together with large-scale circulation features to better understand inversion behavior due both marine-air advection and subsidence processes.
- The climate model projections used in this report were only available as monthly mean fields. It would be advantageous to use projected daily mean fields in order to derive estimates on variability and persistence of strong inversion events.
- Evaluation of climate model projections should continue. This will be made possible with the development of the IPCC 5<sup>th</sup> Assessment and other climate change investigation which will provide improved model simulations, including higher resolution and more realistic physical representations.

## REFERENCES

- Anderberg, M. R., 1973. Cluster analysis for applications, Academic Press, New York, 359pp.
- Aw J., and M. J. Kleeman, 2003. "Evaluating the first-order effect of intraannual temperature variability on urban air pollution." *J. Geophys. Res.*, 108, doi:10.1029/2002JD002688.
- Bonfils, C., P. Duffy, B. Santer, T. Wigley, D. B. Lobell, T. J. Phillips, and C. Doutriaux. 2007. "Identification of external influences on temperatures in California." *Clim. Ch.* 87:43–55.
- Dabdub, D., L. L. DeHaan, and J. H. Seinfeld. 1999. "Analysis of ozone in the San Joaquin Valley of California." *Atmos. Environ.* 33:2501–2514.
- Cayan, D. R., M. Tyree, M. Dettinger, H. Hidalgo, T. Das, E. Maurer, P. Bromirski, N. Graham, and R. Flick, 2009. "Climate change scenarios and sea level rise estimates for the California 2009 Climate Change Scenarios Assessment. *California Climate Change Center*, publication #CEC-500-2009-014-F, 64 pages.
- Cayan, D.R., E.P. Maurer, M.D. Dettinger, M. Tyree and K. Hayhoe, 2008: Climate Change Scenarios for the California Region. *Climatic Change*, published online, 26 Jan 2008, doi:10.1007/s10584-007-9377-6.
- Duffy, P. B., R. W. Arritt, J. Coquard, W. Gutowski, J. Han, J. Iorio, J. Kim, I.-R. Leung, J. Roads, and E. Zeledon. 2006. "Simulations of present and future climates in the western United States with four nested regional climate models." *J. Climate.* 19:873-895.
- Durre, I., R. S. Vose, and D. B. Wuertz, 2006. "Overview of the Integrated Global Radiosonde Archive." *J. Climate*, **19**, 53-68.
- Fernau, M. E., and P. J. Samson, 1999. Use of cluster analysis to define periods of similar meteorology and precipitation chemistry in Eastern North America. Part I: Transport patterns. *J. Appl. Meteorol.*, **29**, 735-750.
- Ferreria, S. R., and E. M. Shipp. 2005. *Historical meteorological analysis in support of the 2003 San Joaquin Valley PM10 state implementation plan*. Final report, California Air Resources Board. Available at [www.arb.ca.gov/airways/CRPAQS/DA/met/HistoricalMet-2003PM10SIP.pdf](http://www.arb.ca.gov/airways/CRPAQS/DA/met/HistoricalMet-2003PM10SIP.pdf).
- Free, M., D. J. Seidel, J. K. Angell, J. Lanzante, I. Durre, and T. C. Peterson. 2005. Radiosonde Atmospheric Temperature Products for Assessing Climate (RATPAC): A new data set of large-area anomaly time series. *J. Geophys. Res.* 110: D22101, doi:10.1029/2005JD0006169.

- Gaffen, D. J. 1994. "Temporal inhomogeneities in radiosonde temperature records." *J. Geophys. Res.* 99:3667–3676.
- Gong, X., and M. B. Richman, 1995. On the application of cluster analysis to growing season precipitation in North America east of the Rockies. *J. Climate*, **8**, 897-931.
- Gordon, N., J. R. Norris, C. P. Weaver, and S. A. Klein, 2005. "Cluster analysis of cloud regimes and characteristic dynamics of midlatitude synoptic systems in observations and a model." *J. Geophys. Res.*, **110**, D15S17, doi:10.1029/2004JD005027.
- Haimberger, L. 2005. Homogenization of radiosonde temperature time series using ERA-40 analysis feedback information. *ERA-40 Project Report Series No. 23*. European Centre for Medium Range Weather Forecasts, Reading, UK.
- Hogrefe, C., B. Lynn, K. Civerolo, J. Y. Ku, J. Rosenthal, C. Rosenzweig, R. Goldberg, S. Gaffin, K. Knowlton, and P. L. Kinney. 2004. "Simulating changes in regional air pollution over the eastern United States due to changes in global and regional climate and emissions." *J. Geophys. Res.* 109: D22301, doi:10.1029/2004JD004690.
- Iacobellis, S. F., J. R. Norris, M. Kanamitsu, M. Tyree, and D. C. Cayan, 2009: Climate variability and California low-level temperature inversions. *California Climate Change Center*, publication #CEC-500-2009-020-F, 48 pages.
- IPCC, 2007. "Intergovernmental Panel on Climate Change Fourth Assessment Report: Climate Change 2007 (AR4)". Cambridge University Press, Cambridge, United Kingdom.
- Jakob, C. and G. Tselioudis, 2003. Objective identification of cloud regimes in the Tropical Western Pacific. *Geophys. Res. Lett.*, **30**, No. 21, 2082, doi:10.1029/2003GL018367.
- Kalnay, E, M. Kanamitsu, et al. 1996. "The NCEP/NCAR 40-year reanalysis project." *Bull. Amer. Meteor. Soc.* 77(3): 437–470.
- Kanamitsu, M., and H. Kanamaru. 2007. "57-Year California Reanalysis Downscaling at 10km (CaRD10) Part I. System Detail and Validation with Observations." *J. Climate.*, **20**, 5527-5552.
- Kanamaru, H., and M. Kanamitsu. 2007. "57-Year California Reanalysis Downscaling at 10km (CaRD10) Part II. Comparison with North American Regional Reanalysis.", *J. Climate.*, **20**, 5553-5571.

- Kleeman, M. J., S.-H. Chen, and R. A. Harley, 2010. "Climate change impact on air quality in California." *Report to the California Air Resources Board 04-349*, 220 pages. Available online at "<http://www.arb.ca.gov/research/apr/past/climate.htm>".
- Lebassi, B., J. Gonzalez, D. Fabris, E. Maurer, N. Miller, C. Milesi, P. Switzer, and R. Bornstein, 2009, Observed 1970-2005 cooling of summer daytime temperatures in coastal California, *J. Climate* Vo. 22, 3558-3573, doi:10.1175/2008JCLI2111.1
- Lu, R., and R. P. Turco. 1994. "Air pollutant transport in a coastal environment. Part I: Two-dimensional simulations of sea-breeze and mountain effects." *J. Atmos. Sci.* 51: 2285–2308.
- Mahmud, A., M. Tyree, D. Cayan, N. Motallebi, and M. J. Kleeman (2008), Statistical downscaling of climate change impacts on ozone concentrations in California, *J. Geophys. Res.*, 113, D21103, doi:10.1029/2007JD009534.
- Mesinger, F., et al. 2006. "North American regional reanalysis." *Bull. Amer. Meteor. Soc.* 87(3): 343–360.
- Mickley, L. J., D. J. Jacob, B. D. Field, and D. Rind. 2004. "Effects of future climate change on regional air pollution episodes in the United States." *Geophys. Res. Lett.* 31: L24103, doi 10.1029/2004GL021216.
- Morcrette, J.-J., 1990. "Impact of changes to the radiation transfer parameterizations plus cloud optical properties in the ECMWF model.", *Mon. Wea. Rev.*, **118**, 847-873.
- Neiburger, M. 1969. "The role of meteorology in the study and control of air pollution." *Bull. Amer. Meteor. Soc.* 50:957–965.
- Novakov, T., T. W. Kirchstetter, S. Menon, and J. Aguiar. 2008. "Response of California temperature to regional anthropogenic aerosol changes." *Geophys. Res. Lett.* 35: L19808, doi:10.1029/2008GL034894.
- Peterson, T. C., and R. S. Vose. 1997. "An overview of the Global Historical Climatology Network Temperature Database." *Bull. Amer. Meteor. Soc.* 78:2837–2849.
- Reynolds, R. W., N. A. Rayner, T. M. Smith, D. C. Stokes, and W. Wang. 2002. "An improved in situ and satellite SST analysis for climate." *J. Climate* 15:1609–1625.
- Schwartz, B. E., and M. Govett. 1992. A hydrostatically consistent North American radiosonde data base at the Forecast Systems Laboratory, 1946–present. NOAA Technical Memorandum ERL FSL-4. Available online at: <http://raob.fsl.noaa.gov/intl/radiosonde.pdf>.

- Snyder, M. A., J. L. Bell, L. C. Sloan, P. B. Duffy, and B. Govindasamy. 2002. "Climate responses to a doubling of atmospheric carbon dioxide for a climatically vulnerable region." *Geophys. Res. Lett.* 29(11): 1514, doi:10.1029/2001GL014431.
- Steiner, A. L., S. Tonse, R. C. Cohen, A. H. Goldstein, and R. A. Harley. 2006. "Influence of future climate and emissions on regional air quality in California." *J. Geophys. Res.* 111: D18303, doi:10.1029/2005JD006935.
- Tennekes, H. 1973. "A model for the dynamics of the inversion above a convective boundary layer." *J. Atmos. Sci.* 30:558–567.
- Thorne, P. W., D. E. Parker, S. F. B. Tett, P. D. Jones, M. McCarthy, H. Coleman, and P. Brohan. 2005. "Revisiting radiosonde upper air temperatures from 1958 to 2002." *J. Geophys. Res.* 110: D18105, doi:10.1029/2004JD005753.
- Wakimoto, R. M. 1987. "The Catalina Eddy and its effect on pollution over Southern California." *Mon. Wea. Rev.* 115:837–855.
- Watson, J. G., and J. C. Chow. 2002. "A wintertime PM<sub>2.5</sub> episode at the Fresno, CA, supersite." *Atmos. Environ.* 36:465–475.
- Wigley, T. M. L., B. D. Santer, and K. E. Taylor, 2000. Correlation approaches to detection. *Geophysical Research Letters*, **27**, 1112973-2976.
- Zhang, Y., J. M. Wallace, and D. S. Battisti. 1997. "ENSO-like interdecadal variability: 1900–93." *J. Climate* 10:1004–1020.